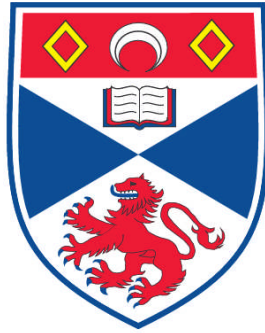


**METAL OXIDE POROUS SINGLE CRYSTALS AND OTHER  
NANOMATERIALS : AN HRTEM STUDY**

**Calum Dickinson**

**A Thesis Submitted for the Degree of PhD  
at the  
University of St. Andrews**



**2007**

**Full metadata for this item is available in  
Research@StAndrews:FullText  
at:**

**<http://research-repository.st-andrews.ac.uk/>**

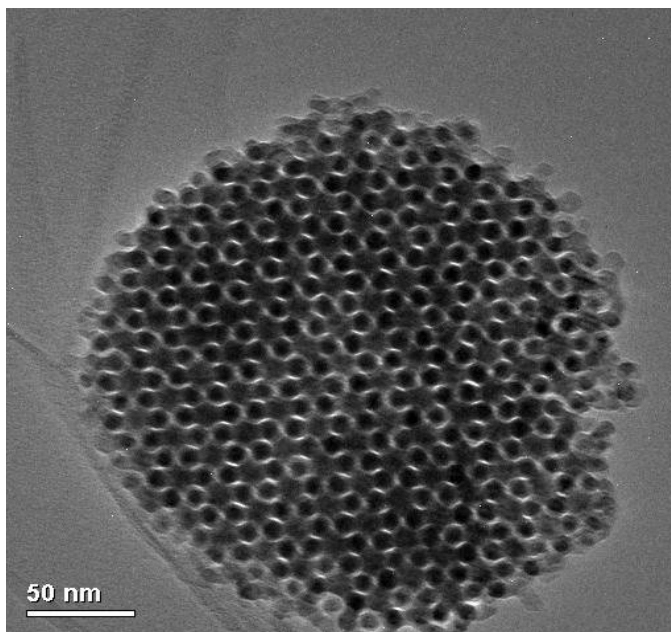
**Please use this identifier to cite or link to this item:**

**<http://hdl.handle.net/10023/217>**

**This item is protected by original copyright**

**This item is licensed under a  
Creative Commons License**

*Metal Oxide Porous Single Crystals and Other  
Nanomaterials: An HRTEM Study*



A thesis presented for the degree of

*Doctor of Philosophy*

In the Faculty of Science of the University of St. Andrews

By Calum Dickinson, BSc (Hons)



University  
of  
St Andrews



## *Acknowledgements*

Dr Wuzong Zhou has helped me so much over the past three years that words can not express enough my gratitude to him, but I will try. His training on the HRTEM, not only in the operation of the machine but the techniques for post analysis of the images has been invaluable. I also thank him for including me in on several collaborations with other universities and arranging for a 3 month placement at Fudan University, China. The patience and guidance through helpful discussions in not just the research, but on all aspects on personal conduct in the academic world, has made him a worthy addition to my christmas card list.

Many others, in their own little ways, have helped me get to the point where I am today. From the University of St. Andrews, I would like to thank Mr Ross Blackley, who has helped me on numerous occasions on the little nuances of the TEM and SEM. Mrs Sylvia Williamson for running the IGA and CHN analysis. Dr. Paul Wright and Professor David Cole-Hamilton for the use of their laboratories. Dr. Chris Baddeley and Dr Nigel Botting for being my additional referees for my CV and for allowing me to participate in bringing chemistry to the scientists of the future. Ms Gemma Catton and Mr Stewart Warrender for their friendship and conversations at lunch. Mr Graham Dawson and Mr Wenbo Yue for making the office habitable. And to everyone else who helped along the way; the technicians, the chemical society and the other PhD students who were all complete stars.

From outside of the university, I would like to thank: Prof. Andrew Harrison (University of Edinburgh), for his magnetic tests on my material and for his continuing help in the investigation of their properties. Prof. Jim Anderson (University of Aberdeen), for the ongoing catalytic tests of the material. Prof Loic Dupont (University of Picardie), for his agreement on electrochemical tests. Prof. Dongyuan Zhao (Fudan University), for welcoming me into his group for three months. Dr Robert Hodgkins (Stockholm University), for his help with isotherm data and all the

mesoporous discussion. Prof. Duncan Bruce (University of Exeter), Prof. Jian Sha (Zhejiang University), Prof. Diawen Pang (Wuhan University) and Prof. Heyong He (Fudan University) for their collaborations.

Additional thanks goes to EPSRC for funding the project and myself over the past 3 years.

Henry J. Tillman once said “*If you are not part of the solution then you are part of the precipitate*”. So I would like to thank everyone again for keeping me as part of the solution.

## *Dedication*

This thesis is dedicated to the memory of all those that have shaped my life who without them, I would not be the person I am today. The following are people who, unknowingly, have had an impact on my life but lost theirs in the past 3 years:

John Ritter (1948-2003)

Richard Biggs (1960-2004)

Marlon Brando (1924-2004)

Christopher Reeve (1952-2004)

Ossie Davis (1917-2005)

John 'Richard' Whiteley (1943-2005)

Robin Cook (1946-2005)

Pat Morita (1932-2005)

Richard Pryor (1940-2005)

Andreas Katsulas (1944-2006)

Paul Gleason (1944-2006)

Johnny Sekka (1934-2006)

And to my grandad Tommy Denholm, who died in March 2004.

*'The meeting of two personalities is like the contact of two chemical substances:*

*If there is any reaction, both are transformed.'*

Carl Jung

Thank you all for transforming my life, you will be sadly missed.

## *Abstract*

Three-dimensional porous single crystals (PSCs) are a recent development in the growing world of mesoporous material. The mesoporosity allows for the material to retain their nanoproperties whilst being bulk in size. The current work concentrates on chromium oxide and cobalt oxide PSCs formed in the templates SBA-15 and KIT-6.

HRTEM is the main technique used in this investigation, looking at the morphology and single crystallinity of these materials. A growth mechanism for the PSC material is proposed based on HRTEM observations. XRD studies revealed that the confinement effect, caused by the mesopores, reduces the temperature for both cobalt and chromium oxide crystallisation, as well as a different intermediate route from the metal nitrates. The properties of chromium oxide PSC are also investigated magnetically and catalytically. Some metal oxides in different templates are also presented, despite no PSC forming. HRTEM work on other nanomaterials, based on collaboration, is also presented.

## Contents

Cover .....	i
Declaration.....	ii
Acknowledgements.....	iii
Dedication.....	v
Abstract.....	vi
Contents.....	vii
1. Introduction.....	1
1.1 Early history of mesoporous silica .....	1
1.2 Developments in mesoporous silica .....	5
1.3 Functionalised mesoporous silica .....	8
1.4 Metal incorporated mesoporous silica .....	9
1.5 Non-siliceous mesoporous material.....	11
1.6 Mesoporous carbon.....	14
1.7 Three dimensional porous single crystals.....	16
1.8 Aim of the current project.....	19
References.....	21
2. Experimental.....	25
2.1 Synthesis of mesoporous silica.....	25
2.2 Synthetic methods of porous single crystals.....	27
2.3 High resolution transmission electron microscopy.....	29
2.4 Scanning electron microscopy.....	45
2.5 X-ray Diffraction.....	51
2.6 Nitrogen adsorption isothermic gravimetric analysis.....	55
2.7 Magnetism.....	57
2.8 Catalysis.....	60
References.....	62
3. Porous single crystals of chromium oxide.....	64
3.1 Synthetic methods for PSCs.....	64
3.2 Chromium oxide in SBA-15.....	68
3.3 Chromium oxide in KIT-6.....	79
References.....	89
4. Porous single crystals of cobalt oxide.....	90
4.1 Synthetic methods for PSCs.....	90
4.2 Cobalt oxide in SBA-15.....	91
4.3 Cobalt oxide in KIT-6.....	100
4.4 Nanobridges in KIT-6 templated PSCs .....	109
References.....	115
5. Various metal oxides using different silica templates.....	116
5.1 Synthetic methods of metal oxides.....	116
5.2 Porous metal oxides.....	117
5.3 Non-porous metal oxides.....	124

References.....	133
6. HRTEM of other nanomaterials.....	134
6.1 Ruthenium oxide nanoparticles in mesoporous silica.....	134
6.2 Silicon nanowires templated by AAO.....	137
6.3 Tri-functional nanospheres.....	145
References.....	150
7. Conclusions and future work.....	152
7.1 Conclusions.....	152
7.2 Future work.....	153
Publications.....	155

## 1. Introduction

Before the 1990s, the largest zeolite pore size was reported as 12-13Å.<sup>1</sup> This was the first material, named as VPI-5, that had a pore size greater than 10Å. Based on aluminophosphate, it was generally believed that zeolites would only increase in pore size slightly. Any increase in the size of the pore would also mean an increase in the ring members, VPI-5 was reported to have eighteen membered rings, and this tends to cause instability in the framework and the material would break down. At the turn of the 1990s, this changed when a new form of porous material was synthesised and not just once but by two independent methods, revolutionalising the world of zeolites, giving an exponential growth for this new class of material over the next 15 years.

### 1.1 Early history of mesoporous silica

In 1990, a new material was reported being synthesised at Waseda University in Japan.<sup>2</sup> The material, now commonly known as KSW-1, exhibited rather strange properties from the outset. Yanagisawa *et al* prepared the material by reacting one of the single layered polysilicates, kanemite, with alkyltrimethylammonium chloride for one week whilst stirring at 65°C under basic conditions; the process was repeated once more. Low angle X-ray diffraction (XRD) revealed peaks in the 2-3 2θ range and revealed d-spacings, for the material, ranging from 3-5 nm depending on the alkyl group used. It was also found that from nitrogen adsorption, the surface area of this mesoporous material had also increased significantly from 50 m<sup>2</sup>/g, of unreacted kanemite, to 900 m<sup>2</sup>/g. This indicated that the nitrogen was undergoing adsorption on the inside of the material. Nitrogen adsorption also allowed for a pore size distribution to be mapped and was found to be rather narrow in the range of 2-4 nm, once again dependent on the alkyl group used. TEM images revealed that the material had a hexagonally ordered pore structure, confirming results from XRD about the ordering and the isothermic data about the porosity. A

schematic diagram for the formation of this material, seen in Figure 1-1, was proposed a few years later.<sup>3</sup> The figure shows how the alkyltrimethylammonium ion replaces the sodium ion as the cation between the layer structure of the kanemite causing the sheets to fold and form a hexagonal material. The material also contains some of the parental material's crystalline structure. With the new large pore systems confirmed, it opened a new term for zeolitic chemists, mesoporous material. However, this was not the only mesoporous material discovered at this time.

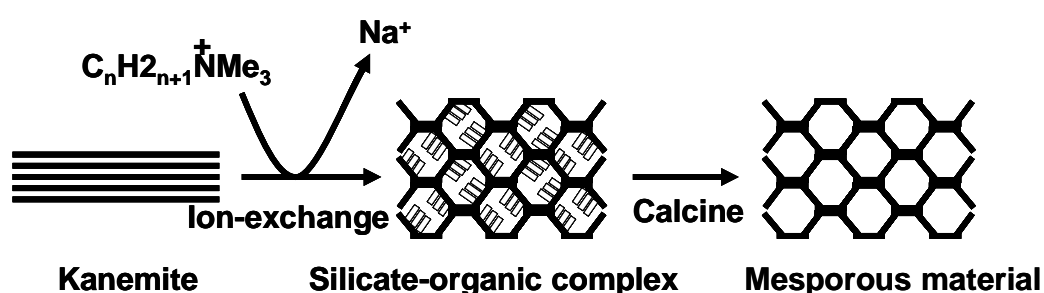


Figure 1-1. Schematic diagram of the formation of KSW-1<sup>3</sup>

A similar material, now known as MCM-41, although with a less time consuming method like the one above, was published in 1992 by Mobil Scientists (now ExxonMobil).<sup>4,5</sup> Although it was first synthesised a few years previously, placing the discovery of MCM-41 at around the same time as KSW-1, due to the commercial background, it was published later after patents were established.<sup>6-8</sup> The synthetic method involved creating micelles using an organic template before coating with a silica source of material and maturing for 48 h at 100 °C. The template could then be removed by calcinations, giving the mesoporous framework. The schematic diagram of this synthesis can be seen in Figure 1-2. Similar low angle XRD and nitrogen adsorption results were obtained for this material as it was from the Japanese material with pore sizes in the range of 1.6-5 nm. However, since the silica source was not from a layered compound but an amorphous material, the mesoporous material does not have any defects leftover from the

layered parent material. Transmission electron microscopy (TEM) was used to confirm this, and had not the TEM been used, then a whole different story could have been told.

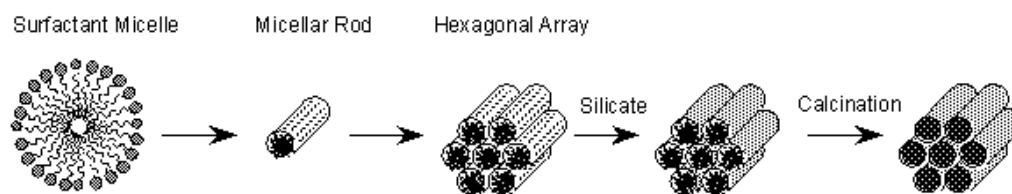


Figure 1-2. Schematic diagram of the formation of MCM-41<sup>5</sup>

Mobil Scientists, when the material was first synthesised, recognised that something about the material was different. Although when low angle XRD results were obtained, the experiments were rerun as well as the XRD data and the machine was also tested for faults. It was not until the TEM was used that they discovered the somewhat unique structure of this material. Since low angle XRD was not that commonly used, this material could have easily been missed if the TEM had not been used. In fact, in the later part of the 1960s, this material was indeed synthesised although was only recognised as ‘low density silica’.<sup>9</sup> It was not until a further study by French scientists in 1997,<sup>10</sup> who believed that since the procedure for the synthesis was relatively simple that someone must have tried a similar experiment in the past, after discovering a reference in Iler’s Chemistry of Silicon,<sup>11</sup> that the ‘low density silica’ was proved to have been mesoporous. Since the method of preparation of the mesoporous material by Mobil was relatively simple, and no new methods had been used to create this material, it was recognised that the characterisation of the material was fundamental to the discovery. XRD has always been very uncommon at low angles, as only very large d-spacings, too large for crystals, would result in such a low angle. However, the TEM was around at the time of the first synthesis and the magnification required to see the mesoporous material and their ordering is relatively low. Had the original scientists in 1969 checked the sample under the TEM, the discovery of the mesoporous material could have

been a lot sooner and a different mesoporous history would have been the result. As it was, two very similar mesoporous materials were made and characterised at around about the same time, although it was to be revealed how much they differed in the synthesis.

In 1995, a comparison between KSW-1 and MCM-41 was made from the synthesis and characterisation.<sup>12</sup> It set out to determine whether the mechanism for both materials' synthesis was the same. With the use of a wide range of techniques, it was shown that the kanemite did not undergo dissolution and therefore could not form around the micelles as proposed by the MCM-41 synthesis but more likely the layered compound stacks up before the layers fold towards each other (Figure 1-1). The fact that both methods were different has led to different lines of research in the mesoporous area.

Since the discovery of the mesoporous material, the number of papers on mesoporous material has increased almost exponentially, shown in figure 1-3, with 2300 publications being published in 2005 alone. These figures are taken from *Web of Science* using the key word 'mesoporous'.

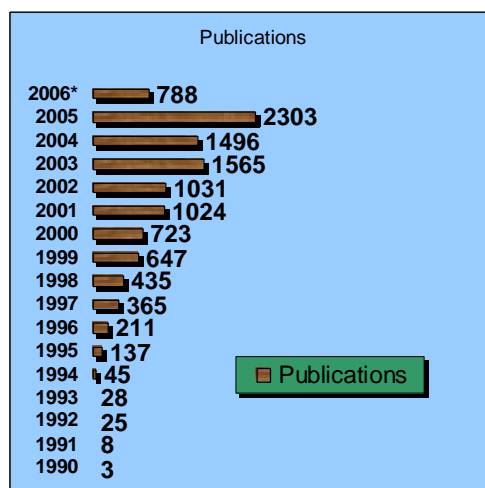


Figure 1-3. Publications on mesoporous material over the past 15 years. 2006\* publications as of 1<sup>st</sup> May.

Since the Mobil technique is by far more adaptable than the Waseda technique, which can be seen by the number of citations (4950 and 3922 for ref. 4 and 5 respectively compared to 501 for ref. 2), it is the Mobil technique that is treated as the standard way to create many different mesoporous materials.

There are two main ways to produce mesoporous material via the templating method. The first is soft templating which uses surfactant molecules, like the Mobil technique, methods and materials can be found in sections 1.2-1.5. The second is hard templating, or nanocasting, where a mesoporous material, normally mesoporous silica, is used as a template, which can be found in sections 1.6 and 1.7.

## 1.2 Developments in mesoporous silica

The mesoporous silica was immediately recognised as one of the most important discoveries in recent years by zeolite chemists and, as such, many started in this field worldwide working on both siliceous and non siliceous frameworks. In the mesoporous silica framework field, a discovery in 1995 about surfactants resulted in a major change in the development of new mesoporous silica.

MCM-41 is templated by a cationic quaternary ammonium surfactant that causes the anionic silica species to coat the micelles. Studies that followed afterwards always considered ionic surfactants until in 1995, in two independent studies, the ability to use non-ionic surfactants was discovered.<sup>13,14</sup> Attard *et al*,<sup>13</sup> unlike the MCM-41 synthesis, used the True Liquid-Crystalline Templating (TLCT) method to create the mesopores. Rather than being prepared in an acidified aqueous media, the surfactant was prepared in ethanol with the phase of the micelles arrangement being confirmed by light microscopy before adding the silica source. The non-ionic surfactants came from using various chain lengths of polyethylene oxides in the form of Pluronic and

Tergitol surfactants. This allowed the possibility of reusing the surfactant if it was extracted, rather than decomposed by calcination, and also led to one of the most important mesoporous silicas.

In 1998, non-ionic triblock copolymers were used to create a series of mesopore silica systems that were not only larger in pore size but in wall thickness.<sup>15,16</sup> The triblock copolymers are made up from Poly (ethylene oxide)-poly (propylene oxide)-poly(ethylene oxide) chains, (normally abbreviated to PEO-PPO-PEO), varying in length. SBA-15, which is now one of the widest used mesoporous silicas, was created using this surfactant type and is made up of large mesopores in a hexagonal array and, unlike MCM-41, smaller connecting pores between these which results in a connected pore system. The connecting pores were first indicated by adsorption data, although they could not be physically seen until later (Section 1-6).

For the siliceous mesoporous material using pluronic P123 ( $\text{EO}_{20}\text{PO}_{70}\text{EO}_{20}$ ), like SBA-15, the surfactant was dissolved in an acidified aqueous media and when the solution was clear, the silica source was added, normally TEOS or TMOS. The solution was then stirred for 24 h before being matured statically at typically 100 °C for 24-72 h. The material was then calcined at 550 °C for 5 h to remove the surfactant. When using the surfactant Pluronic F127 ( $\text{EO}_{106}\text{PO}_{70}\text{EO}_{106}$ ), the addition of KCl was required to aid the dissolving of the surfactant.

The pore size for SBA-15 could be tailored from 50-300 Å, which is much larger than the range for MCM-41, 30-100 Å, where both materials' high range comes from the use of a swelling agent, 1,3,5 trimethylbenzene (TMB). The wall thickness of SBA-15 has an inverse relationship with the pore size, as the unit cell d-spacing is relatively constant. Both parameters can be tailored by altering the maturation temperature and time. A lower temperature creates a smaller pore but larger wall thickness, with the pore being about twice the diameter and the wall thickness is six times larger than that of MCM-41. The higher temperature leads to pores that are 4-5 times larger and walls three times thicker than MCM-41. The importance of the connectivity

between the pores becomes apparent when using the mesoporous material as a template for nanocasting; this is discussed later (section 1.6).

Since the introduction of the triblock copolymers, many silica phases from the non-ionic pathway have been created. The ability to add in swelling agents, mentioned earlier, to the mixture at the micelle forming stage can alter the phase and pore size of the mesoporous silica. KIT-6, analogous to MCM-48, and FDU-12, a cage structure like SBA-16, use similar conditions to SBA-15 and SBA-16, with the exception of the addition of butan-1-ol and TMB, respectively, as swelling agents.<sup>17,18</sup> Figure 1-4 shows the mathematical representations, that have the lowest overall free energy for the shape, of some mesoporous templates, (a) is representative of hexagonal SBA-15 where you can also see the connecting micropores,<sup>19</sup> (b) is a bicontinuous framework like KIT-6 or MCM-48,<sup>19</sup> (c) and (d) are cage structures with (c) like SBA-16<sup>20</sup> (body-centered) and (d) like FDU-12 (face-centered).<sup>21</sup> The intensity of colour in the areas is the extent of the curvature on the gibbs free energy in that area.

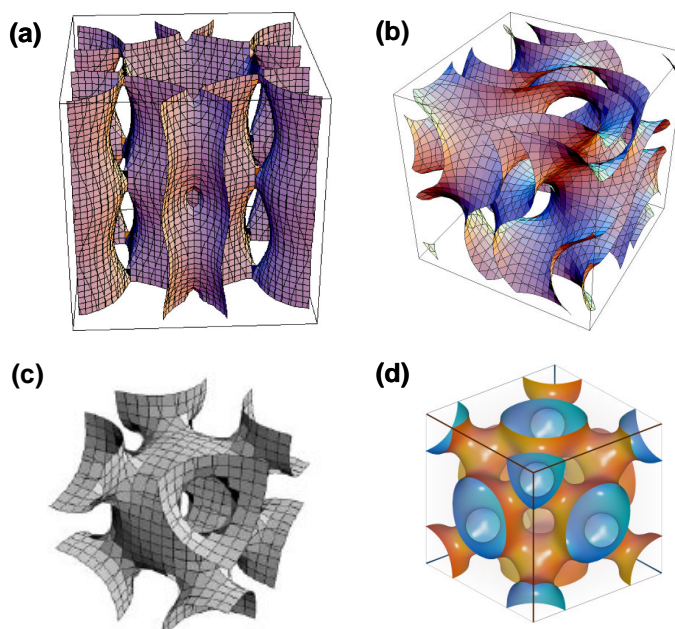


Figure 1-4. Mathematical diagrams of mesoporous structures for (a) SBA-15, (b) KIT-6, (c) SBA-16 and (d) FDU-12.<sup>19,20,21</sup>

### 1.3 Functionalised mesoporous silica

The fact that mesoporous silica is well ordered with uniform mesopores, which can be tailored to various sizes, allowed research into possible applications. This led to scientists working at the functionalisation of the walls of the silica. The functionalisation can either occur at the synthesis step (*in situ*) or the post synthesis step.

*In situ* functionalisation is typically carried out using a silica source with an organic group attached, such as phenyltriethoxysilane and *n*-octyltriethoxysilane.<sup>22</sup> The introduction of the organics into the mesopores, in this manner, can give a higher thermal stability for the organics when compared to other modified silicas. Work by MacQuarrie, revealed that not only the thermal stability for the aminopropyl-MCM was increased, from 250 °C to >500 °C, but also a high solvent stability, with no removal of the aminopropyl groups even after immersion in ethanol under reflux.<sup>23</sup> Problems, however, can arise when the desired organic group changes the phase of the material. Studies of the effect on the addition of different percentages of a thiol group, in this case 3-mercaptopropyltriethoxysilane, into synthesis of SBA-15 revealed how it could change the structure, pore size and surface area.<sup>24</sup> An earlier study had revealed how SBA-15 (hexagonal) could be changed to FDU-5 (cubic), by the addition of a certain percentage of the same thiol.<sup>25</sup> However, this change in pore structure was not always a desired effect which is only found using *in situ* functionalisation and not post-synthesis functionalisation

When the functionalisation occurs post synthesis, the functional groups are grafted to the cell walls. Typically, the same chemicals used in the *in situ* method, an organic group attached to a triethoxysilane molecule, are introduced into the template material.<sup>26</sup> The triethoxysilane part of the molecule reacts with the silanol groups on the wall anchoring the organic group inside the pore; this can be seen in Figure 1-5. This easily adaptable technique allows a whole host of organic groups to be grafted. The more reactive groups at the end of the chains can be altered

further to allow other functional groups to be present, such as CN being converted to COOH. The major advantage of attaching the functional groups, in this method, is that it does not alter the mesopore structure, unlike the *in situ* method. However, there is a reduction in pore size, due to the protruding organic groups, and additional steps are required than that of the *in situ* method.

The uniform size of these pores can result in specific reactions where the size of the pore can be tailored for the reaction. Smaller pore sizes will allow inaccessibility for large chain molecules to enter and will always be more selective than grafted material with no pores. The ability to functionalise the material allows for catalytic experiments to take place, such as esterification.<sup>27</sup> Although with the addition of metals, the catalytic experiments available increase dramatically.

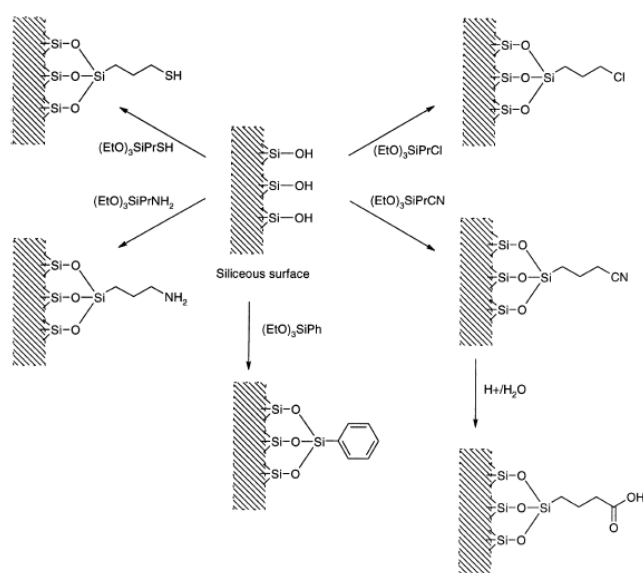


Figure 1-5. Preparation of post synthesis functionalisation of mesoporous silica.<sup>26</sup>

#### 1.4 Metal incorporated mesoporous silica

As mentioned above, mesoporous silica can be functionalised to allow for the synthesis of a specific catalyst. Metal incorporation can also be done allowing for catalysts to be made. Even from the very beginning, it was noted that metals could be added into the framework, with Beck *et al* reporting the incorporation of aluminium.<sup>5</sup> Very soon after the discovery of mesoporous

silica, various other metals were reported as having been added into the walls of the silica, titanium being just one of these.<sup>28</sup> There are two ways for the metal to be incorporated, much like the organic functionalisation, embedding and grafting.

The metal can be embedded into the framework in the growth stage of the mesoporous material. This is normally achieved by adding a metal organic salt with the silica source into a solution containing the surfactant.<sup>28,29</sup> Another method for preparing the embedded metal is the use of a metal containing surfactant.<sup>30</sup> This is used in the same way as the standard surfactant, with the exception of the calcination of the surfactant leaving the metal behind in the framework. The metal containing surfactants, however, are not commercially available and normally need to be synthesised first.<sup>31</sup> However, grafting uses more commercially available metal containing chemicals.

Grafting is done simply by adding the metal, in the form of a salt, to the pores of the already synthesised mesoporous silica. The silanol groups situated on the pore walls allow for the metal complex to be anchored.<sup>32</sup> As was the disadvantage of the post synthesis functionalisation, the metal will reduce the pore size by protruding from the pore walls. The addition of organic groups on the metal surface can help avoid aggregation of the metal particles.

The difference between the embedded and the grafted titanium can be seen in figure 1-6. The computer simulation of the silica wall shows how the titanium sits on top of the oxygen groups on the silica wall when grafted (a) and is under the oxygen in the silica for the embedded (b). The computer simulation also shows the presence of oxygen groups around the titanium.

The catalytic activity of both methods of metal incorporation in mesoporous silica has been compared and one such study shows the effects not only on the rate of reaction but the selectivity on the product.<sup>33</sup> In the paper, it was found that the embedded titanium slowly converted almost all the reactant to the desired product with (73-95 %) selectivity, whereas the grafted titanium

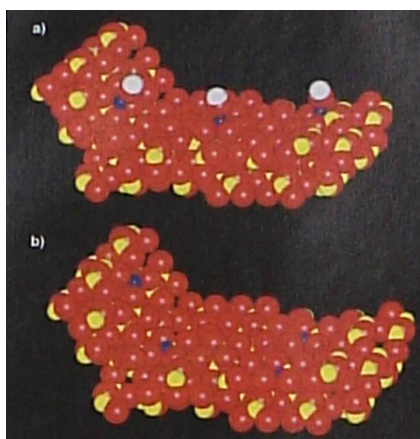


Figure 1-6. Computer simulation of (a) grafted titanium and (b) embedded titanium on the pore wall of MCM-41.<sup>33</sup>  
Blue= Ti, yellow= Si, red= O and white= H.

converted most of the reactant to the desired product (95-99 %) at a rate that was an order of magnitude higher than the embedded. Both the embedded and the grafted Ti exhibited a much higher selectivity to the desired product, in this case the epoxide, than that of UV light (2.5 %), and both are efficient catalysts depending on whether you want a high conversion or a high rate. Whilst the mesoporous silica was being investigated as a good catalytic support for non siliceous species, the research into non siliceous mesoporous materials was still at work.

### 1.5 Non-siliceous mesoporous material

In 1997, the first ordered mesoporous metal was synthesised.<sup>34</sup> As with the above examples, the material was synthesised with the use of surfactants as the templating group. The work of Attard<sup>13</sup> and Pinnavaia<sup>14</sup>, the use of non-ionic surfactants allowed for the removal by a solvent method rather than the calcination, which allows the mesoporous system to remain intact.

With the mesoporous metals, the way of the TLCT was the starting route, by first making the liquid crystalline phase, confirmed by optical microscopy, before adding a metal salt. The metal forms around the micelles of the surfactant and creates the mesoporous structure, before being

reduced by the addition of a reducing agent. The salt, surfactant and reducing agent can then be removed by washing with various solutions. TEM of the material not only confirms the mesoporous nature of the material, as does the low angle XRD, but it also reveals the spherical nature of the mesoporous material. This interesting phenomenon, which tends to not be seen in mesoporous silica, will be discussed later in the thesis.

The above method, results in the creation of mesoporous metal powders. However it was not long before Attard *et al* created another first, this time in the form of mesoporous thin films.<sup>35</sup> As the powder used the true liquid crystal template (TLCT) method, so does the thin film with the addition of the surfactant being put onto a conducting material. The thin film is then created by the electrodeposition of the metal and this replicates the mesoporous structure as before. The ability to make mesoporous material in the form of thin films has the possibility of being of use in gas sensors and battery applications. Metal oxides were also of great interest for several of these applications.

In 1994, various mesoporous metal oxides using the surfactant technique were synthesised.<sup>36,37</sup> However, the early synthesis of mesoporous metal oxides had several problems related to the material. Not only did quite a lot of the material stay within the lamellar phase, there was also a problem of surfactant removal. Both forms of surfactant removal, calcination and solvent extraction, caused the collapse of the porous material. The metal oxides were thermally unstable as they could not withstand heating to the temperatures required to remove the surfactant. It was not until a year later that this became possible.

In 1995, the first thermally stable mesoporous metal oxide material was created.<sup>38</sup> Titanium oxide was able to retain the mesopores, even after calcination at 500 °C, which could be seen by the TEM. The surface area was only 200 m<sup>2</sup>/g, which although larger than bulk material is significantly lower than MCM-41<sup>5</sup> even after the difference between the density of titanium oxide and amorphous silica have been taken into account.

Following this discovery, in 1996, the formation of porous zirconium oxophosphate was discovered.<sup>39</sup> Not only was the pore surface area larger than the titanium oxide, the stability of the material could be altered by the addition of additional phosphate groups. It was also believed that the instability of the other mesoporous metal oxides is contributed to by the fact that transition metal species tend to have more than one stable oxidation state, for which zirconium has only one. Both the titanium and the zirconium used ionic surfactants as the templating material, which led to research using non ionic surfactants a couple of years later.

After the discovery of the non ionic triblock copolymers in 1998,<sup>15</sup> the previously thermally unstable materials were reviewed. The result was very positive; with metal oxide frameworks that previously were unable to have their surfactants removed retaining their porosity after calcination.<sup>40</sup> Using the surfactant P123, a wide range of thermally stable mesoporous oxides were synthesised. The pore diameters ranged from typically 35-60 Å for the transition metal block, which were relatively large pores although smaller than the aluminium oxide and silica pores, both of which were ~130 Å. The surface area of these materials, despite using a larger precursor, was comparable to the zirconium oxophosphate, with the titanium oxide having almost identical surface areas. The surface area ranges for the metal oxides tend to be ~900 m<sup>2</sup> cm<sup>-3</sup>, with the exception of a few, tantalum oxide being the highest at ~1353 m<sup>2</sup> cm<sup>-3</sup>.<sup>40</sup> Mesoporous silica was however still the highest at 1782 m<sup>2</sup> cm<sup>-3</sup>, although the wall of the metal oxide revealed something different than that of silica.<sup>15</sup>

Another interesting feature was the presence of nanocrystals within the wall. These crystals typically ranged from less than 1 nm to about 3 nm. There was no correlation between the surface area of the porous material to the presence and size of the nanocrystals in the wall. The use of the TEM with this material allows the presence of the nanocrystals to be determined, especially whether they are in a high or low yield. The use of dark field imaging gives the ability to distinguish between crystalline areas and amorphous areas of the material. With one sort of non

siliceous material being synthesised from the surfactant template *via* the soft templating route, another type of material can be made using the silica *via* the hard templating route.

## 1.6 Mesoporous carbon

Whereas the above mesoporous material's synthesis involves the use of surfactants, it is worth remembering that the mesoporous silica can be used as a template itself. In 1999, Ryoo *et al* created the first mesoporous carbon framework, CMK-1, using a very simple technique known as nanocasting or hard-templating.<sup>41</sup>

Using MCM-48, a mesoporous silica with a cubic arrangement, as the template, sucrose and sulphuric acid was impregnated into the framework. The material was then heated at 800-1100 °C under vacuum and the sulphuric acid catalyses the carbonisation creating the carbon framework. The silica template then can be removed by hydrofluoric acid, leaving the free standing carbon framework, revealing some interesting structure features.

The carbon framework was found to not be the negative replica of the template and as such had a different space group,  $I4_1/a$ , than that of its parent material,  $Ia3d$ . It was however found that when using SBA-15 as a template, creating CMK-3, that the material not only replicated the space group but the contours of the surface of the pore wall.<sup>42,43</sup> Although evidence for the presence of micropores could be seen in the original paper with results from the isotherm,<sup>16</sup> it was not until the framework was used as a template for carbon that it could physically be seen. Figure 1-7 shows the difference between using MCM-41, which has no complementary pores, and SBA-15 which isothermic evidence had indicated the presence of complementary pores. As can be seen, carbon templated by MCM-41 can only give disordered nanorods whereas carbon, templated by SBA-15, can result in a hexagonal framework.

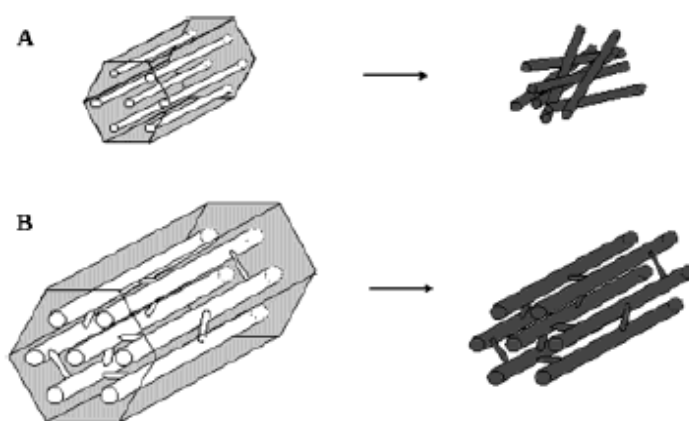


Figure 1-7. Schematic drawing of pore systems (left) and the carbon replicas (right) of A, MCM-41 and B, SBA-15.<sup>43</sup>

In fact, the importance of being able to see the 3D mesoporous structure with the negative replica is rather apparent. Figure 1-8 shows replicas of the mesoporous silica which can be seen in Figure 1-4. (a) is a negative replica of SBA-15, such as CMK-3. It is worth noting that you can see the connecting bridges, which were the complementary pores within SBA-15. (b) is the negative replica of an *Ia3d* mesostructure, MCM-48 or KIT-6, note the bicontinuous system, one depicted in white and the other black. (c) is the negative replica of the body centered cage structure of SBA-16 and (d) is the negative replica of the cage structure of FDU-12. The mesoporous carbon walls, like the silica, made in this way tend to have amorphous walls, however recently this has changed with the creation of graphite walls.<sup>44</sup>

The graphite walls are made up of discoid graphene sheets that align perpendicularly to the walls of the template.<sup>44</sup> The use of aluminium inside the walls of the templating material offers catalysis. The graphite walls were a result of the changing of the carbon precursor from sucrose to an aromatic compound. This method was found to work for various silica templates that carbon replicas had already been reported including cubic MCM-48<sup>5</sup> and SBA-1<sup>47</sup>, CMK-1 and CMK-2 respectively, as well as hexagonal SBA-15<sup>15</sup>, CMK-3<sup>42</sup>. It is the crystalline graphite walls, which show the importance of hard templating, as this would not have been created using

soft templating. With soft templating, the majority of the walls tend to be mainly amorphous, however the hard templating can lead to material with crystalline walls.

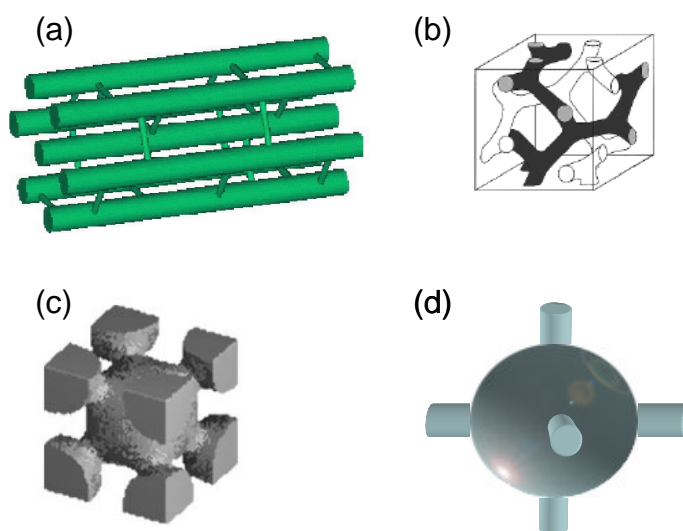


Figure 1-8. Negative replicas of (a) SBA-15, (b) KIT-6, (c) SBA-16 and (d) FDU-12.<sup>20,45,46</sup>

### 1.7 Three dimensional porous single crystals

In 2003, Zhu *et al* reported the synthesis of the first three dimensional porous single crystal.<sup>48</sup> This was made using the hard templating method, using SBA-15 as a template. TEM work was used to investigate the single crystal property of the material and found that each nanorod array gave a single crystal pattern. Atomic imaging further corroborated this as the same atomic orientation was seen in each rod although separate to different particles. The communication, between the nanorods, comes via the nanobridges, which were the randomly orientated complementary pores in SBA-15 (see Figure 1-7 and 1-8). This, however, was not the only material of this type.

At around the same time and independently, another PSC was discovered in the form of indium oxide.<sup>49</sup> As mentioned this also revealed a single crystal property in both the hexagonal,

*P6mm*, form and the cubic, *Ia3d*, form. The difference in synthesis is easily apparent between the two materials; the former uses several steps whereas the latter uses one step.

With the synthesis of the chromium oxide PSC, SBA-15 was calcined before grafting aminopropyltriethoxysilane (APTS) onto the silica walls via refluxing in toluene for 5 h. The chromium oxide precursor, potassium dichromate, was then dissolved in water and was stirred with the template, for 12 h, before filtering and drying. The chromium oxide precursor, within the template, was then decomposed in a furnace at 550 °C for 5 h before removing the silica template with a 10 % HF solution.

The synthesis of the indium oxide PSC was as follows: The indium nitrate and the surfactant, P123, were dissolved in ethanol for 0.5 h before adding the silica source, TEOS, with HCl. The mixture was then dried at room temperature for 18 h before adding a thin layer of paraffin before heating again for 18 h at 60 °C. The sample was then calcined at 550 °C for 5 h before removing the silica template with a 2 M NaOH solution.

The *Ia3d* platinum network, published much earlier in 2001, was reported as the first time the *Ia3d* micellar framework had been seen under the TEM.<sup>46</sup> Although the TEM images show a nice crystalline edge, there is no mention as to whether the particles had a polycrystalline or a single crystal SAED pattern. The only mention in the paper about the crystallinity refers to the thin edges giving the standard crystalline patterns.

Often, the crystalline nature of the material has not been investigated. As such, it is difficult to establish whether the material is single crystal or polycrystalline. An example of this is cerium oxide reported by Laha and Ryoo.<sup>50</sup> This paper was published around the beginning of this project. Similarly, when Ryoo and co-workers reported the production of CMK-8 and CMK-9, they also mentioned another mesoporous platinum.<sup>17</sup> Still with the *Ia3d* structure but this time using KIT-6, as opposed to MCM-48, as the template. However, once again the crystallinity of the mesoporous material was not investigated.

Since the start of this project, concurrent work done in Zhao's group has occurred.<sup>51,52</sup> Using MCM-48 and SBA-15 as templates, the material, in the form of the metal nitrate, was impregnated via ethanol evaporation, into the microwave digested template. After the evaporation, the material was then heated to 550 °C for 5 h before removing the silica template with a 2 M NaOH or a 10 % HF solution.

This method was later adopted for this project as there was less wastage and it was far simpler than the previous methods with fewer steps and greater adaptability to different metal oxides. However, due to availability of the apparatus, the silica templates were calcined rather than microwave digested. The Zhao group reported that microwave digested material had a higher number of silanol groups with almost full removal of the template.<sup>53</sup> Typically, when considering calcination against ethanol extraction, a decision needs to be made with high surfactant removal (the former) or high number of silanol groups within the pores (the latter). Although, silanol groups play a part in the impregnation step, it is not the major factor. The crystallinity from Zhao's papers differed with each material. The metal oxide single crystal material, although not investigated in detail, were chromium, cobalt, indium and nickel whereas polycrystalline metal oxide materials were iron, manganese and cerium. The polycrystalline material does not necessarily mean that a single crystal is not possible, as in the case of iron oxide.<sup>54</sup>

In a recent paper of work by another group at the University of St Andrews on PSCs, single crystal iron oxide was reported.<sup>54</sup> They reported not only the properties of this single crystal material but compared it to the mesoporous polycrystalline material. Both materials were prepared in the same template of KIT-6. The use of carbon aerogels as templates for magnesium oxide has also been reported, although no large scale mesoporous ordering was seen nor was the magnesium oxide single crystal material but made up of small crystallites.<sup>55</sup> Work carried out by the same group created mesoporous cobalt oxide, diffraction patterns were not shown in the TEM work and so once again it is hard to determine whether the material is single crystal or

polycrystalline. It would be worth noting that work carried out for this project has shown single crystallinity for the mesoporous structure in a similar system.

It is no doubt over the past few years of this project there have been significant advances in the field. New mesoporous material has been discovered and the special nature of the single crystallinity has been compared to polycrystalline material. However, more often than not, the single crystallinity of these materials has not been completely investigated.

## 1.8 Aim of the current project

The aim of this project was to produce PSCs in a variety of templates, to study the formation mechanism of these materials and to study the detailed structure of these materials.

The PSC should be of a wide interest in applications. Like most mesoporous material, they are large in size, which makes them easy to handle, but due to the nanoscale channels, they have nanoproperties. With the case for the PSC, since it is a single crystal, it should be more thermally stable than amorphous and polycrystalline material. The mesoporous framework makes them self supported catalysts, and since there is no need for an additional support, the properties will not be reduced. Additionally, even if the particles aggregate together, which normally causes nanoparticles to become bulk material, the frameworks should stay intact retaining their nanoproperties.

By looking at the formation mechanism, it can reveal interesting effects from the mesoporous silica template. The mesoporous template will act like a nanoreactor and as such will cause different effects in the growing of the crystal. Also, mesoporous material with similar pore diameter but different shape could cause different nanoreactor results.

This project investigates the synthesised PSCs of chromium oxide and cobalt oxide in KIT-6 and SBA-15. The single crystallinity of these materials is confirmed with the use of HRTEM and

SAED studies. The decomposition temperature of the precursor material, inside the mesopores, to metal oxides and the metastable intermediates are compared to that of the bulk. The magnetic and catalytic properties for the chromium oxide PSC are presented. Chromium and cobalt oxides are compared and a formation mechanism is proposed. Work carried out on other metal oxides and mesoporous templates are also reported, as well as the HRTEM on other nanomaterials.

## References

- [1] M.E. Davis, C. Saldarriaga, C. Montes, J. Garces and C. Crowder, *Zeolites*, 1988, **8**, 362.
- [2] T. Yanagisawa, T. Shimizu, K. Kuroda, and C. Kato, *Bull. Chem. Soc. Jpn.*, 1990, **63**, 988
- [3] S. Inagaki, Y. Fukushima and K. Kuroda, *Chem. Commun.*, 1993, 680
- [4] C.T. Kresge, M.E. Leonowicz, W.J. Roth, J.C. Vartuli and J.S. Beck, *Nature*, 1992, **359**, 710
- [5] J.S. Beck, J.C. Vartuli, W.J. Roth, M.E. Leonowicz, C.T. Kresge, K.D. Schmitt, C.T.-W. Chu, D.H. Olson, E.W. Sheppard, S.B. McCullen, J.B. Higgins and J.L. Schlenker, *J. Am. Chem. Soc.*, 1992, **114**, 10834
- [6] J.S. Beck, *US Patent No. 5057296*, 1991
- [7] C.T. Kresge, M.E. Leonowicz, W.J. Roth and J.C. Vartulli, *US Patent No. 5098684*, 1992
- [8] C.T. Kresge, M.E. Leonowicz, W.J. Roth and J.C. Vartulli, *US Patent No. 5102643*, 1992
- [9] V. Chiola, J.E. Ritsko and C.D. Vanderpool, *US Patent No. 3556725*, 1971
- [10] F. Drenzo, H. Cambon and R. Dutarte, *Micropor. Mater.*, 1997, **10**, 283
- [11] R.K. Iler, *The Chemistry of Silica*, 1979
- [12] C.Y. Chen, S.Q. Xiao and M.E. Davis, *Micropor. Mater.*, 1995, **4**, 1
- [13] G.S. Attard, J.C. Glyde and C.G. Goltner, *Nature*, 1995, **378**, 366
- [14] S.A. Bagshaw, E. Prouzet, T.J. Pinnavaia, *Science*, 1995, **269**, 1242
- [15] D.Y. Zhao, J.L. Feng, Q.S. Huo, N. Melosh, G.H. Fredrickson, B.F. Chmelka and G.D. Stucky, *Science*, 1998, **279**, 548
- [16] D.Y. Zhao, Q.S. Huo, J.L. Feng, B.F. Chmelka and G.D. Stucky, *J. Am. Chem. Soc.*, 1998, **120**, 6024
- [17] F. Kleitz, S.H. Choi and R. Ryoo, *Chem. Commun.*, 2003, 2136
- [18] J. Fan, C.Z. Yu, F. Gao, J. Lei, B.Z. Tian, L.M. Wang, Q. Luo, B. Tu, W.Z. Zhou and D.Y. Zhao, *Angew. Chem. Int. Ed.*, 2003, **42**, 3146

- [19] O. Terasaki, T. Ohsuna, Z. Liu, Y. Sakamoto and A.E. Garcia-Bennett, *Stud. Surf. Sci. Catal.*, 2004, **148**, 261
- [20] Y. Sakamoto, M. Kaneda, O. Terasaki, D.Y. Zhao, J.M. Kim, G.D. Stucky, H.J. Shin and R. Ryoo, *Nature*, 2000, **408**, 449
- [21] <http://www.msri.org>
- [22] S.L. Burkett, S.D. Sims and S. Mann, *Chem. Commun.*, 1996, 1367
- [23] D.J. MacQuarrie, *Chem. Commun.*, 1996, 1961
- [24] R.P. Hodgkins, A.E. Garcia-Bennett, P.A. Wright, *Micropor. Mesopor. Mater.*, 2005, **79**, 241
- [25] X.Y. Liu, B.Z. Tian, C.Z. Yu, F. Gao, S.H. Xie, B. Tu, R.C. Che, L.M. Peng and D.Y. Zhao, *Angew. Chem. Int. Ed.*, 2002, **41**, 3876
- [26] H.H.P. Yiu, P.A. Wright and N.P. Botting, *J. Mol. Catal. B Enzym.*, 2001, **15**, 81
- [27] W.D. Bossaert, D.E. De Vos, W.M. Van Rhijn, J. Bullen, P.J. Grobet and P.A. Jacobs, *J. Catal.*, 1999, **182**, 156
- [28] P.T. Tanev, M. Chibwe and T.J. Pinnavaia, *Nature*, 1994, **368**, 321
- [29] A. Corma, M.T. Navarro and J. P. Pariente, *Chem. Commun.*, 1994, 147
- [30] N.C. King, C. Dickinson, W.Z. Zhou and D.W. Bruce, *Dalton Trans.*, 2005, 1027
- [31] J. Bowers, M.J. Danks, D.W. Bruce and R.K. Heenan, *Langmuir*, 2003, **19**, 292
- [32] T. Maschmeyer, F. Rey, G. Sankar and J.M. Thomas, *Nature*, 1995, **378**, 159
- [33] R.D. Oldroyd, J.M. Thomas, T. Maschmeyer, P.A. Macfaul, D.W. Snelgrove, K.U. Ingold and D.D.M. Wayner, *Angew. Chem. Int. Ed.*, 1996, **35**, 2787
- [34] G.S. Attard, C.G. Goltner, J.M. Corker, S. Henke and R.H. Templer, *Angew. Chem. Int. Ed.*, 1997, **36**, 1315
- [35] G.S. Attard, P.N. Bartlett, N.R.B. Coleman, J.M. Elliott, J.R. Owen and J.H. Wang, *Science*, 1997, **278**, 838

- [36] U. Ciesla, D.G. Demuth, R. Leon, P.M. Petroff, G.D. Stucky, K.K. Unger and F. Schuth, *Chem. Commun.*, 1994, 1387
- [37] Q.S. Huo, D.I. Margolese, U. Ciesla, D.G. Demuth, P.Y. Feng, T.E. Gier, P. Sieger, A. Firouzi, B.F. Chmelka, F. Schuth and G.D. Stucky, *Chem. Mater.*, 1994, **6**, 1176
- [38] D.M. Antonelli and J.Y. Ying, *Angew. Chem. Int. Ed.*, 1995, **34**, 2014
- [39] U. Ciesla, S. Schacht, G.D. Stucky, KK Unger and F. Schuth, *Angew. Chem. Int. Ed.*, 1996, **35**, 541
- [40] P.D. Tang, D.Y. Zhao, D.I. Margolese, B.F. Chmelka and G.D. Stucky, *Nature*, 1998, **396**, 152
- [41] R. Ryoo, S.H. Joo and S. Jun, *J. Phys. Chem. B*, 1999, **103**, 7743
- [42] S. Jun, S.H. Joo, R. Ryoo, M. Kruk, M. Jaroniec, Z. Liu, T. Ohsuna and O. Terasaki, *J. Am. Chem. Soc.*, 2000, **122**, 10712
- [43] R. Ryoo, S.H. Joo, M. Kruk and M. Jaroniec, *Adv. Mater.*, 2001, **13**, 677
- [44] T.W. Kim, I.S. Park and R. Ryoo, *Angew. Chem. Int. Ed.*, 2003, **42**, 4375
- [45] W.Z. Zhou, K.K. Zhu, B. Yue, H.Y. He and C. Dickinson, *Stud. Surf. Sci. Catal.*, 2004, **154**, 924
- [46] H.J. Shin, R. Ryoo, Z. Liu and O. Terasaki, *J. Am. Chem. Soc.*, 2001, **123**, 1246
- [47] Q.S. Huo, D.I. Margolese, U. Ciesla, P. Feng, T.E. Gier, P. Sieger, R. Leon, P.M. Petroff, F. Schuth and G.D. Stucky, *Nature*, 1994, **368**, 317
- [48] K.K. Zhu, B. Yue, W.Z. Zhou and H.Y. He, *Chem. Commun.*, 2003, 98
- [49] H.F. Yang, Q.H. Sui, B.Z. Tian, Q.Y. Liu, F. Gao, S.H. Xie, J. Fan, C.Z. Yu, B. Tu and D.Y. Zhao, *J. Am. Chem. Soc.*, 2003, **125**, 4724
- [50] S.C. Laha and R. Ryoo, *Chem. Commun.*, 2003, 2138
- [51] B.Z. Tian, X.Y. Liu, H.F. Yang, S.H. Xie, C.Z. Yu, B. Tu and D.Y. Zhao, *Adv. Mater.*, 2003, **15**, 1370

- [52] B.Z. Tian, X.Y. Liu, L.A. Solovyov, Z. Liu, H.F. Yang, Z.D. Zhang, S.H. Xie, F.Q. Zhang, B. Tu, C.Z. Yu, O. Terasaki and D.Y. Zhao, *J. Am. Chem. Soc.*, 2004, **126**, 865
- [53] B.Z. Tian, X.Y. Liu, C.Z. Yu, F. Gao, Q. Luo, S.H. Xie and D.Y. Zhao, *Chem. Commun.*, 2002, 1186
- [54] F. Jiao, A. Harrison, J.C. Jumas, A.V. Chadwick, W. Kockelmann and P.G. Bruce, *J. Am. Chem. Soc.*, 2006, **128**, 5468
- [55] W.C. Li, A.H. Lu, C. Weidenthaler and F. Schuth, *Chem. Mater.*, 2004, **16**, 5676

## *2. Experimental*

Porous single crystal creation has several steps, the first being the synthesis of well ordered mesoporous silica. The metal oxide precursor can then be added into these pores in a variety of methods. Once the PSC is formed, the material can be characterised. The main technique used for this project is high resolution transmission electron microscopy (HRTEM). Other techniques used were; scanning electron microscopy (SEM), X-ray diffraction (XRD) and nitrogen adsorption. Magnetic and catalytic tests were also carried out on the PSC.

### 2.1 Synthesis of mesoporous silica

Four well ordered mesoporous silicas were used as the template for the PSC formation. The syntheses of each of these are as follows.

#### *Synthesis of SBA-15<sup>1</sup>*

4.0 g of Pluronic P123,  $\text{EO}_{20}\text{PO}_{70}\text{EO}_{20}$ , was added into a beaker containing 120 ml of 2 M HCl and 30 ml of distilled water. The beaker was stirred in a temperature probe controlled oil bath at 40 °C until the surfactant is dissolved. Dr Robert Hodgkins (Stockholm University), for the synthesis of SBA-15 fibres, added in 3.36 g Expancel spheres at this stage. Expancel spheres consists of a thermoplastic polymeric shell encapsulating a hydrogen blowing agent.<sup>2</sup> When heat is applied, the polymer shell becomes flexible and the blowing agent exerts pressure, resulting in the expansion of the microspheres. 8.5 g of TEOS (triethoxysilane) was pipetted into the stirring solution and was continued to be stirred at 40 °C for 24 h. The solution containing the white precipitate was poured into a Teflon bottle and matured at 100 °C in an oven for 24-72 h (typically 48 h). The white precipitate was filtered, washed with distilled water and dried at 40 °C overnight.

### *Synthesis of SBA-16<sup>3</sup>*

1.0 g of Pluronic F127, EO<sub>106</sub>PO<sub>70</sub>EO<sub>106</sub>, was dissolved in a solution containing 2 g KCl, 10 ml of HCl (37%) and 50 ml of distilled water whilst stirring at 40 °C. Once dissolved 4.3 g of TEOS was added to the mixture and stirred for 24 h at 40 °C. The solution was then matured at 100 °C for 24-72 h in a Teflon bottle. The sample was then filtered, washed and dried at 40 °C.

### *Synthesis of KIT-6<sup>4</sup>*

1.0 g of Pluronic P123 was dissolved stirring in a solution of 10 ml HCl and 30 ml of distilled water at 40 °C. Once dissolved, 1.0 g of butan-1-ol was added and was stirred for a further 1 h before adding the TEOS (2.15 g). After 24 h, the solution was transferred into a Teflon bottle and matured at 100 °C for 24-72 h. The sample was then filtered, washed with distilled water and dried at 40 °C.

### *Synthesis of FDU-12<sup>5</sup>*

1.0 g of Pluronic F127 was dissolved in a solution containing 2.5 g KCl and 60 ml 2 M HCl. After stirring at 40 °C and once the surfactant was dissolved, 1.0 g of trimethylbenzene (TMB) was added into the solution and stirred for a further 24 h. TEOS (4.15 g) was then added to the solution and stirred for 24 h at 40 °C. The solution was matured at 100 °C for 24-72 h before filtering, washing and drying.

### *Calcination of the mesoporous silica*

The dried mesoporous silica was transferred to a crucible and placed in a muffle furnace. The temperature of the furnace was then increased to 500 °C for 5 h, using a heating rate of 2 °C per minute. The silica was then ready for use.

## 2.2 Synthetic methods of porous single crystals

There are several methods that can be used to create PSCs. Some methods are more adaptable and a lot simpler than others. This section also covers the removal of the template after the formation of the PSC using two different methods.

### *Aminosilylation method*<sup>6</sup>

1.0 g of mesoporous silica was added to a solution containing 30 ml of toluene and 5 ml of APTS (aminopropyltriethoxysilane) and was stirred under reflux at 100 °C for 5-12 h. The solution was allowed to cool to room temperature gradually before the silica was filtered off. Excess organics were removed by washing with toluene three times and then drying at room temperature.

0.3 g of aminosilylated silica was added to a 30 ml aqueous solution, acidified to pH 1.5 (by HCl) containing 3.0 g of a metal oxide salt. The solution was then stirred for 12-72 h, before filtering off. The powder was then washed three times with distilled water and the powder was air dried for 0.5 h.

### *Nitrate method*<sup>7</sup>

1-2.5 mmoles of hydrated metal nitrate was dissolved by stirring in 5-8 g of ethanol. Once dissolved, 0.15 g of the mesoporous template was added to the solution and stirred for a further 2 h. The solution was then transferred into a wide bottomed petri dish and the ethanol was allowed to evaporate at 20-40 °C.

### *Dual solvent method*<sup>8</sup>

1.0 g of mesoporous silica was stirred for 3 h in a dry hexane solvent. 1.0 ml of an aqueous

solution of the metal nitrate was added to this solution under vigorous stirring. The solution was allowed to stir overnight before filtering the sample and drying at 40 °C.

#### *Crystallisation of PSC*

The metal oxide precursor containing mesoporous silica, from the previous steps, was placed in a crucible before being put into a muffle furnace. The temperature was increased at a rate of 1-2 °C per minute to the desired temperature, typically 550 °C. After dwelling for 5 h, the oven was then ramped down to room temperature and the crucible was allowed to cool before removing from the furnace.

#### *Removal of template*

The removal of the silica template was either done by hydrofluoric acid (HF) or sodium hydroxide (NaOH) depending on the metal oxide.

For removing by HF, the sample was transferred into a Teflon bottle and 20 ml of 10 % aqueous HF was added dropwise into the bottle. The solution was then stirred for 8 h or overnight for complete removal of the silica. The sample was transferred into a centrifuge tube then centrifuged for 3 minutes before decanting off the clear liquid and rewashing the powder with distilled water. The sample was centrifuged and washed a further 2 times before extracting from the centrifuge tube with ethanol, which was then evaporated.

For removal of template by NaOH, the powder was transferred to a Teflon bottle and 20 ml of 2 M NaOH was added dropwise into the bottle. The solution was then stirred for 8 h in an oil bath at 70-90 °C. The sample was then centrifuged as before.

## 2.3 High resolution transmission electron microscopy<sup>9-11</sup>

The most important technique used in this project is high resolution transmission electron microscopy (HRTEM). In this section, the basic theory of the electron microscope, as well as such techniques as imaging, selected area electron diffraction (SAED), energy dispersive X-ray spectroscopy (EDX) and dark field imaging are also covered.

### *Sample preparation for HRTEM*

Due to different stabilities in samples, different preparation conditions are required. The most common preparation technique is solvent suspension, with the solvent usually being acetone or ethanol and in a very few cases, water. Acetone tends to be the preferred solvent due to the high evaporation rate. Other methods are dry preparation, for samples unstable in solvents, and scraping, for samples which are thin films. For the PSCs, the sample preparation tended to be the solvent suspension.

To prepare a sample by solvent suspension, the sample is ground up using a pestle and mortar. Acetone is added to the sample and is mixed with the powder. A few drops of the solution can then be dropped onto a holey carbon film supported on a 3 mm copper or gold grid. The solvent was then allowed to evaporate, which deposits the sample onto the film. Figure 2-1 is a diagram of a copper grid with an enlarged section so the holey carbon film can be seen. If the nanomaterial is found to stick together, sonication in the solvent can be used.

If the sample reacts with all the standard solvents, it can be prepared for the TEM by dry preparation. The sample is ground to a fine powder and the copper grid is covered with the powder. The excess is removed by tapping and repeated. This should allow enough particles for analysis.

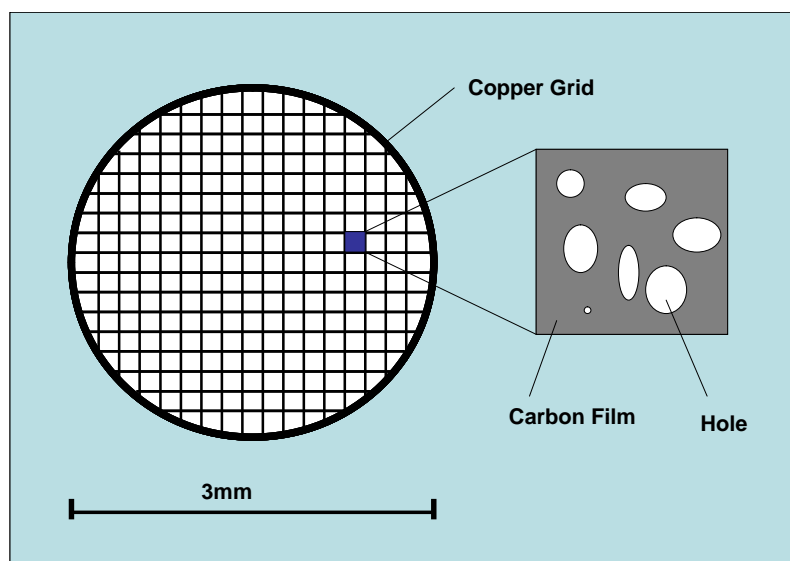


Figure 2-1. A diagrammatic representation of a copper grid supporting a holey carbon film.

Thin films can be scraped directly onto the copper grid using a razorblade. Only a very light scraping is required, to avoid the substrate, which the film sits on, depositing on the grid. A rough check on the deposition of the material can be done using an optical microscope; although only the larger particles will be seen as observing nanomaterial would be too difficult.

### *Theory and operation of the HRTEM*

The electron microscope can use three different electron sources, a plain tungsten (W) filament, a W filament with a LaB<sub>6</sub> crystal tip and a field emission gun. Each offers different levels of brightness, with W filament being the lowest and field emission being the brightest. The filament is held in an uncharged Wehnelt cap (0 kV) and is heated in vacuum to excite the electrons. The anode, situated below the Wehnelt cap, allows for the excited free electrons to be directed through it due to the positive voltage, typically 200 kV. The electrons, when located at the filament, will have a high potential energy and a low kinetic energy until the electron reaches the anode, and beyond, where they will have no potential energy and high kinetic energy. A diagram of the electron gun, using a W filament, can be found in figure 2-2.

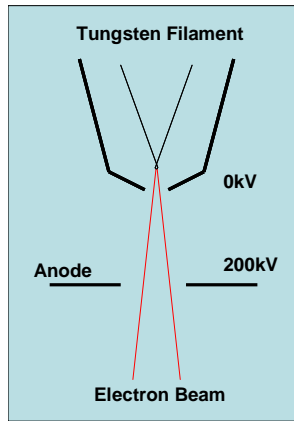


Figure 2-2. Diagram of the electron gun using a tungsten filament. The red line indicates the path of the electrons.

The kinetic energy of an electron (eV), which is the product of half the mass (m) and the velocity (v) squared, can be related to the wavelength ( $\lambda$ ). Since De Broglie's equation shows that the momentum of an electron (p) is equal to the product of mass and velocity and also Planck's constant (h) divided by the wavelength, the wavelength of the electron can be derived. As the voltage is very high, then the velocity of the electron will be comparable to the speed of light and therefore relativistic corrections are needed. This can be seen in a series of equations (2.1-4).

(2.1) The energy of the electron equation, (2.2) De Broglie's equation, which is applied to equation (2.1), (2.3) Wavelength of the electron equation rearranged from equation (2.1) and (2.4) wavelength of the electron with relativistic corrections.

$$eV = \frac{1}{2}mv^2 = \frac{p^2}{2m} = \frac{h^2}{2m\lambda^2} \quad (2.1)$$

$$p = mv = \frac{h}{\lambda} \quad (2.2)$$

$$\lambda = \frac{h}{\sqrt{2meV}} \quad (2.3)$$

$$\lambda = \frac{h}{\sqrt{2m_0eV_r}} = \frac{h}{\sqrt{2m_0eV_0\left(1 + \frac{eV_0}{2m_0c^2}\right)}} \quad (2.4)$$

For 200 kV, the usual operation voltage for the microscopes in the project, the value of the wavelength is 0.00251 nm. With the wavelength being so much smaller than that of light (visible light wavelength ~400 nm), it allows for a greater resolution for nanomaterials.

The electron beam, as it moves down the column, passes through a series of lenses and apertures. The first lens the beam encounters is the condenser lens; this focuses the beam onto the sample. The contrast of the sample can also be changed by using different sizes of the condenser apertures, located below the lens. After the specimen, the beam is refocused by the objective lens, which allows for the diffraction plane to be viewed. The objective aperture can also be used to increase sample contrast and to view dark field imaging. The beam finally passes through the projector lens, which gives the resulting image on the viewing screen. Figure 2-3 shows a diagrammatic representation of the column of an electron microscope.

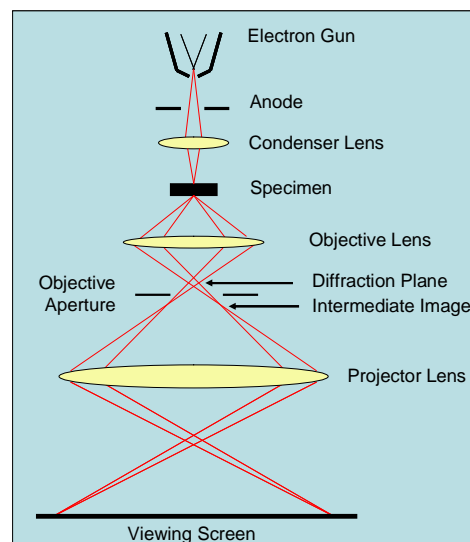


Figure 2-3. Diagrammatic representation of electron beam passing down the column of a TEM.

It is important that the conditions in the column are kept in good order; this includes the alignment of the electron beam. The better the alignment, the better the quality of image resolution. Since it is almost impossible to make a 100 % perfectly curved lens, there is a major defect that has to be addressed called spherical aberration. Even the optical microscope has this defect; however, the magnification is never high enough for it to be a significant effect. The effect ( $\Delta r$ ), which is the difference between where the beam should be, as opposed to where it is, is proportional to the magnification ( $M$ ), the spherical aberration ( $C_s$ ) and the solid angle ( $\alpha^3$ ). This gives us equation (2.5) and the effect of an imperfect lens can be seen in figure 2-4. Since the value of  $\Delta r$  is dependent on the distance between the lens and the image plane ( $b$ ), then the effect ( $\epsilon_s$ ) can be written as equation (2.6). Equation (2.6) can be substituted as the magnification divided by the distance 'b', is equivalent to the reciprocal focal length ( $F$ ). The focal length is the distance between point Q and the lens or length 'a' in the diagram. Additionally, since  $\alpha$  is very small,  $\tan \alpha$  will be roughly equal to  $\alpha$  and therefore the angle will be approximately equal to  $R/F$ .

The derivative of the spherical aberration, equation (2.7), leads to the solving of the total path difference,  $W_s(\alpha)$ , given by equation (2.8).

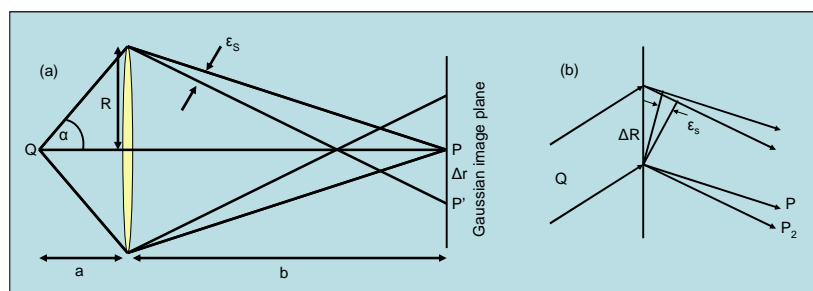


Figure 2-4. (a) A diagram showing the effect of an imperfect lens on distorting the image. (b) The diagram showing how the extent of the path difference between a beam passing through a perfect lens, P, and passing through a lens with a defect, P<sub>2</sub>.

$$\Delta r = MC_s \alpha^3 \quad (2.5)$$

$$\varepsilon_s = \frac{\Delta r}{b} = \frac{MC_s \alpha^3}{b} \approx \frac{C_s R^3}{F^4} \quad (2.6)$$

$$ds = \varepsilon_s dR \quad (2.7)$$

$$W_s(\alpha) = \frac{2\pi}{\lambda} \Delta R = \frac{2\pi}{\lambda} \int_0^R ds = \frac{2\pi}{\lambda} \int_0^R \varepsilon_s dR = \frac{2\pi}{\lambda} \int_0^R \frac{C_s R^3}{F^4} dR = \frac{2\pi}{\lambda} \frac{1}{4} \frac{C_s R^4}{F^4} = \left( \frac{2\pi}{\lambda} \right) \frac{1}{4} C_s \alpha^4 \quad (2.8)$$

To counter this effect, the microscope has to not be in focus conditions but in a defocus condition. The defocus effect can cancel out the phase shift caused by the spherical aberration by creating one of its own,  $W_f(\alpha)$ , shown in Figure 2-5. The effect of the defocus ( $\varepsilon_f$ ) is equal to the product of the effect for length  $b$  ( $\Delta b$ ) and the angle  $\beta$  divided by the distance  $b$ , (2.9). As with  $\alpha$ ,  $\beta$  is very small and therefore is roughly equivalent to  $\tan \beta$ . The defocus phase shift, equation (2.10), can then be used to give Scherzer's formula, (2.11).

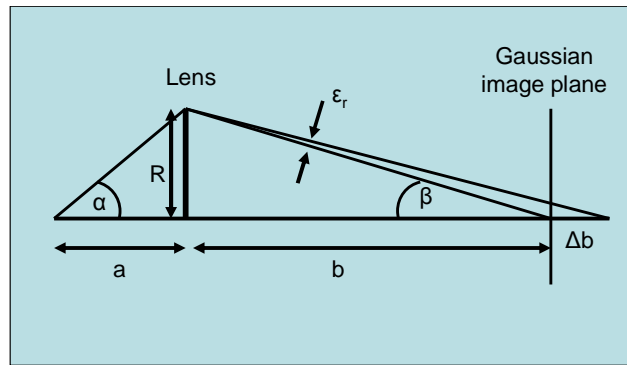


Figure 2-5. Diagram showing how a defect in a lens will put the image behind the Gaussian plane by a factor of  $\Delta b$ .

$$\varepsilon_f = \frac{\Delta b \beta}{b} = \frac{\Delta b R}{b^2} = \frac{\Delta F R}{F^2} \quad (2.9)$$

$$W_f(\alpha) = \frac{2\pi}{\lambda} \int_0^R \varepsilon_f dR = \frac{2\pi}{\lambda} \int_0^R \frac{\Delta F R}{F^2} dR = \left( \frac{2\pi}{\lambda} \right) \frac{1}{2} \Delta F \alpha^2 \quad (2.10)$$

$$\chi(\alpha) = \frac{2\pi}{\lambda} \left( \frac{1}{2} \Delta F \alpha^2 - \frac{1}{4} C_s \alpha^4 \right) \quad (2.11)$$

Using Scherzer's formula, equation (2.11), the phase contrast transfer function (PCTF) can be calculated. Figure 2-6 (a) shows that for Gaussian focus the contrast of the unfocused sample is not present when  $S_1$  is low. Figure 2-6 (b), created from equation (2.12) reveals that for Scherzer focus, with  $S_1$  being larger and positive, that an  $S_2$  is present.  $S_2$  is the interpretable resolution limit, equation (2.14) and where the line crosses the axis is the point resolution. The resolution limit,  $\Delta x$ , can then be calculated with it being the reciprocal of  $S_2$ , (2.15).

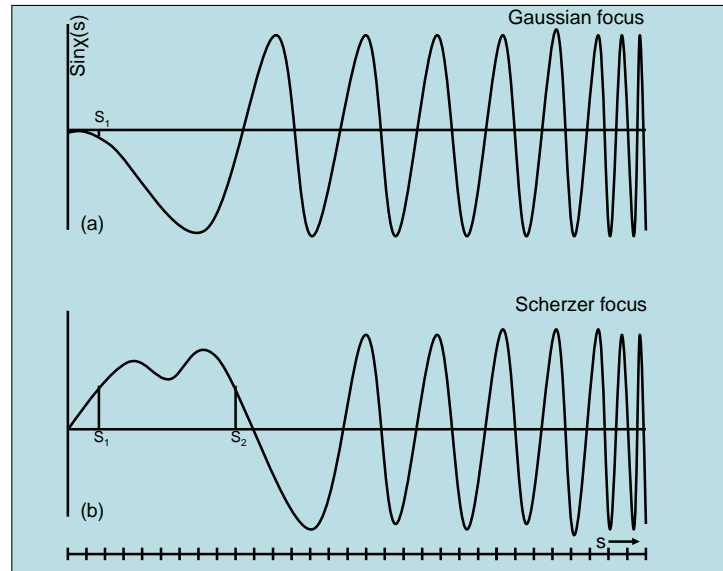


Figure 2-6. (a) Diagram showing that there is no contrast when  $S_1$  is low. (b) Diagram showing that with  $S_1$  being larger and positive, that an  $S_2$  is present.  $S_2$  is the interpretable resolution limit and where the line crosses the axis is the point resolution.

$$\chi(S) = \frac{2\pi}{\lambda} \left( \frac{1}{2} \Delta F \lambda^2 |S|^2 - \frac{1}{4} C_s \lambda^4 |S|^4 \right) \text{ where} \quad (2.12)$$

$$|S| = 2 \sin \frac{\alpha}{\lambda} \approx \frac{\alpha}{\lambda} \quad (2.13)$$

$$S_2 = 1.51 C_s^{-1/4} \lambda^{-3/4} \quad (2.14)$$

$$\Delta x = 0.66C_s^{1/4}\lambda^{3/4} \quad (2.15)$$

The defocus effect, which allows contrast for the sample to be seen, can either be underfocus or overfocus. The underfocus imaging is the correct condition, whereas the over focus is the reverse contrast. The best way to see the difference is by applying the conditions to the same particle. Figure 2-7, shows a TEM image of a hexagonally ordered SBA-15 particle viewed down the [0001] direction. Although (b) gives a more visually pleasing image of a honeycomb structure, the contrast is incorrect as it is overfocus and (a), which is underfocus, gives a more true account to the real life structure. It is worth noting that the pores are white for underfocus and black for overfocus.

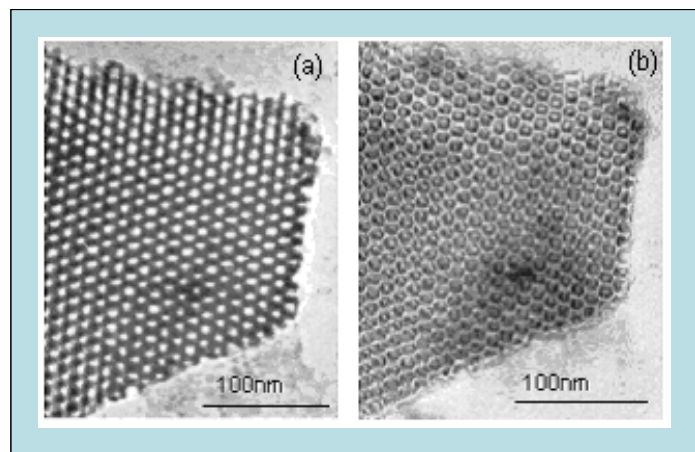


Figure 2-7. TEM images of SBA-15 viewed down the [001] axis with the focus conditions being (a) underfocus and (b) overfocus.

There are three main contrasts in TEM imaging; mass-thickness, diffraction and phase contrast. For mass-thickness contrast, the thicker the sample, the darker the contrast, however the mass of the material has to be taken into account. Materials of high mass, such as heavy atoms and dense crystals, will have an increased chance at scattering the electrons at a high angle. These high angle scattered electrons tend to be removed by the use of an aperture. If only a small

amount of information is obtained then the data will have a low intensity, and therefore darker contrast.

Diffraction contrast is normally seen with crystalline material. This contrast is mainly from the stresses in crystal planes that shift the atomic column out of alignment. The resulting effect, which is caused by the interference of the electron waves, is contrast within the image at these locations. The amount of strain on the atoms will differ from one crystal plane to the next, so this contrast will be affected by crystal orientation. Other effects include; sample preparation, crystal thickness and defects within a crystal. The defects amplify this atomic distortion, making the diffraction contrast very useful for defect investigation.

Diffraction contrast has a limited resolution of 1-3 nm since it is based on the crystal structure stresses. To use the HRTEM to view atomic columns, phase contrast is required. The wavelength of an electron was calculated previously in equation 2.4, although this is for an electron passing unhindered through the vacuum of the microscope. When the electron passes through a crystal, the individual atoms cause the wavelength to change, thus changing the phase of the electron. The electrons that are less affected will result in a different contrast to those that are more affected. The density and thickness of the sample will greatly alter the phase of the electron and therefore show very dark contrasts for both. Additionally, if the sample is too thin, only one atom deep, the effect on the phase of the electron will be too small for a contrast difference.

Since the phase contrast is very much dependent on such a small fluctuation in the electron wavelength, it is clear why the alignment of the beam is important for good imaging of the particle. Just as important for imaging, is the particle itself and the location on the carbon film. For very thick particles, the edge of the particle should be used for imaging as it tends to be thinner than the middle of the particle. The location of the particle can be seen in the diagram of Figure 2-8. There are four locations that a particle can be in; the first, A, is overlapping on the copper wall, this can cause distortion of the image and further TEM activities such as selected

area electron diffraction (SAED) and energy dispersive x-ray spectroscopy (EDX) will be difficult as the copper grid can interfere. B is when the particle is sitting on the carbon film, this poses a problem for atomic imaging as rather than a clear background, the amorphous carbon is surrounding it, however with nanoparticles that are only a few nanometers in scale this can be unavoidable. C is a particle surrounded and overlapped by other particles, although over a hole which would give a clear background, the surface of the particle may be complicated due to the overlap. D is the ideal location, a particle of a reasonable size separated from other particles which is found with an edge over a hole. When it comes to atomic imaging of a crystalline material, not only must the microscope be in good condition and the particle should be in an ideal location, but a good symmetric SAED pattern should be obtained first.

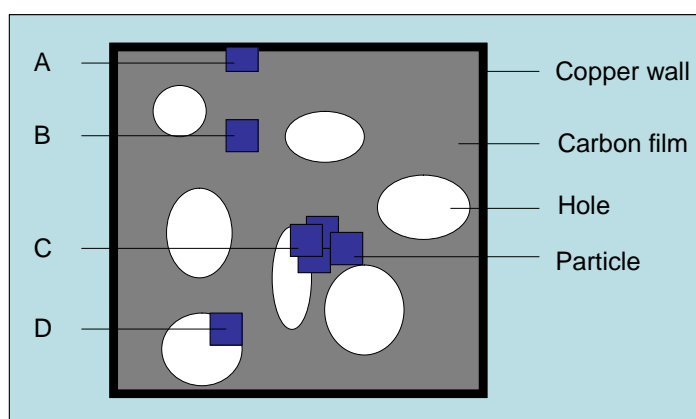


Figure 2-8. Diagram showing the location of particles found on the carbon film on the copper grid. Positions; A overlaps with the wall, B sits only on the carbon film, C surrounded by other particles and D sits over a hole.

SAED determines whether the sample is amorphous or crystalline, and if crystalline whether it is polycrystalline (made up of lot of different crystals) or single crystal (made up of just one crystal). There are three basic patterns for SAED; solid rings that indicate amorphous material, dotted rings indicate polycrystalline material and a 2 dimensional pattern indicates a single

crystal (Figure 2-9). To obtain the best diffraction pattern for a crystal, the specimen needs to be tilted in both the x and y direction. The double tilt sample holder is specially designed to do this.

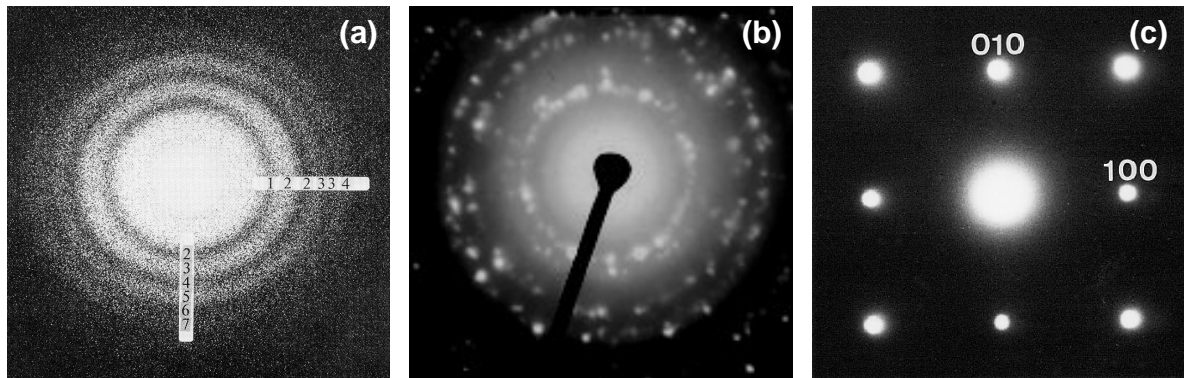


Figure 2-9. Diffraction patterns. (a) Solid ring pattern from an amorphous material. (b) Broken ring pattern from a polycrystalline material. (c) 2D pattern from a single crystal.

By measuring the distance between the diffraction rings or spots, the reciprocal d-spacing can be calculated as shown in Figure 2-10 and equation (2.16) where  $d^*$  is the reciprocal d-spacing,  $D^*$  is the distance between spots on the negative and  $L$  is the camera length. Unlike XRD, the relationship between two spots on a pattern can be directly related to each other and as such, only two independent spots need to be indexed to work out all spot indexes of the pattern. If the unit

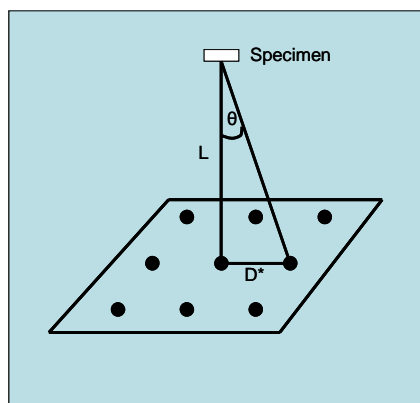


Figure 2-10. Diagram to show how to work out the d-spacing from a diffraction pattern

cell is known then the diffraction pattern can be indexed. If the unit cell is unknown then two or more diffraction patterns of one crystal with different zone axes are required to calculate the unit cell.

$$d^* = \frac{2 \sin \theta}{\lambda} = \frac{D^*}{L\lambda} \quad (2.16)$$

The use of the selected area aperture allows for selecting large or small areas of a crystal. Small apertures are normally quite beneficial for the studying of defects or for removing residual background spots from other crystals. Twin defects can be studied using this method as the aperture can be used either side of the defect and on the defect. Figure 2-11 shows a diagram of an example of the twin defect with the lines indicating change in crystal orientation. The circles represent the selected area aperture and are attached to a corresponding diffraction pattern. The centre pattern is the twin defect pattern, whereas the left and right patterns are from either side of the defect. The diffraction spots are coloured differently so the two patterns can be seen how they make up the twin defect pattern.

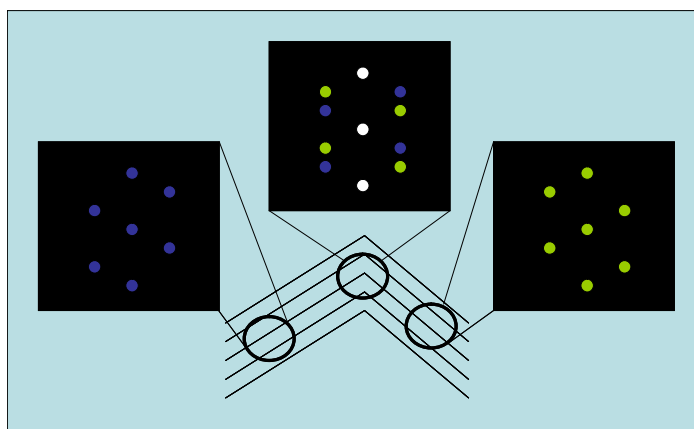


Figure 2-11. Diagram showing the use of selected area on studying defects.

SAED can also reveal superstructure and additionally tell what zone axis the superstructure is on. XRD is unable to do this as superstructure peaks are very weak. Figure 2-12 shows a diagram

of a diffraction pattern with a superstructure of a particle with a cubic unit cell viewed down the [110] zone axis. The figure shows how there is superstructure in the  $(1\bar{1}0)$  direction but not the (001) direction.

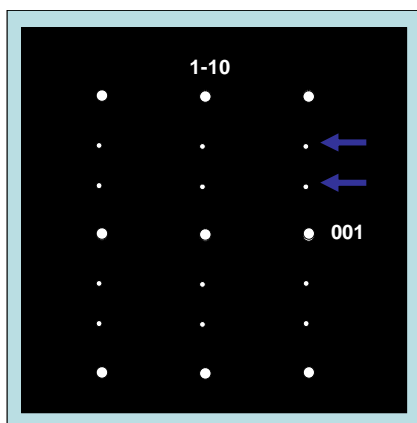


Figure 2-12. Diagram of a diffraction pattern of a cubic crystal viewed down the [110] direction. The blue arrows indicate the superstructure spots.

With the diffraction pattern, the TEM can be switched from bright field, which is the standard for imaging, to dark field imaging which distinguishes between amorphous and crystalline material. This is a very simple technique and is especially useful when looking for nanoparticles in mesoporous silica<sup>11</sup> or crystalline domains in soft templated mesoporous metal oxide<sup>12</sup>.

A diffraction pattern is obtained for the material using the smallest aperture. Normally the (000) spot is moved to the centre, but for dark field imaging a spot that is in the surrounding area is needed. The objective aperture is inserted and is centred on the selected spot, reducing the aperture size until the smallest is obtained. The selected area aperture is then removed and the microscope is switched to imaging. Amorphous material and light atoms will appear dull and hazy whereas the crystalline material or heavy atoms will shine.

The reason for this is due to the majority of amorphous material and the lighter elements only changes the angle of the beam very slightly, whereas the heavier atoms and crystalline material

will deflect the beam to a higher angle. As the deflected beam moves further from the central position, the amount of signal from amorphous material will decrease. By setting the aperture to a diffraction spot, it removes information from the low angle bright field imaging, which can be seen in Figure 2-13. The information that does get through will have the majority coming from the crystal that has that spot and a minor signal from the amorphous material. Similarly, if you have defects in a crystal, there is a possibility of using dark field imaging of one of the defect areas by blocking out the diffraction spots using the aperture of the areas you are not interested in.

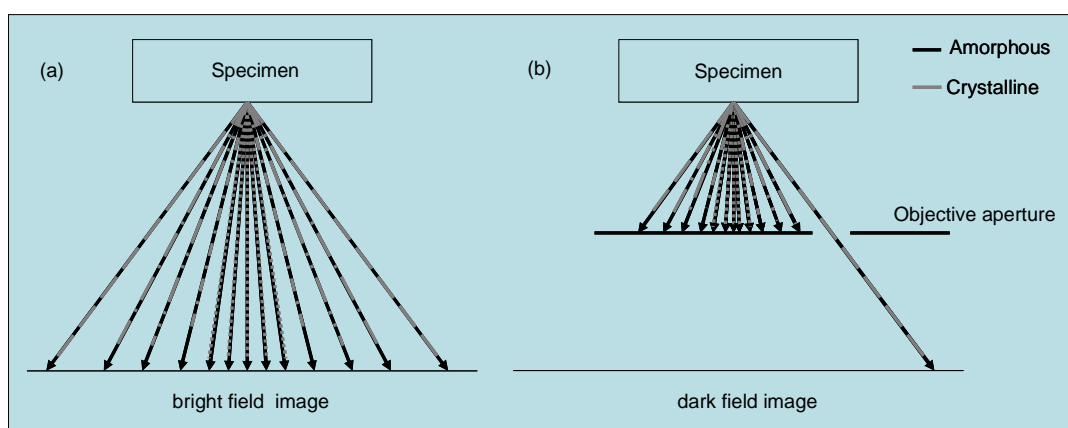


Figure 2-13. Schematic diagram showing information created by the electron beam after going through the specimen. (a) Information for both amorphous and crystalline material is carried equally by low angle beams, with the crystalline information increasing and the amorphous information decreasing at the higher angles. (b) The insertion of the objective aperture removes the low angle beams and the information for bright field imaging.

Figure 2-14 shows how a bright field image can be changed into a dark field image. Although the diffraction pattern is not real, the method used to turn the dark field image was. On the left you have the bright field image of a silicon nanowire with some amorphous material attached, a diffraction pattern (centre) is obtained and the objective aperture is moved from the centre to an off centre spot, on the right is the resulting dark field image. Note the brightness of the crystalline material and the dullness of the amorphous material.

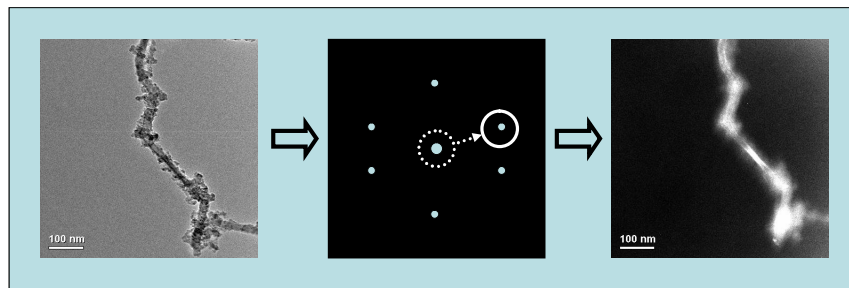


Figure 2-14. Diagram for going from bright field imaging (left) to dark field imaging (right). The dotted circle, the centre, indicates where the objective aperture was before and the solid circle indicates where the aperture was moved to.

Energy dispersive X-ray spectroscopy (EDX) is a powerful tool for determining the elements present and the composition of the material. The spectra from the elements can be quantified in atomic and weight percentage. The impurities in a sample can be determined and the EDX can also be used to examine local defects. If the position of an element in a particular crystal is required, mapping can be used. This allows for elemental distribution within a particle to be viewed.

EDX works by an electron from the gun colliding with an electron from the inner shell of the atom of the specimen, causing this electron to be ejected (Figure 2-15 (a)). Usually the electron that is ejected is from the K-shell, leaving a space for an electron in a higher shell to drop down. When the electron drops from a high level to a lower level, an x-ray is emitted, (Figure 2-15 (b)). The x-ray's energy is determined by the difference in energy between these two shells. As the energy between the levels of an atom varies between elements, the element present can be determined by the x-ray given out. The common x-ray coming from an atom is  $K_{\alpha}$ , which has the energy of an electron going from the L-shell to the K-shell.  $K_{\beta}$ , an electron going from the M-shell to the K-shell and  $L_{\alpha}$ , M-shell to L-shell, can also normally be seen.

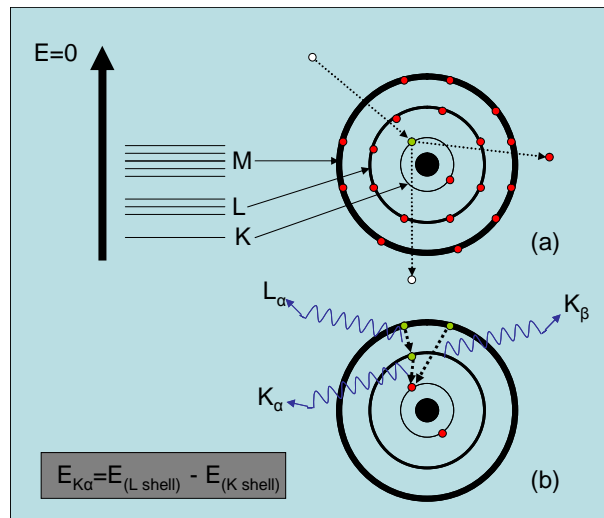


Figure 2-15. (a) Diagram of a bombarding electron knocking out a K-shell electron. (b) Diagram of electrons, from a higher shell, moving down into the space in the K-shell and the corresponding x-ray energies.

### *Jeol JEM-2000fx*

The Jeol JEM-2000fx electron microscope operates at 200 kV using a W-filament. It has a top magnification of 850,000 X with a resolution of 0.18 nm. There is a built in camera to take images and diffractions. Other than the single tilt sample holder, the TEM also comes equipped with a  $\pm 30^\circ$  double tilt holder.

### *Jeol JEM-2011*

The Jeol JEM-2011 electron microscope operates at 200 kV using a LaB<sub>6</sub>-filament. The resolution is 0.18 nm with a top magnification of 1,500,000 X. Along with the built in camera for diffraction patterns, there is a Gatan CCD camera attached for digital micrographs. Also attached is an Oxford Instruments EDX system for spectral analysis as well as a semi-STEM for elemental mapping. The double tilt holder has a  $\pm 20^\circ$  range.

## 2.4 Scanning electron microscopy

The HRTEM is able to study the mesopore structure and crystal structure, however the scanning electron microscope (SEM) is needed to study the three dimensional topography of the PSC material. The SEM can also be used for EDX of the sample.

### *Sample preparation for SEM*

Powder samples for the SEM are prepared by grinding in a mortar and pestle. A double- sided sticky carbon tab is adhered onto a brass stub and the protective plastic is removed from the other sticky side. A small amount of the powdered sample is spread across this tab and the stub is placed in a sample holder.

If the sample is found to be charging too much and imaging is difficult then gold sputtering is required. The stub with the sample is placed in a vacuum chamber with a tungsten coil containing a piece of gold foil. The coil is heated slowly and at a certain temperature it vapourises the gold, coating the sample.

### *Theory and operation of the SEM*

The SEM works similarly to the TEM, although instead of transmitted electrons for the imaging, it uses backscattered electrons. This allows for thicker samples to be used and such information as specimen topography, magnetic contrast and voltage contrast can be studied. Figure 2-16 is a block diagram of the SEM chamber. The electron gun emits the electrons down the column and the electron beam is focussed by a series of lenses. The final lens the electron passes through is linked to the magnification. The electrons come in contact with the sample and are backscattered into a collector. The information is then amplified before appearing on a

computer monitor using the SEM software. The computer is then used to change the conditions of the sample which it relays to the final lens.

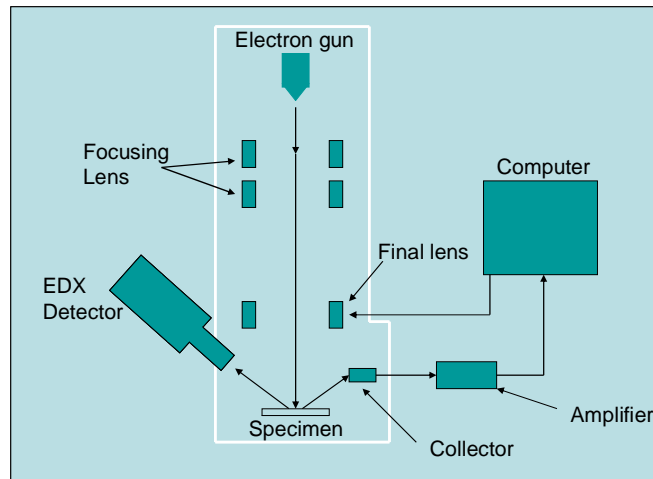


Figure 2-16. Block diagram of the inside of a scanning electron microscope.

When the sample is non-conducting, there can be a charge effect. Figure 2-17 shows an example of this charging effect. If the amount of electrons striking the sample is less than the amount that back scatter, then the sample is becoming positively charged and if it is more than the backscattered electrons, the sample will become negatively charged. Only when the sample is conducting that this charge effect will be lost at high voltage.

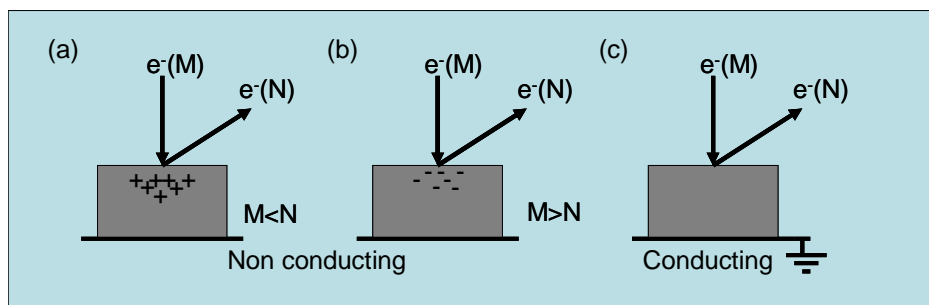


Figure 2-17. Diagram of samples charging under the electron beam. When the electron beam strikes a non-conducting sample, it can either (a) lose electrons becoming positively charged or (b) gain electrons becoming negatively charged. If the sample is conducting, (c), then no charging should be present.

There are two methods to combat the charging effect, either a low voltage can be chosen or the sample can be coated with carbon or gold. For using a low voltage, it has the advantage of the sample keeping the original surface. However, it is difficult to find a suitable voltage for the sample and also leads to a reduction in the resolution. The coating method results in getting a good conducting surface. However, it is extremely difficult to get a coating that is not too thin and not too thick (Figure 2-18). If the sample is too thin then there will still be a charging effect and if the sample is too thick then you will lose the original topography of the sample.

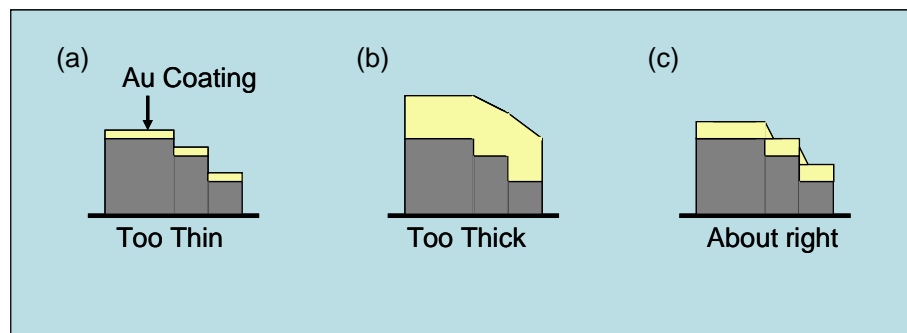


Figure 2-18. Diagram of gold coating an SEM sample with the coating being (a) too thin, (b) too thick and (c) about right.

Image contrast of the sample consists of three parts; the brightness of the beam, the received intensity at the detector and the contrast between two parts of the sample (2.17-19). The brightness of the beam ( $\beta$ ) is proportional to the beam current ( $i$ ) and inversely proportional to the area ( $0.25\pi d^2$ ) and the solid angle ( $\pi\alpha^2$ ), where  $d$  is the beam diameter and  $\alpha$  is the beam divergence.

$$\beta = \frac{\text{current}}{(\text{area})(\text{solidangle})} = \frac{4i}{\pi^2 d^2 \alpha^2} \quad (2.17)$$

The received intensity at the detector ( $I_D$ ) is equal to the intensity of the source ( $I_S$ ) multiplied by the sum of the product of the relation between the source and object ( $R_{SO}$ ) the energy of the signal received ( $E$ ) and the relation between the object and the detector ( $R_{OD}$ ) with other factors such as background noise ( $N$ ). The contrast between two different parts of the sample ( $C_0$ ) is the difference between the received intensities of these areas ( $I_D$  and  $I'_D$ ). The energy received at the detector will depend on the type of sample, for example the energy received will be different in a sample for a signal coming from a positive electrode than with a negative electrode (Figure 2-19 (a)). The height difference in a sample also effects the relations between both the source/object and object/detector. Figure 2-19 (b) shows, with four sites on a sample, how the relation between the source and object can be similar (A and D) or different (A and B) and also the relation between the object and detector can be similar (C and D) or different (A and D).

$$I_D = I_S \sum (R_{SO} \times E \times R_{OD}) + N \quad (2.18)$$

$$\frac{I'_R}{I_R} = \left( \frac{R'_{SO}}{R_{SO}} \right) \left( \frac{E'}{E} \right) \left( \frac{R'_{OD}}{R_{OD}} \right) = C_0 \quad (2.19)$$

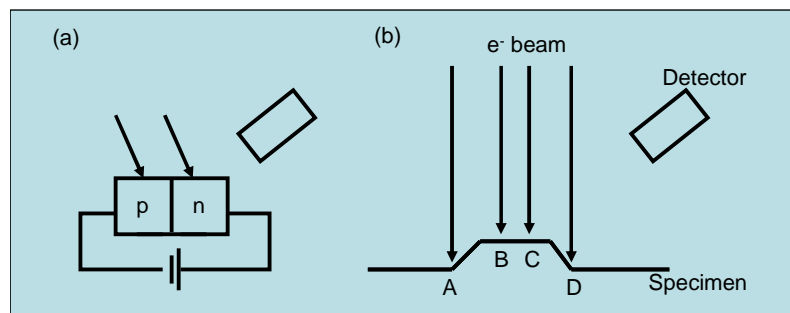


Figure 2-19. Diagram showing how the sample can affect the image contrast by having either (a) different electrical properties or (b) varying heights in topography.

When a sample has extensive topography, the depth of field mode can be used. This allows looking at the structure below the sample's surface. Figure 2-20 is a diagram for how the depth of

field can be altered and is explained using the following equations. The depth of field ( $D$ ) is approximately equivalent to the beam size ( $r$ ) divided by the beam divergence ( $\alpha$ ) multiplied by a factor of two (2.20). The beam size, which can also be seen as the picture element, is the minimum Cathode ray tube (CRT) spot size (0.1mm) divided by the magnification ( $M$ ) (2.21). Since the angle of beam divergence is so small, then  $Tan \alpha$  is approximately equal to  $\alpha$  and therefore is equal to the radius of the aperture ( $R$ ), divided by the working distance ( $WD$ ) (2.22). This gives the depth of field being proportional to the working distance and inversely proportion to both the aperture size and magnification (2.23). However, there is a loss of resolution and to see details at higher magnification, the working distance needs to be reduced to increase the resolution. Figure 2-21 shows an object with three levels, a high working distance allows us to see the three dimensional image of the object due to the increase in depth of field. When wanting to study at higher magnifications, a lower working distance is required and although decreasing the depth of field, it increases the resolution allowing defects to be seen. The aperture size should be altered to give the optimum beam divergence ( $\alpha_{opt}$ ), which minimises the various aberrations of the lenses, as it is the cube root of the beam size divided by the spherical aberration of the lenses ( $C_s$ ) (2.24).

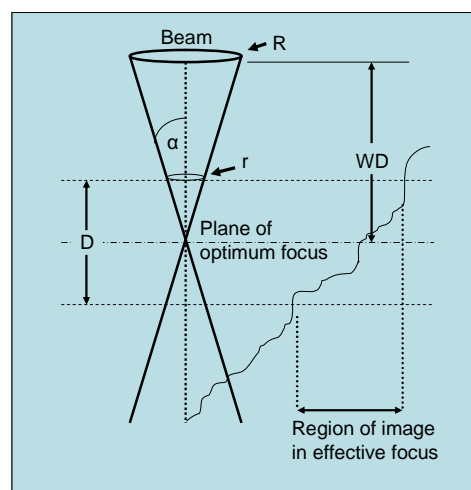


Figure 2-20. Diagram showing how the depth of field ( $D$ ) can be altered by choosing a smaller aperture size ( $R$ ) and a long working distance ( $WD$ ).

$$\frac{D}{2} \cong \frac{r}{\alpha} \quad (2.20)$$

$$r = \frac{0.1mm}{M} \quad (2.21)$$

$$\alpha = \frac{R}{WD} \quad (2.22)$$

$$D = \frac{2r}{\alpha} = \frac{0.2mm}{\alpha M} = \frac{(0.2mm)(WD)}{RM} \quad (2.23)$$

$$\alpha_{opt} = \left( \frac{d}{C_s} \right)^{1/3} \quad (2.24)$$

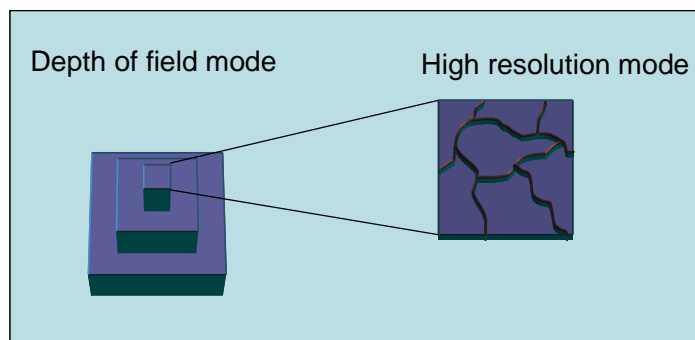


Figure 2-21. Diagram showing the difference between having a high depth of field with low resolution (left) and low depth of field but a high resolution (right).

### *Jeol JSM-5600*

The Jeol JSM-5600 scanning electron microscope operates in the range of 5-30 kV with a W-filament as the electron source. Maximum magnification is 300,000 X with a resolution of 3.5 nm. Specimen tilting range is  $-10^{\circ}$  to  $+90^{\circ}$  and specimen rotation is  $360^{\circ}$ . The SEM is controlled via a computer and also has EDX facility from Oxford Instruments attached.

## 2.5 X-ray diffraction<sup>13</sup>

Whilst the HRTEM can look at local crystal structures, it is always worth looking at the bulk sample so that the major crystal phase can be established. Particle size can also be calculated from the X-ray diffraction (XRD).

### *Sample preparation for reflective XRD*

The sample is ground up using a pestle and mortar, before being transferred to a metal plate with a shallow pit and packed fully. A glass slide is used to level off the excess sample and smooth the surface. Figure 2-22 (a) is an example of the metal plate.

### *Sample preparation for transmission XRD*

Two plastic discs were spread with a thin layer of petroleum jelly. A small amount of ground up sample was sandwiched between the plastic discs. An XRD disc was opened up by removing the inner metal disc and the plastic discs were placed inside. The inner disc was then replaced holding the sample in the central position. Figure 2-22 (b) is an assembly diagram of this procedure.

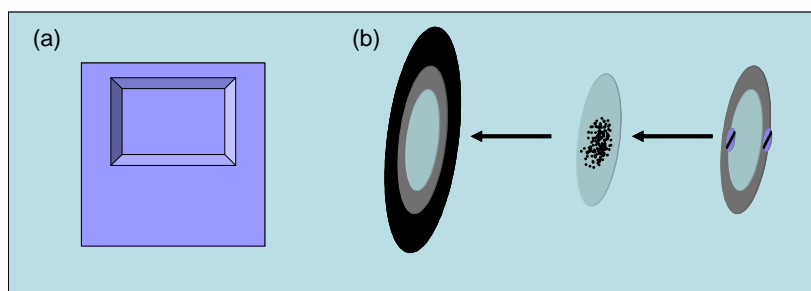


Figure 2-22. Diagram showing XRD sample holders. (a) A reflective XRD plate with a shallow pit for the sample.

(b) A transmission XRD disc assembly diagram.

### Theory and operation of XRD

The generation of X-rays is very similar to the EDX. A tungsten filament is heated up and electrons are emitted and attracted towards an anode made of copper. The copper atom loses an electron and when the vacancy is filled with a higher energy level electron, X-rays are emitted. Typically, the X-ray collected is Cu  $K_{\alpha}$  which has a wavelength of 0.154 nm. Cu  $K_{\alpha}$  can be in two slightly different states,  $K_{\alpha 1}$  and  $K_{\alpha 2}$ , which have wavelengths of 0.15406 and 0.154439 nm respectively, with the average wavelength being 0.15418 nm. Figure 2-23 (a) is a schematic diagram of the X-ray tube with a monochromator attached, this is typical for transmission XRD but absent in reflective XRD.

For reflective XRD, the tube will direct the X-rays at the sample, the crystal structure will then deflect the X-rays at an angle towards the detector. The window for the detector has a diffracted beam monochromator, which is a cover over the detector window with a narrow slit that allows Cu  $K_{\alpha}$  X-rays through but not Cu  $K_{\beta}$  (Figure 2-23 (b)). The detector, which rotates to different angles will then record the number of counts at a certain angle and relay this to the computer. A spectrum can then be calculated, with intensity against angle ( $2\theta$ ).

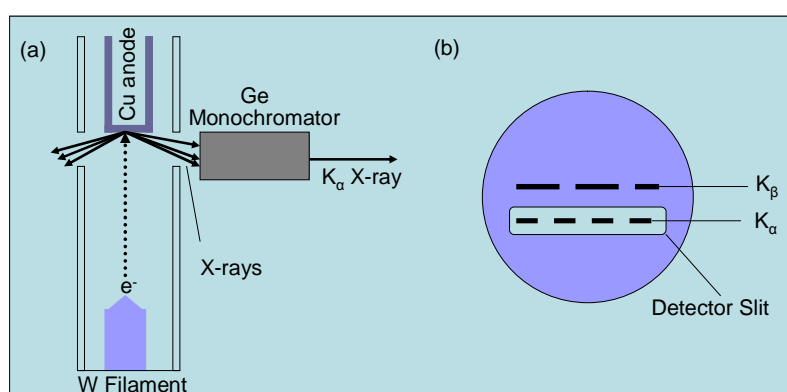


Figure 2-23. Schematic diagram of (a) the X-ray tube of a transmission XRD with a monochromator attached. The X-ray tube is the same for reflective XRD with the exception of the monochromator. (b) Diagram of diffracted beam monochromator for reflective XRD.

For transmission XRD, the X-rays, which will include the Cu  $K_{\alpha}$  X-ray, will pass through a monochromator, typically a crystal of a specific orientation, to take away the unwanted X-rays, for example Cu  $K_{\beta}$ , and leave the desired X-ray. This allows for a greater resolution than for when using the diffracted beam monochromator. The X-ray will then pass through the sample and into the detector. Figure 2-24 is a schematic diagram to show (a) reflective XRD and (b) transmission XRD.

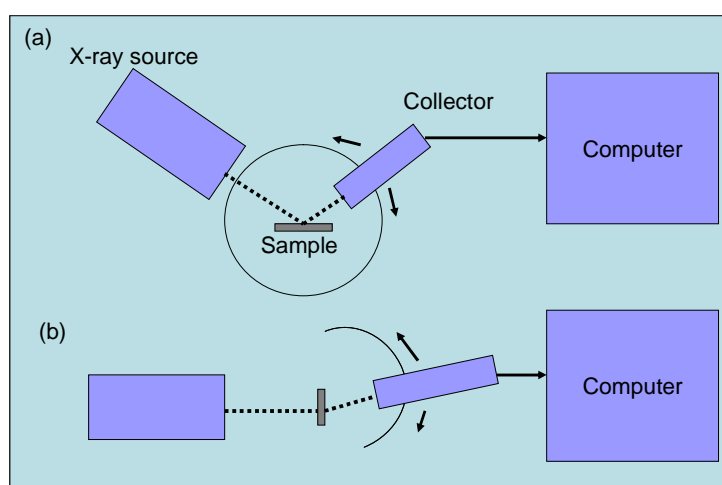


Figure 2-24. Schematic diagram of (a) reflective XRD and (b) transmission XRD

When the X-ray hits the sample, a crystalline sample will randomly scatter the X-rays. Using Bragg's law, the scattered X-rays are able to be constructively recombined in the form of a pattern. The diagram that leads to the Bragg equation (2.25) can be seen in Figure 2-25, where  $XYZ$  is equal to  $n\lambda$ . The Bragg equation states that the product of the diffraction order ( $n$ ) and the wavelength ( $\lambda$ ) is equal to twice the product of the distance between the lattice planes ( $d$ ) and the sine of the diffraction angle ( $\sin\theta$ ).

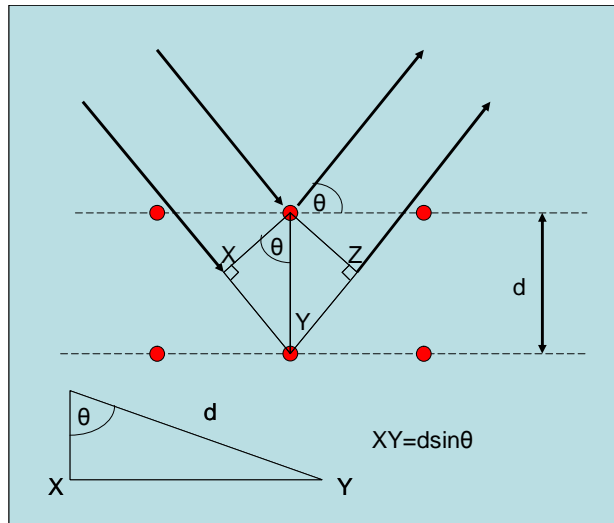


Figure 2-25. Schematic diagram of how the Bragg equation is derived from a crystal structure.

$$n\lambda = 2d \sin \theta \quad (2.25)$$

Crystal size can also be calculated from the XRD pattern by the peak width, using the Debye-Scherrer formula (2.26). As a particle gets smaller towards the nanosize, the width of the peak increases. The average crystallite size can be determined by the product of the shape factor ( $k$ ) and the wavelength of the X-ray ( $\lambda$ ) divided by the product of the full width at half maximum in radians ( $\beta$ ) and the cosine of the angle of point of maximum diffraction (2.26). The shape factor tends to be in the region of 0.8-1.39, although will typically be 0.9. Due to this shape factor, there tends to be a large error of ~50%.<sup>12</sup> The wavelength for the copper X-rays will typically be 0.154056 nm ( $K_{\alpha 1}$ ) in transmission XRD and 0.15418 nm ( $K_{\alpha 1}$  and  $K_{\alpha 2}$ ) for reflective XRD.

$$D_{hkl} = \frac{k\lambda}{\beta \cos \theta} \quad (2.26)$$

#### *Philips reflective diffractometer*

The Philips reflective diffractometer uses a tungsten filament and a copper anode operating at 40 kV. The collector detects copper  $K_{\alpha 1}$  and  $K_{\alpha 2}$  x-rays of average wavelength 0.15418 nm using a diffracted beam monochromator or secondary monochromator.

### *Stoe transmission diffractometer*

The Stoe transmission diffractometer uses a tungsten filament and copper anode operating at 40 kV. It uses only copper  $K_{\alpha 1}$  x-rays of wavelength 0.154056 nm using a primary Ge monochromator.

## 2.6 Nitrogen adsorption- isothermic gravimetric analysis

The mesoporous nature of the PSC material as well as the silica material can be investigated by nitrogen adsorption isothermic gravimetric analysis (IGA), revealing the surface area, pore size distribution, using the BJH model, and pore volume of the material.<sup>14</sup>

### *Sample preparation for IGA*

A metal boat was tared in the sealed isotherm chamber before measuring in 10-15 mg of mesoporous sample. The system was then sealed with the metal boat containing the sample inside. The sample was then degassed at 393 K for 2 h before returning the sample to room temperature for accurate weight measurement of sample. The sample was then cooled by liquid nitrogen and gravimetric nitrogen adsorption data was collected at 77 K.

### *Theory and operation of IGA*

Many gases can be used for adsorption although nitrogen was the standard for this project. The nitrogen will flow through the pores of the mesoporous sample, depositing a monolayer of nitrogen on the surface. As the pressure inside the pores increase, the nitrogen builds up into a multilayer coverage. As the multilayer gets larger, and the pressure increases, capillary condensation can occur, causing a steep incline in the isotherm graph. Once the pore is fully

filled, the isotherm graph will level off. The standard mesopore isotherm is classed as type IV. After the adsorption, desorption can be carried out.

Nitrogen desorption works in the same way as adsorption but in reverse, giving a very similar looking type IV isotherm graph. When the desorption and adsorption data are put together, hysteresis loops can be created. The two main types of hysteresis loops experienced in this project are H1 and H2 (Figure 2-26). H1 is typical for mesoporous material with cylindrical pores, SBA-15, and H2 is typical for mesoporous caged structures, SBA-16. The reason for the two types of hysteresis is due to the difference between the adsorption and desorption of the two types of material. For H1, the cylindrical channels have relatively the same diameter all along the pore, so the filling of the pores will occur quite rapidly. For H2, the cage structure has large chambers and small connecting windows, when the nitrogen fills these cages it takes a long time for capillary condensation. During the desorption, since the nitrogen can only be released through the very small windows, it takes a much smaller pressure to release the nitrogen from the chambers than it did to fill them.

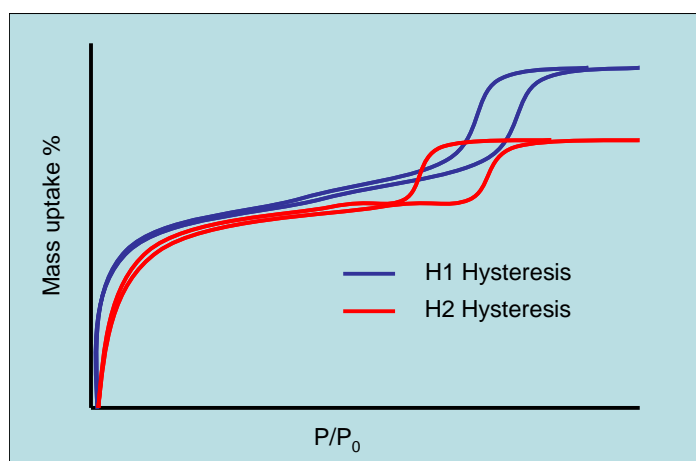


Figure 2-26. Diagram of type IV isotherms with hysteresis loops for cylindrical mesopores (H1) and mesocages (H2).

From the isotherm data, a whole host of information can be received. Surface area, pore size distribution, pore volume as well as the presence of micropores. The surface area of the mesoporous silica and the PSC can then be compared.

#### *Hidden microanalysis machine*

The Hidden microanalysis machine is an IGA-II series automated gravimetric analyser. The machine typically operates with nitrogen gas at relative partial pressure of the range 0.0-1.0

## 2.7 Magnetism<sup>15</sup>

Since the PSC's bulk size is made up of a nanostructure, their magnetic properties were investigated.

#### *Sample preparation for the magnetometer*

Approximately 10-100 mg of the sample was weighed into a gelatine capsule of known low magnetic response. The capsule was then sealed and inserted into a drinking straw, and held in place using two smaller pieces of a drinking straw. The straw was then loaded onto the immersion rod and dipped into the evacuation chamber. Since oxygen is magnetic, the system is purged with helium before the full insertion into the machine.

#### *Theory of magnetism*

When applying a magnetic field to a sample, the sample's magnetism can be investigated. A magnetic material can exhibit a diamagnetic or paramagnetic response. The magnetic susceptibility is proportional to the magnetisation of the sample and inversely proportional to the strength of the field (2.27). When the magnetisation opposes the magnetic field, the magnetic

susceptibility is less than zero and is called diamagnetism. Then the magnetisation is added to the field, the magnetic susceptibility is positive and is called paramagnetism.

Diamagnetic material will only have a magnetic response when an external field is applied. However, paramagnetic material will have a magnetic response even in the absence of an applied field. The material tends to have a permanent dipole moment, which is commonly seen in metals due to the unpaired electrons in the atomic orbital. It is due to this unpaired electron response that helium, which has only paired electrons, is used as the gas instead of oxygen, which has 2 unpaired electrons, when studying the magnetism of the material. When a material is purely paramagnetic, the individual dipoles from the atoms will not interact with each other and are entirely random in orientation. When the dipole moments do interact, ferromagnetism and antiferromagnetism is the result.

In ferromagnetism, the dipoles align with each other, with the spins being in the same direction, in the absence of an applied field. Since electrons that are aligned are spinning in the same direction, there is a small repulsion that will lower the electrostatic energy and this leads to nearby electrons also aligning with these electrons. This alignment is only short range though and over a longer range a neighbouring region may be antialigned. When neighbouring dipoles antialign, this is different to ferromagnetism and is called antiferromagnetism.

Antiferromagnetism is less common than ferromagnetism, and occurs at a lower temperature. As the temperature decreases, the antiferromagnetic response can typically become diamagnetic and also exhibit some ferromagnetic behaviour. Both ferromagnetic material and antiferromagnetic material will spontaneously align or antialign below a certain temperature. Above this temperature, both types of magnetism tend to become paramagnetic, as the mobility of spin increases and therefore spontaneous alignment can not occur. For ferromagnetic material, this is the Curie temperature and for antiferromagnetic material, it is the Néel temperature, which

are analogous to each other. A magnetometer can be used below these temperatures to apply a field to study the materials behaviour.

Magnetic coils are assigned a magnetic field and the sample is placed between them, see Figure 2-27. By moving the sample in and out of these fields, the magnetic susceptibility can be calculated. The magnetic susceptibility ( $\chi$ ) is equal to the magnetism of the sample ( $M$ ) divided by the applied field ( $H$ ), (2.27). The magnetic susceptibility can also be seen by using the Curie-Weiss law (2.28). Using this law, the magnetic susceptibility is a constant ( $C$ ) divided by the temperature ( $T$ ) in Kelvin minus the sign and strength of the coupling ( $\theta$ ), where the constant  $C$  is the square of the magnetic moment ( $\mu$ ) divided by 8 (2.29). By altering the temperature, the susceptibility will increase.

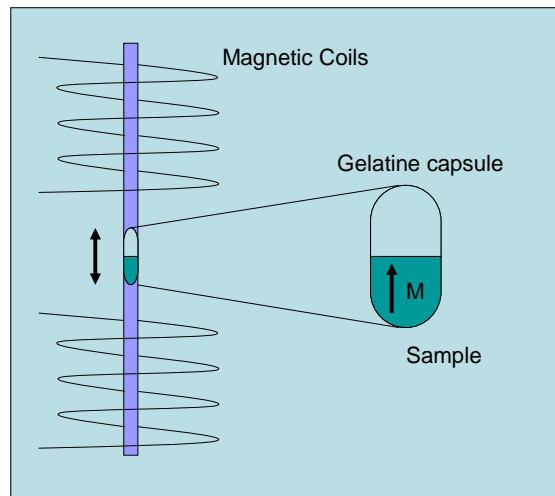


Figure 2-27. Diagram of sample inside the coils in a magnetometer.

$$\chi = \frac{M}{H} \quad (2.27)$$

$$\chi = \frac{C}{(T - \theta)} = \frac{\mu^2}{8(T - \theta)} \quad \text{Where} \quad (2.28)$$

$$C = \frac{\mu^2}{8} \quad (2.29)$$

## 2.8 Catalysis

Due to the easily manageability of the PSC being bulk in size whilst still retaining nanoproperties, the catalytic activities of the PSC are of interest.

### *Preparation of sample for oxidation of cyclohexene*

0.05 g of PSC was added to a stainless steel autoclave containing 0.74 mmol of cyclohexene, 2.08 g of 2,2-dimethylpropanol and 25 ml of toluene as solvent. The reactor was purged with pure oxygen and pressurised to 10 bar. The contents were stirred at 85 °C for 16 h before the solution was analysed using a gas chromatography-mass spectrometer.

### *Nanomaterials in catalysis*

The ability to retrieve the catalyst from reactants and products and being able to reuse it has always been of interest in catalysis.<sup>16</sup> The less complicated the procedure, the higher ability for it to become an effective industrial application. This is one of the main advantages in heterogeneous catalysis as different phases are so easy to separate.

For the past 80 years, there has been the use of nanoparticles in the catalytic industry.<sup>17</sup> The main concentration was on the rate of reaction, which obviously since the smaller the material the greater the surface area (gram for gram). However, the focus has now changed to look at the selectivity of catalysts in reactions. By using nanosized catalysts, a better selectivity for products from bulk catalysts can be achieved. It has already been mentioned in sections 1.4 and 1.5 about the use of mesoporous material as hosts for catalysts, and in section 1.8 about using mesoporous PSC as catalytic material. The nanosized pores not only allow for support of the nanoparticles but

the size of the pores allow for the selectivity in the size of the reactants that can enter the pores. Since nanoparticles have well defined crystal faces, they tend to exhibit the ability of single crystals. This avoids active sites having a wide range of reactivities, as nanoparticles have the ability to restructure their full atomic structure which is absent in bulk material as they tend to only restructure the surface. Despite this, two main problems for nanosized catalysts tend to always be present. The first is the ability of needing a support to allow for the catalysts to be easily transferable and the second is the aggregation of the nanomaterial.

When the material is supported, it is important for the support to not play a major role in the catalysis, as since the support is normally bulk material then it can reduce the selectivity of the reaction.<sup>18</sup> If the nanomaterial in the support is not immobilised in some way, the particles can aggregate together and become bulk material, thus losing their nanoproperties. This can be done by capping the nanomaterial altering the surface using ligands, but like the support selection, it is important to find a ligand that is not detrimental to the catalysis and the selectivity.<sup>19</sup>

As explained in section 1.8, the PSC is bulk in size but has nanoproperties. Due to the interconnecting frameworks of the PSC, the material is able to support itself and does not need a secondary material for support. This results in the catalytic activity in a reaction will only be coming from the PSC and not from a supporting material. Since the bulk size of the PSC is made up of the nanomaterial framework, aggregation of the particles will not cause the loss of the nanoproperties as the pore structures should remain intact and therefore retaining the desirable properties. Another added advantage of the PSC is the ability to most likely be more stable than polycrystalline material. Since the crystal structure is over such a relatively vast area, it is less likely to break down over prolonged use than that of the polycrystalline material. With the above techniques, the study of the characterisation and properties of these PSCs were carried out.

## References

- [1] D.Y. Zhao, J.L. Feng, Q.S. Huo, N. Melosh, G.H. Fredrickson, B.F. Chmelka and G.D. Stucky, *Science*, 1998, **279**, 548
- [2] M. Ahmad, *J. Vinyl Addit. Technol.*, 2001, **7**, 156
- [3] D.Y. Zhao, Q.S. Huo, J.L. Feng, B.F. Chmelka and G.D. Stucky, *J. Am. Chem. Soc.*, 1998, **120**, 6024
- [4] F. Kleitz, S.H. Choi and R. Ryoo, *Chem. Commun.*, 2003, 2136
- [5] J. Fan, C.Z. Yu, F. Gao, J. Lei, B.Z. Tian, L.M. Wang, Q. Luo, B. Tu, W.Z. Zhou and D.Y. Zhao, *Angew. Chem. Int. Ed.*, 2003, **42**, 3146
- [6] K.K. Zhu, B. Yue, W.Z. Zhou and H.Y. He, *Chem. Commun.*, 2003, 98
- [7] B.Z. Tian, X.Y. Liu, H.F. Yang, S.H. Xie, C.Z. Yu, B. Tu and D.Y. Zhao, *Adv. Mater.*, 2003, **15**, 1370
- [8] K. Jiao, B. Zhang, B. Yue, Y. Ren, X.Y. Liu, S.R. Yan, C. Dickinson, W.Z. Zhou and H.Y. He, *Chem. Commun.*, 2005, 5618
- [9] P.B. Hirsch, A. Howie, R.B. Nicholson, D.W. Pashley and M.J. Whelan, '*Electron Microscopy Of Thin Crystals*', 1971
- [10] J.C.H. Spence, '*High-Resolution Electron Microscopy*', 2004
- [11] M. Andersson, H. Birkedal, N.R. Franklin, T. Ostomel, S. Boettcher, A.E.C. Palmqvist and G.D. Stucky, *Chem. Mater.*, 2005, **17**, 1409
- [12] P.D. Tang, D.Y. Zhao, D.I. Margolese, B.F. Chmelka and G.D. Stucky, *Nature*, 1998, **396**, 152
- [13] R. Jenkins and R.L. Snyder, '*Introduction To X-ray Powder Diffraction*', 1996
- [14] E.P. Barrett, L.G. Joyner and P.P. Halenda, *J. Am. Chem. Soc.*, 1951, **73**, 373
- [15] A.F. Orchard, '*Magnetochemistry*', 2003
- [16] J.A. Gladysz, *Pure Appl. Chem.*, 2001, **73**, 1319

- [17] G.A. Somorjai and Y.G. Borodko, *Catal. Lett.*, 2001, **76**, 1
- [18] Z. Xu, F.S. Xiao, S.K. Purnell, O. Alexeev, S. Kawi, S.E. Deutsch, B.C. Gates, *Nature*, 1994, **372**, 346
- [19] S. Kundu, A. Pal, S.K. Ghosh, S. Nath, S. Panigrahi, S. Praharaj, S. Basu and T. Pal, *J. Nanopart. Res.*, 2005, **7**, 641

### *3. Porous Single Crystal of Chromium Oxide*

As mentioned before, chromium oxide was the first PSC formed using SBA-15 as a template. This used a two-step reaction using firstly the aminosilylated method followed by the impregnation of the potassium dichromate. Other templates and methods have been used in the synthesis of chromium oxide PSC. The dual solvent method, also a two-step reaction, has been used with the KIT-6 template and the ethanol method in which only one-step is required.

#### 3.1 Synthetic methods for PSCs

##### *Aminosilylation method<sup>1</sup>*

1.0 g of mesoporous silica was added to a solution containing 30 ml of toluene and 5 ml of APTS (aminopropyltriethoxysilane) and was stirred under reflux at 100 °C for 8 h. The solution was allowed to cool to room temperature gradually before the silica was filtered off. Excess organics were removed by washing with toluene three times and then drying at room temperature.

The APTS is anchored onto the silanol groups in the wall of the template by a condensation reaction. During the refluxing in the solvent, the ethoxide group hydrolyses to become hydroxyl groups. The two silanol (Si-OH) groups, one from the wall and the other from the organic, will react with each other and form a Si-O-Si bond attaching the organic group to the wall, with the by-product of water.

The amount of APTS allowed to attach to the walls is directly related to the presence of silanol groups on the wall of the silica. As discussed in the previous section, the removal of the surfactant from the mesoporous silica template will leave varying amounts of silanol groups depending on the method. With the original PSC, calcined SBA-15, which is known to sufficiently reduce the number of silanol groups, was used. Therefore, the quantity of APTS

attached to the wall will be significantly lower than if ethanol extraction or microwave digestion was used to remove the surfactant.

0.3 g of aminosilylated SBA-15 was added to a 30 ml aqueous solution, acidified to a pH of 1.5 (by HCl) containing 3.0 g of potassium dichromate. The solution was then stirred for 12-72 h, before filtering off the powder. The powder was then washed three times with distilled water and the powder was air dried for 0.5 h.

The potassium dichromate of the aqueous solution is acidified with HCl to become dichromic acid and potassium chloride. The potassium chloride will remain in solution avoiding a potassium contamination in the final product. The dichromate ion will attach itself to the amine group of the aminopropyl group that is attached to the wall. Since the silanol groups of calcined material is relatively low and therefore the abundance of the aminopropyl groups would also be diffuse, it would be reasonable to assume that there is some attraction between the chromate ions to each other to allow for a significant amount of the metal ions to enter the pores.

When the powder is filtered off and washed, the filtrate has to be converted from chromium (VI) to chromium (III), before being safely disposed. Other methods avoid this step by using the 'safe' chromium (III) ion as the chromium source in the form of the nitrate.

### *Dual Solvent method<sup>2</sup>*

The dual solvent method is a two-step process, the first step is to make the two solvent solutions and the second step is to combine them. Typically 1.0 g of KIT-6 was stirred for 3 h in a dry hexane solvent. 1.0 ml of an aqueous solution of the chromium nitrate was added to this solution under vigorous stirring. The solution was allowed to stir overnight before filtering the sample and drying at 40 °C.

Obviously a major advantage in this method is that the anchoring groups are the unmodified silanol groups for the attachment of the chromium ions. This takes out the time consuming step of

aminopropyl attachment as it is deemed unnecessary, as the metal ion is just as attracted to the negatively charged oxygen ions as they are to the amines. The other advantage is that the chromium (III) ion does not need to be reduced, as with the chromium (VI) before disposal, the reduction of a further step and the use of a safer chemical.

However, with the filtration, there is still the filtrate for disposal. Since the filter paper will only catch larger particles, there will be a further loss to the overall amount of material collected at the end. The filtration step can be avoided and therefore no waste solvent disposal is required.

#### *Chromium nitrate in ethanol method<sup>3</sup>*

This method is not only a one-step process but has no waste solvent or wasteful filtration step. 0.58 g of chromium nitrate nonahydrate was dissolved by stirring in 8 g of ethanol. Once dissolved, 0.15 g of the SBA-15, or other mesoporous silica, was added to the solution and stirred for a further 2 h. The solution was then transferred into a wide bottomed petri dish and the ethanol was allowed to evaporate at 40 °C.

This appears to work in the same way as the previous method, with the anchoring of the chromium ions into the pores by the hydroxyl groups. However, unlike the previous methods, the solvent is evaporated off and therefore all the material used will remain in the sample. Since we know that there is a reduction in the silanol groups with the material being calcined<sup>4</sup>, it is believed that as the solvent evaporates, the chromium ions are drawn into the pores by capillary action. Additionally, the decomposition of the chromium nitrate does go through a liquid phase before decompositions and so further capillary movement within the pores can occur at the heating stage.

Recent work carried out by another member of this research group currently suggests that simply by grinding the precursor with the mesoporous material before heating can result also in the porous material. However, the yields of the PSC products are normally low. The method was

adapted from work by Wang *et al.* who used the grinding method to impregnate the mesoporous material with metal oxides.<sup>5</sup> This implies that the more important capillary condensation step occurs during the heating phase rather than the solvent evaporation. The ethanol evaporation technique may actually be simply a good way to evenly disperse the chromium nitrate with the mesoporous silica.

### *Crystallisation of PSC*

The chromium oxide precursor containing mesoporous silica, from the previous steps, was placed in a crucible before being put into a muffle furnace. The temperature was increased at a rate of 2 °C per minute to the desired temperature of 550 °C. After dwelling for 5 h, the oven was then ramped down to room temperature and the crucible was allowed to cool before removing from the furnace.

Although the methods used different precursors, the heating conditions were exactly the same. The crystallinity of the final chromium oxide was also unchanged, which was shown by the XRD, as was the final chromium oxide from the bulk materials without the presence of silica. A detailed temperature and dwell time XRD study is revealed later of chromium nitrate with and without the porous template. The temperature study only has differing final temperatures when compared to the above procedure, whereas the time study also differs in that the samples are quenched rather than cooled gradually in the furnace.

The removal of the silica template was done by stirring for 8 h overnight with 10 % aqueous HF solution. The solution was then neutralised by a sodium hydroxide solution before separating the metal oxide powder from the solution by centrifuge. After the decantation of the liquid, the powder was washed and centrifuged thrice. The chromium oxide was then extracted from the centrifuge tube using ethanol, which was evaporated off at 40 °C. Although sodium hydroxide can also be used to remove the template, it requires stirring at 70-90 °C. Using HF, in the removal

process, only needs to be stirred at room temperature. Once the template is removed, the crystalline property of the porous metal oxide can be characterised.

## 3.2 Chromium oxide in SBA-15

### *HRTEM characterisation*

After the template is removed, the mesoporous structure of the metal oxide can be seen. As mentioned before, with the fact that the material is a negative replica of the template, the 3D network is made up of cylindrical nanorods in a hexagonal array held together by interconnecting nanobridges. The large nanorods and the smaller nanobridges are the negative replicas of the mesoporous SBA-15 main pores and complementary bridging pores, respectively (Figure 3-1).

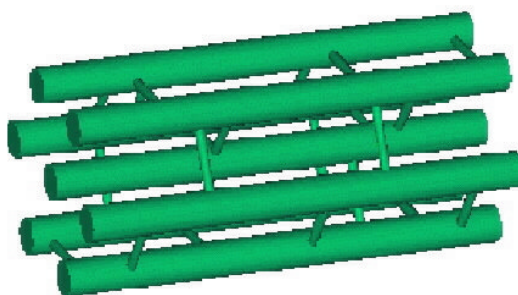


Figure 3-1. Diagram of the 3D-network of nanorods connected by nanobridges.

The nanorods in the array can be observed using the HRTEM, which can be seen in Figure 3-2. In Figure 3-2 (a), the nanorods are the dark contrast areas (indicated by the blue arrows) whereas the pores are the lighter contrast (indicated by the red arrows). It can clearly be seen that the nanorods are not just aligned with each other, but that they are part of the same framework. Figure 3-2 (b) shows a space between the two nanorods, there are two likely possibilities for this. The first is that when the material was undergoing decomposition and crystallising into the oxide, causing the contraction of the amorphous material, the material was contracting away from the

middle of the pore as the crystal was growing at either ends of the pore. The second is quite simple the nanorods were not formed in the same main pore with one being high and the other being lower. Figure 3-2 (b) also shows the first sign that the material is single crystal over the range of the nanorods. It also supports the second possibility for the separation of the nanorods as the lattice imaging can not be seen on the right hand nanorod whereas it can with the left hand nanorod.

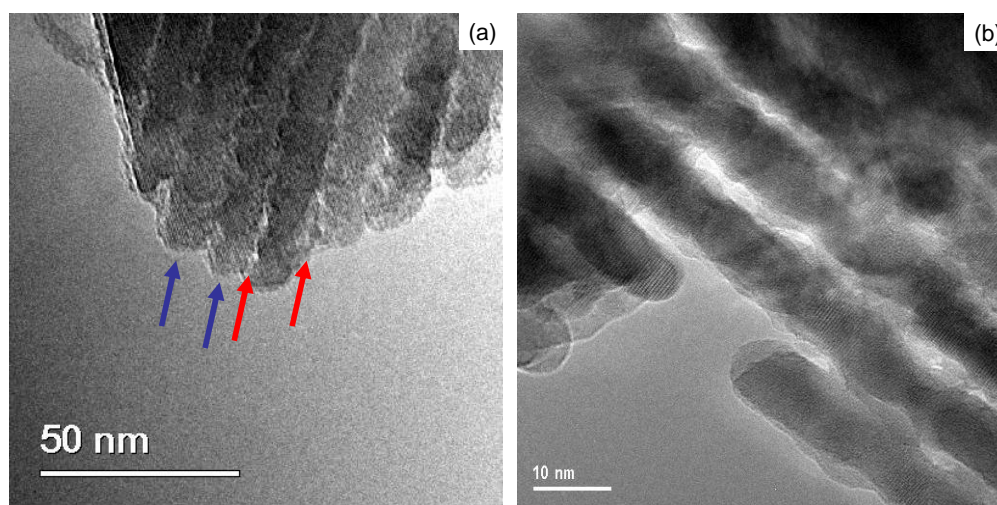


Figure 3-2. HRTEM images of low magnification images of nanorods in a PSC of  $\text{Cr}_2\text{O}_3$ . In (a), the nanorods are indicated by the blue arrows and the pores are indicated by the red arrows. Image (b) shows the nanorod arrangement with a gap.

Another thing that can be observed by the image is the reduction in particle size. Where the SBA-15 particles can be  $\sim$ microns in size, the chromium oxide mesostructure is only on the scale of nanometers in size. This is caused by the fact that when the precursor material fills the pores; it is in a low density amorphous state. This means that even if the amorphous material completely fills the pores, when the precursor decomposes to the chromium oxide, the crystals will contract due to the higher density. If it is assumed that the amorphous material has a similar density of amorphous mesoporous silica of  $2.2 \text{ g cm}^{-3}$  and the density of the crystalline chromium oxide is

5.21 g cm<sup>-3</sup> then if the amorphous precursor takes up 100% of the space then the crystalline chromium oxide would only take up 40% of the space.

The crystallinity of the mesoporous chromium oxide can first of all be investigated by the diffraction pattern. Using the selected area aperture, a large section of nanorods can be selected and they reveal a single crystalline diffraction pattern (Figure 3-3). This two dimensional pattern reveals a large scale atomic ordering in the mesoporous chromium oxide. It can also be used to confirm that the material is chromium oxide in the composition of Cr<sub>2</sub>O<sub>3</sub>, Eskolaite, as the pattern can be indexed to the rhombohedral unit cell with space group  $R\bar{3}c$  and lattice parameters  $a = 4.951$  and  $c = 13.598$  Å (JCPDS: 841616).<sup>6</sup>

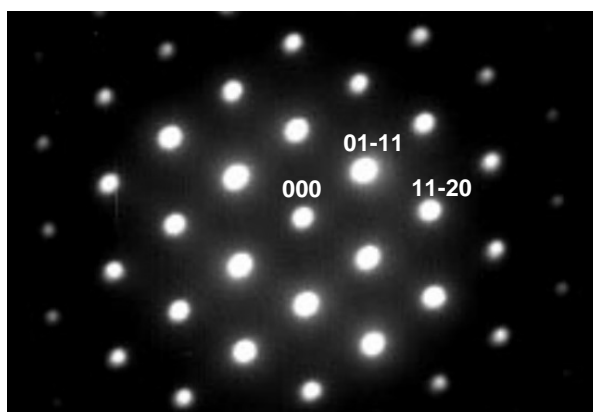


Figure 3-3. A two dimensional SAED pattern revealing the single crystal nature of the porous chromium oxide. The diffraction pattern is viewed down the  $[1\bar{1}01]$  zone axis and is indexed to the rhombohedral unit cell of Cr<sub>2</sub>O<sub>3</sub> with space group  $R\bar{3}c$  and lattice parameters  $a = 4.951$  and  $c = 13.598$  Å. The angle between the 2 indexed spots is 34°.

Once the electron diffraction pattern is obtained along a principal zone axis, the atomic ordering can be seen on the corresponding HRTEM images by increasing the magnification. In Figure 3-4, the atomic ordering for the nanorods can clearly be seen to be in the same orientation. The black arrow also indicates the nanobridge between the nanorods, which is the reason for the

hexagonal mesoporous structure being maintained after the template removal. If it was not for these bridges, then the structure would just be nanorods, which was seen in the CMK-3 paper and Figure 1-7 when comparing SBA-15 which has the bridging pores and MCM-41 which does not.<sup>7</sup>

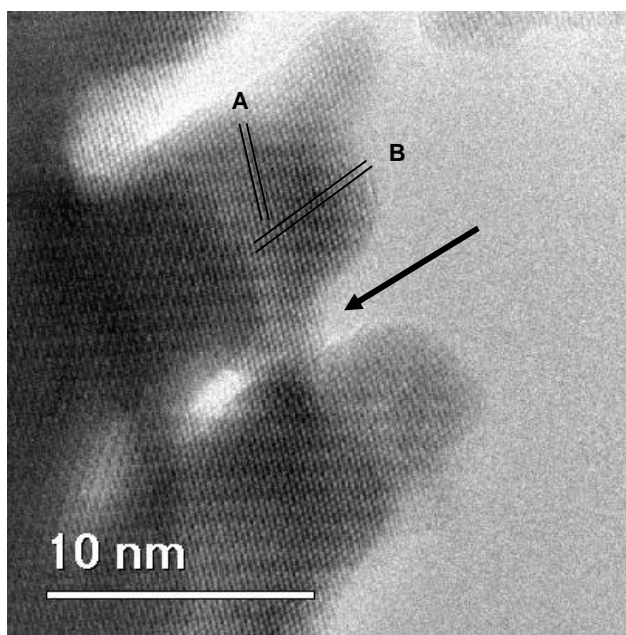


Figure 3-4. HRTEM high magnification image of two nanorods connected by a nanobridge, indicated by the black arrow. The same crystal orientation can be seen on both nanorods and across the bridge. The d-spacings  $A = 2.50 \text{ \AA}$  and  $B = 2.166 \text{ \AA}$  which corresponds to the  $(\bar{1}2\bar{1}3)$  and  $(11\bar{2}0)$  atomic planes, respectively, of the rhombohedral  $\text{Cr}_2\text{O}_3$  ( $a = 4.951$  and  $c = 13.598 \text{ \AA}$ ), viewing down the  $[1\bar{1}01]$  zone axis.

The fact that the crystalline bridge can be seen after the template removal further supports the reasoning that the chromium oxide is following the pore structure rather than the nanorods self-arranging into the hexagonal array. If the nanorods were arranging hexagonally after the mesoporous silica was removed then the material would not exhibit a pore structure and would more closely resemble a bundling effect of the nanorods.

Also, if the pore filling is low or there are less bridging pores between the major pores, then single nanorods can be seen. If the bridging is low and the nanorods are more isolated in the

growth of the crystals, then disordered nanorods can be seen (Figure 3-5). This can be due to the nanobridging pores collapsing, which is discussed in greater detail later in this chapter.

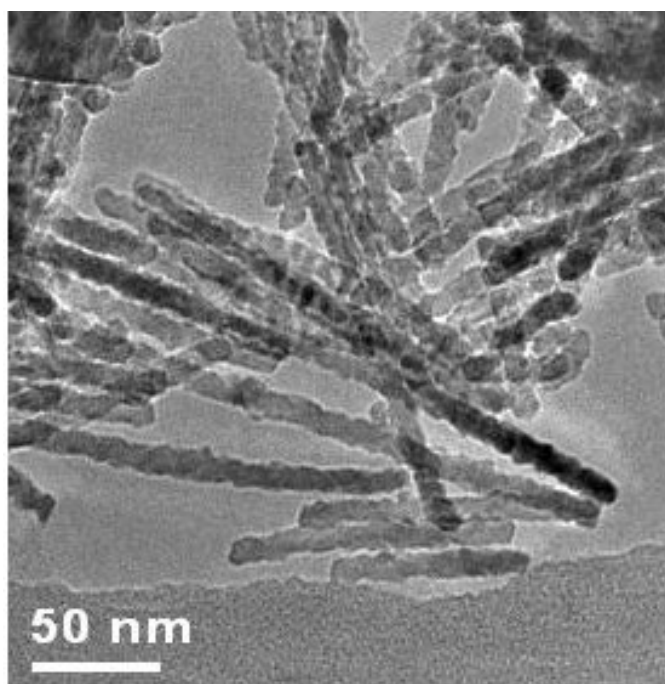


Figure 3-5. HRTEM image of nanorods of Cr<sub>2</sub>O<sub>3</sub> with little or no connectivity by nanobridges.

#### *XRD study of crystallisation*

Using a temperature dependent study of the oxide formation in SBA-15, the decomposition of the nitrate can be seen (Figure 3-6). Cr (III) ions, which is the oxidation state of the chromium when as chromium nitrate (Cr(NO<sub>3</sub>)<sub>3</sub>·9H<sub>2</sub>O) and chromium oxide (Cr<sub>2</sub>O<sub>3</sub>), have a green colour. The colour is lighter and easier to distinguish when inside the mesopores of the silica, which has no colour. When the sample is heated to ~100 °C, the sample changes from green to brown. The brown colour is typical of chromium (IV) ions, indicating that when the nitrate decomposes, giving out NO<sub>x</sub> gases, the chromium (III) is oxidised to chromium (IV), as well as other chromium ions described later.

The chromium stays brown until 350 °C where it turns to a greenish-brown colour, and at 400 °C the sample is green. At 350 °C, the chromium (IV) has been partially reduced back to chromium (III) but not fully since there is still presence of the brown colour. After 400 °C, the chromium (IV) has fully been reduced to chromium (III) losing the brown colour all together.

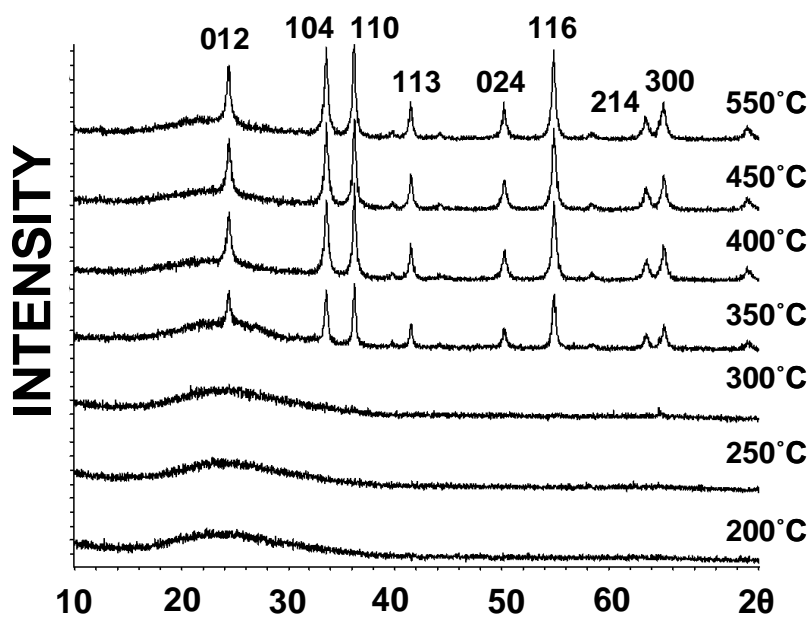


Figure 3-6. XRD patterns of temperature study for crystal growth of  $\text{Cr}_2\text{O}_3$  in SBA-15 from 200-550 °C. Dwell time at each temperature was for 5 h. XRD peaks are indexed to the rhombohedral unit cell ( $a=4.951$  and  $c=13.598$  Å).

By looking at the XRD, it can be seen that before 350 °C, the chromium-containing material inside the SBA-15, is in an amorphous state (Figure 3-6). It is only after the chromium (IV) starts to be reduced into chromium (III) oxide that a crystalline pattern starts to be seen (350 °C). After 350 °C, once the chromium (IV) is fully reduced to chromium (III), the crystal diffraction pattern does not intensify. The only crystalline phase can clearly be seen to be chromium (III) oxide with the rhombohedral unit cell with parameters  $a = 4.951$  and  $c = 13.598$  Å.

Comparing this to the XRD data collected for the first PSC paper,<sup>1</sup> it can be seen that even though dichromate is used as the chromium source, the XRD patterns are the same. This is

further supported by R. B. King in his book, *Encyclopaedia of Inorganic Chemistry*, which states that chromium (VI) oxide will go through the intermediate phase of chromium (IV) oxide before reducing to chromium (III) oxide.<sup>8</sup>

As can be seen by the XRD, there is no crystallisation before 350 °C. A time dependent study at this temperature was carried out in 0.5 h steps at this temperature from 0.5-2 h. Although there was no significant colour change from that of the brown sample at 300 °C for 5 h and 350 °C at 2 h, XRD shows that crystallisation of chromium (III) oxide had occurred.

Figure 3-7 shows that after 1.5 h that the chromium (III) oxide signal in the XRD had grown significantly. In fact using the peak positions from the above material and extrapolating it down to the 0.5 and 1 h XRD patterns, very small peaks can be seen. What can clearly be seen in these data is that there are no crystalline intermediate phases before the growth of the final chromium (III) oxide. Comparing this to the decomposition of chromium nitrate without the presence of silica, the effect of the material being inside the pores can be observed.

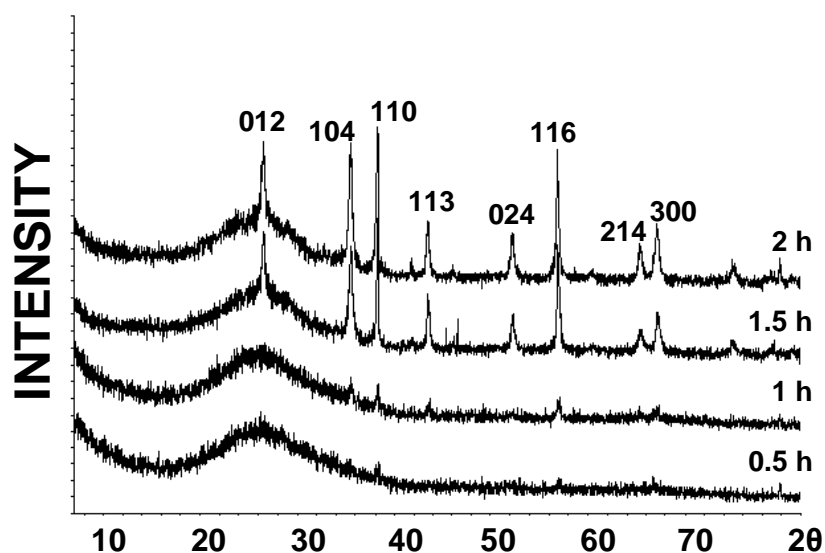


Figure 3-7. XRD patterns of the crystal growth of Cr<sub>2</sub>O<sub>3</sub> inside SBA-15 from a time dependent study at 350 °C for 0.5-2 h. The patterns clearly show that the material remains amorphous until the final crystalline product. Peaks are indexed to the rhombohedral unit cell.

The chromium nitrate, without the presence of silica, was heated at 350 °C for 0.5-2 h in 0.5 h increments and 3-5 h in 1 h increments (Figure 3-8). XRD patterns revealed that the chromium nitrate stays in a decomposed amorphous state until 350 °C after 1 h. The broad hump in the  $2\theta$  range of 20-35°, is indicative of the amorphous intermediate chromium oxide. It is not until the 2 h stage that this hump disappears indicating that all the amorphous material has been converted to a crystalline state. The peaks can be indexed to  $\text{Cr}_2\text{O}_5$  with the monoclinic unit cell parameters of  $a = 12.01$ ,  $b = 8.52$ ,  $c = 9.39$  Å and  $\beta = 92.0^\circ$  (JCPDS 381329).<sup>9</sup> Peaks for  $\text{Cr}_2\text{O}_5$  even after 5 h of heating at 350 °C are still unchanged, indicating that this is the metastable intermediate product for the nitrate decomposing to the chromium (III) oxide. It is not until 400 °C at 5 h that all the material becomes chromium (III) oxide.

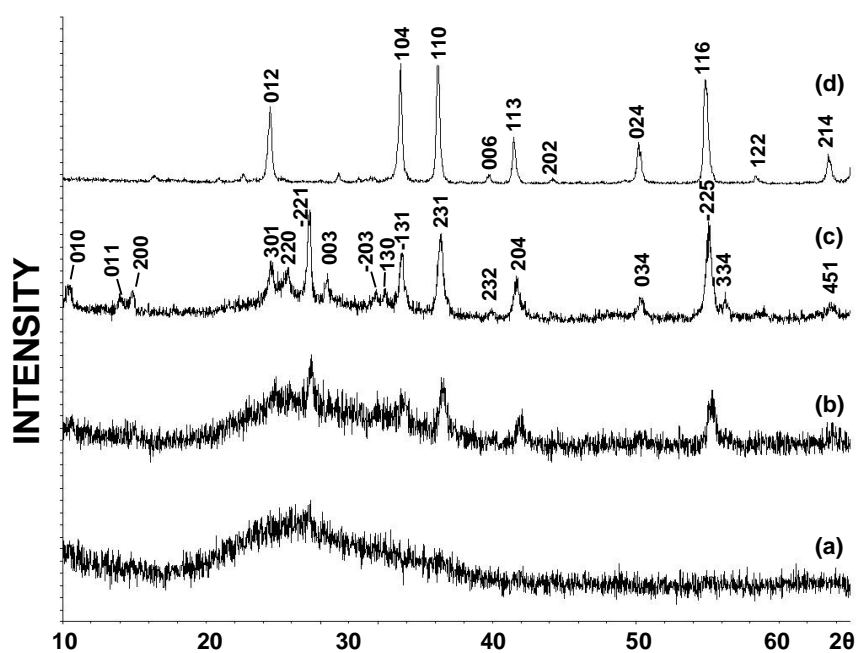


Figure 3-8. XRD patterns of the decomposition of chromium nitrate without the presence of mesoporous silica template. (a-c) Patterns after 350 °C treatment for 0.5-1.5 h in 0.5 h increments. Pattern (c) is indexed to  $\text{Cr}_2\text{O}_5$  with a monoclinic unit cell with parameters  $a=12.01$ ,  $b=8.52$ ,  $c = 9.39$  Å and  $\beta= 92.0^\circ$ . (d) XRD pattern from the specimen after heating the chromium nitrate to 400 °C for 5 h, showing the rhombohedral phase of  $\text{Cr}_2\text{O}_3$ .

When comparing this to the material in the mesopores, it can be seen that a slightly different crystallisation route is occurring. The chromium nitrate, as suggested by Labus *et al*, decomposes to become amorphous  $\text{Cr}_5\text{O}_{12}$ .<sup>10</sup> This material then crystallises into a mixture of chromium (V) oxide  $\text{Cr}_2\text{O}_5$  and chromium (IV) oxide  $\text{CrO}_2$  at 350 °C. The chromium (V) oxide and the chromium (IV) oxide reduce, evolving oxygen, to become chromium (III) oxide at 400 °C. This difference in the crystallisation route between materials with and without the presence of mesopores can also be seen in the chapter on cobalt oxide.

Labus *et al* suggests that the chromium (III) oxide formation is a competitive process with an endothermic and exothermic process.<sup>10</sup> The endothermic process is the reconstruction of the crystalline phase whereas the exothermic process is the recombination of the evolved atomic oxygen. They also found that the endothermic process is preferred over the exothermic process with reduction of the mass of the material.

Obviously, inside the mesopores, there is less material available so, according to Labus *et al*, the endothermic recrystallisation process would be preferred over the exothermic recombination of oxygen process. However, as it was seen that no recrystallisation occurred in any intermediate products before the formation of the chromium (III) oxide, it can be assumed that this endothermic process is not the dominant process. Since inside the pores, heat transportation is rather difficult, the crystallisation of the intermediates will not obtain the energy this process requires, and therefore not occur. With no endothermic process occurring, then the majority of the energy from the furnace, as well as that given out by the evolution of oxygen, will go into the formation of the chromium (III) oxide. This may also be the reason for a lower crystallisation temperature that is needed to crystallise the chromium (III) oxide.

The crystallisation temperature is not the only effect from the mesopores, but it was found that without the presence of the mesopores, there is no control over the shape and size of the crystals. Particles of chromium oxide formed in the SBA-15 will be cylindrical, with several

nanorods of approximately the same length attached to each other. Similarly, since the amount of material that is able to migrate to the crystal is restricted by the pores, the range of crystal size is rather small (70-150 nm in diameter). However, when the material is more abundant and there are no size constraints, the shapes of the crystals are irregular (Figure 3-9) and a wide range of sizes can be seen (150 nm to several microns).

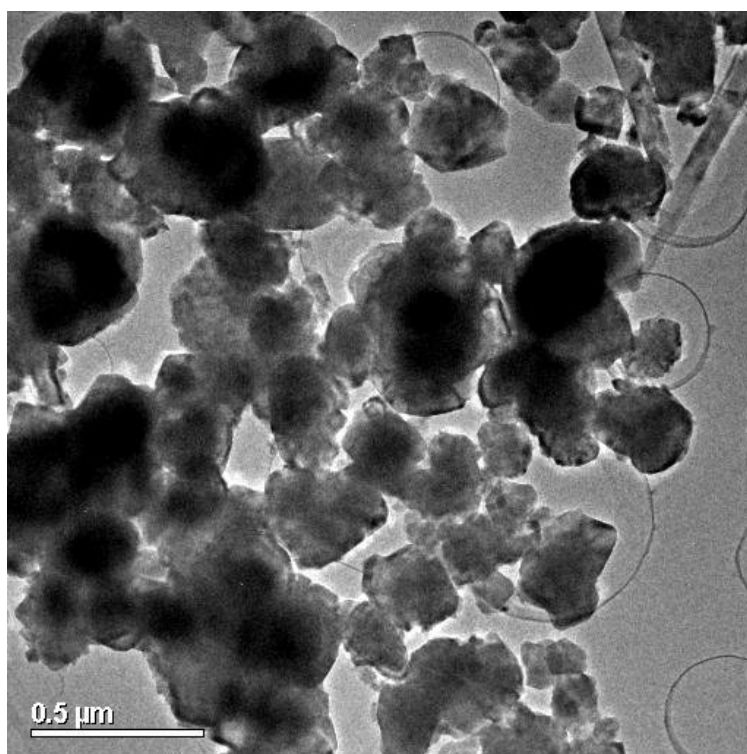


Figure 3-9. HRTEM image of bulk chromium oxide particles formed without the presence of mesopores showing irregular shape and size of particles.

The HRTEM was used to try and view the chromium oxide nanoparticles, inside the SBA-15, after 0.5-1 h of heating at 350 °C. Unfortunately, the nanoparticles were not seen within the pores. This is due to the particles being so small and having a wide dispersity. The wide dispersion of the nanoparticles was more of a problem in obtaining images as very small particles in mesoporous silica can be seen using the HRTEM when dispersity is low and clusters are

common.<sup>11</sup> It does become harder to see the particles that are well dispersed, especially for particles that are only about 2 nm in amorphous material that is 200 nm thick. The nanocrystals are so small, that the SAED does not show up any diffraction spots.

After 2 h at 350 °C, when the XRD peaks have significantly increased, SAED patterns of the particles are visible, see Figure 3-10. The patterns do however reveal a multicrystal property, indicating that several crystals of chromium oxide form in each particle of SBA-15. In fact, even after 5 h at 550 °C, the multicrystal SAED pattern is still seen. Once the SBA-15 is removed, the SAED reveals that each crystal is a single crystal, indicating that the multiple crystals in the

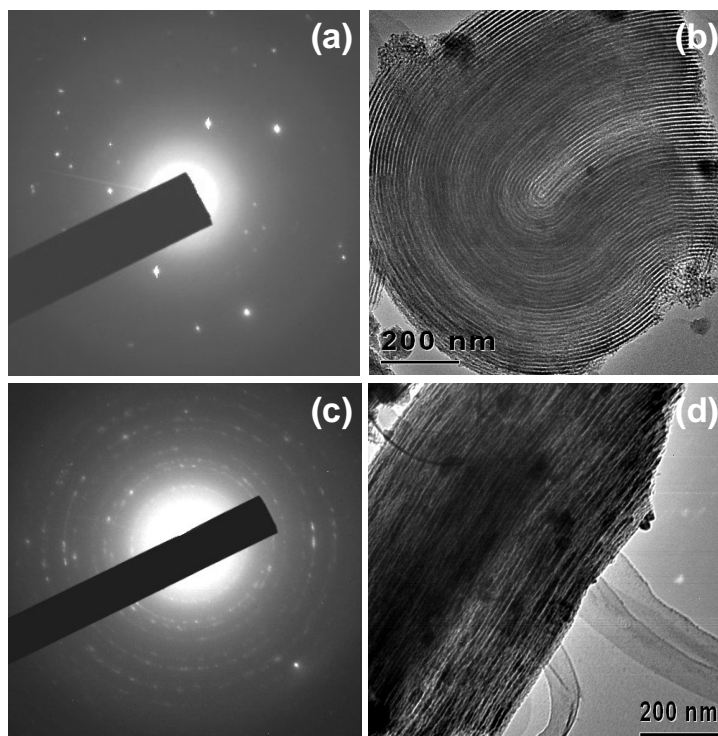


Figure 3-10. HRTEM images and SAED patterns of chromium oxide in SBA-15 with (a-b) coming from after heat treatment at 350 °C for 2 h and (c-d) from heat treatment at 400 °C for 5 h.

SBA-15 are single crystal in their own right but different orientations in the mesopore system. However, some relation could be seen in chromium oxide PSC made in KIT-6 using the dual solvent method.

### 3.3 Chromium oxide in KIT-6

#### *HRTEM of PSC*

Although KIT-6 has a cubic structure, there is a greater relation to SBA-15 (hexagonal) than the cage structures of FDU-12 and SBA-16 (both are cubic). This is due to the KIT-6 channels being continuous pore systems with branching. The two pore systems in KIT-6 appear to be separate and this is supported by the data of  $\text{Cr}_2\text{O}_3$  PSCs. However, in Chapter 4, it will be discussed about how there is evidence that they are connected with each other.

After the chromium (III) oxide had been crystallised in the template of KIT-6 at 550 °C for 5 h, an SAED was taken and a multicrystal pattern was obtained, as before from SBA-15. HRTEM images of the template with the chromium oxide crystals revealed several particles inside (Figure 3-11). Once again the size of particle range is smaller, 100-200 nm, than the

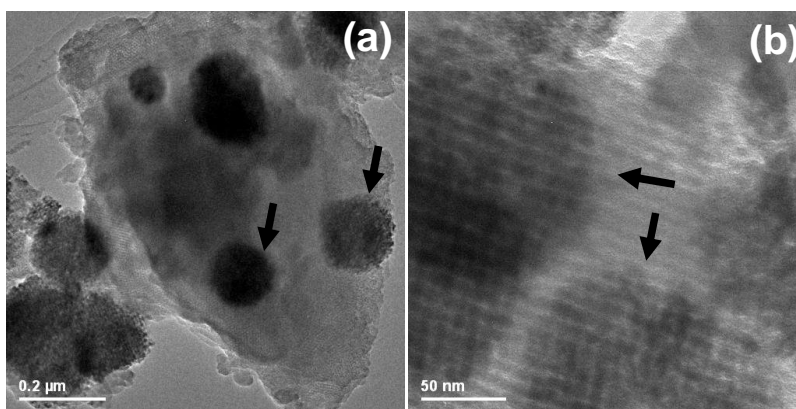


Figure 3-11. HRTEM images of spherical chromium oxide particles in KIT-6. The black arrows indicate the separate crystals. (a) A low magnification image of several particles inside the KIT-6 template. (b) A TEM image at a higher magnification looking at particles growing in close proximity to each other but are not connected.

template, with it being ~microns in size. After the template is removed, all the particles were found to be spherical in shape and revealed the first of the interesting things.

When the template was removed, it could be seen that the crystal had grown in only one of the channels, see Figure 3-12 (inset). This allowed for the pores to be clearly seen as some empty

channels on the view direction and supported the fact that the bicontinuous pores were unconnected. When both pore networks are replicated in the case of PSC of  $\text{Co}_3\text{O}_4$  (Chapter 4), no such empty channels can be seen. The chromium oxide particles tended to collect together into clusters (Figure 3-12). This is thought to be some sort of small particle effect. The adsorption properties of this will be discussed later. SAED of the crystal showed the single crystal property which could then be seen with the atomic ordering. When the dual solvent method was used, an interesting feature was seen which was absent using the ethanol method.

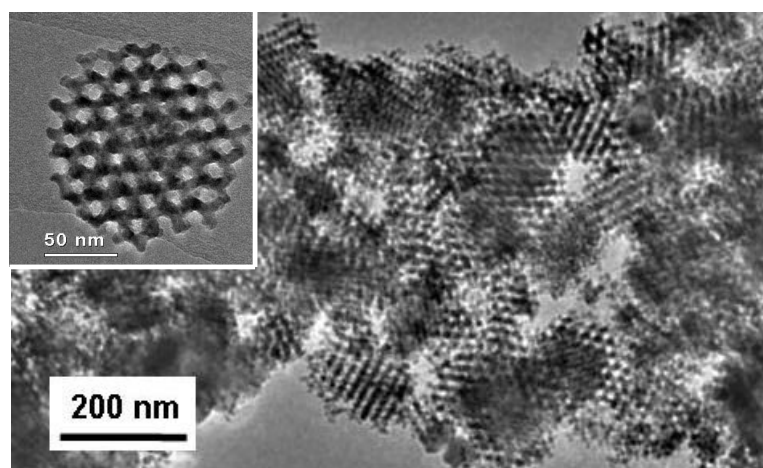


Figure 3-12. HRTEM of chromium oxide templated by KIT-6. Main image is clusters of the porous single crystals in various orientations. Inset is a porous single crystal on its own viewed down the  $[111]$  axis of the mesopore network.

When several PSCs, that were formed using the dual solvent method, were analysed, it was found that there was some connection between the mesopore orientation and the crystal orientation. Looking at two particles down the  $[100]$  and  $[111]$  direction, it was found that the crystal orientation was  $[\bar{2}\bar{2}01]$  and  $[0001]$  respectively (Figure 3-13). Although this may not seem related, the angle between the mesopore directions is  $54.7^\circ$ , whilst the angle between the crystal orientations is  $51.5^\circ$  (3.1 and 3.2). The difference of the angles can be attributed to the difference between a cubic unit cell and a rhombohedral unit cell.

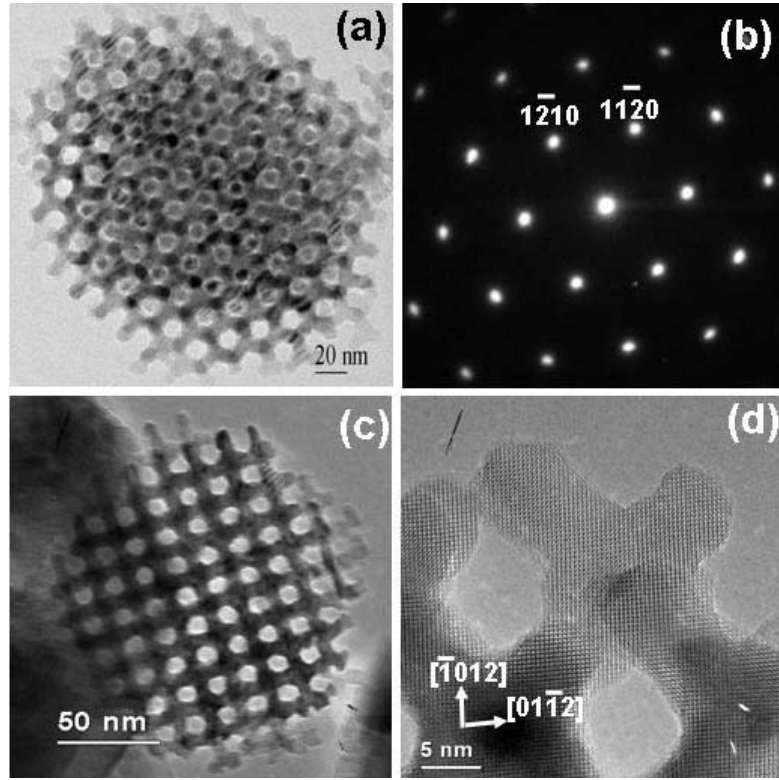


Figure 3-13. (a) TEM image of a PSC particle of  $\text{Cr}_2\text{O}_3$  templated by KIT-6 viewed down the mesoporous orientation  $[111]$  with (b) being the corresponding SAED of the single crystal viewed down the  $[0001]$  direction. (c) Another TEM image from the same specimen along the  $[100]$  mesoporous zone axis and (d) the corresponding HRTEM image showing the single crystal of  $\text{Cr}_2\text{O}_3$  viewed down the  $[\bar{2}\bar{2}01]$  zone axis.

The interaxis angle between  $[111]$  and  $[100]$  of the cubic mesostructure is

$$\rho = \cos^{-1} \left( \frac{u_1 u_2 + v_1 v_2 + w_1 w_2}{\sqrt{(u_1^2 + v_1^2 + w_1^2)(u_2^2 + v_2^2 + w_2^2)}} \right) = \cos^{-1} \left( \frac{1}{\sqrt{3}} \right) = 54.7^\circ \quad (3.1)$$

while the angle between  $[0001]$  and  $[\bar{2}\bar{2}01]$  of the  $\text{Cr}_2\text{O}_3$  crystal is

$$\rho = \cos^{-1} \left( \frac{u_1 u_2 + v_1 v_2 - \frac{1}{2}(u_1 v_2 + v_1 u_2) + \frac{c^2}{a^2} w_1 w_2}{\sqrt{\left[ \left( u_1^2 + v_1^2 - u_1 v_1 + \frac{c^2}{a^2} w_1^2 \right) \left( u_2^2 + v_2^2 - u_2 v_2 + \frac{c^2}{a^2} w_2^2 \right) \right]}} \right) = 51.6^\circ \quad (3.2)$$

As mentioned before this phenomenon was not seen with material made from the ethanol evaporation method, although, both methods did result in the mesopores causing the same size and shape constraints.

#### *Isotherm data of PSC*

The porosity of the PSCs could also be checked using nitrogen adsorption. Isotherm data of the nitrogen adsorption of the chromium oxide templated by the KIT-6 confirmed the mesoporosity. It also revealed a decrease of surface area when compared to the KIT-6 surface area. The lower surface area can be attributed to the loss of microporosity in the negative replica, which was revealed by the t-plot. This makes sense, as the microporosity in the mesoporous silica is due to the surfactant bridging the pore systems. Additionally, since the structure of the PSC is effectively just the negative replica of the pore system, the external surface area will be reduced, when compared to the template external surface, as well. With the specific surface area being  $74 \text{ m}^2/\text{g}$  and a pore volume of  $0.456 \text{ cm}^3 \text{ g}^{-1}$ , the surface area per volume can be calculated using the density of the crystal.

The surface area per volume was calculated as  $114 \text{ m}^2 \text{ cm}^{-3}$  (3.3) when assuming that the density of the chromium oxide was  $5.21 \text{ g cm}^{-3}$ , which is that of the bulk chromium oxide. This is about a quarter of the KIT-6 surface area per volume calculated as  $462.9 \text{ m}^2 \text{ cm}^{-3}$ , with the specific surface area of  $752 \text{ m}^2/\text{g}$  and pore volume of  $1.17 \text{ cm}^3/\text{g}$  and density of silica  $2.2 \text{ g cm}^{-3}$  (3.4). The reasonable high surface area also indicates that the yield of the PSC product is high, in agreement with the TEM observation.

For the PSC product of  $\text{Cr}_2\text{O}_3$ , the surface area per volume is

$$\frac{1\text{g}}{\left(0.456 + \frac{1}{5.21}\right)\text{cm}^3} \times 74\text{m}^2 / \text{g} = 114.2\text{m}^2 / \text{cm}^3 \quad (3.3)$$

In comparison, the value for KIT-6 is

$$\frac{1g}{\left(1.17 + \frac{1}{2.2}\right)cm^3} \times 752m^2 / g = 462.9m^2 / cm^3 \quad (3.4)$$

The isotherm also reveals that the rapid uptake of nitrogen occurs at relatively high pressures ( $P/P_0 = 0.88$ ), see Figure 3-14. This is probably due to the fact that only one pore system has been used in the creation of each PSC and this makes a relatively larger pore. As mentioned before, the particles of the chromium oxide are also attracted to each other, possibly to magnetic interactions, and this would result in the larger pore width, Figure 3-15 (a), and the nitrogen adsorption occurring at a higher pressure. This can also be seen in AMS-8 particles that have aggregated together.<sup>12</sup>

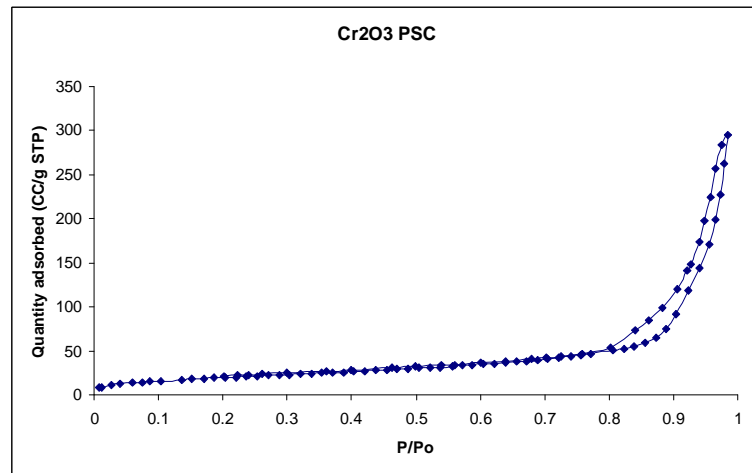


Figure 3-14. Nitrogen adsorption isotherm of mesoporous chromium oxide templated by KIT-6.

With the nitrogen adsorption data being relatively linear before  $P/P_0 = 0.8$ , the pore size distribution graph is very broad between 0 and 130 Å, seen in Figure 3-15 (b). However, there are two slight inflections (indicated by the black arrows) to the graph which could give an indication of pore size. The first peak is at about 4 nm and the second is at about 9 nm. These values for the pore size will be corroborated with the PSD for mesoporous cobalt oxide (Chapter 4).

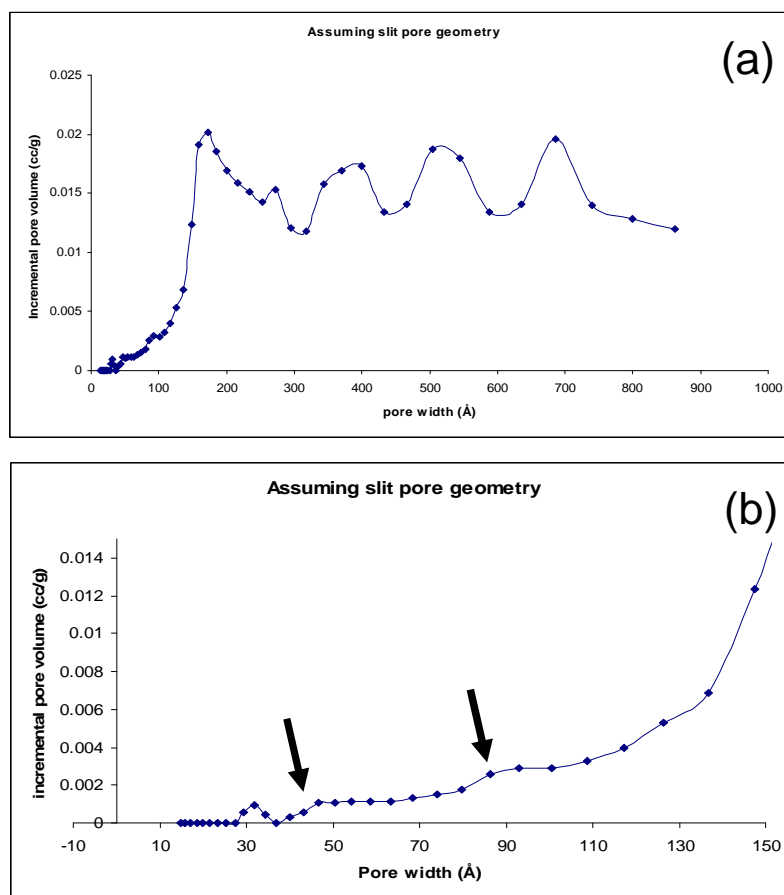


Figure 3-15. Graphs of pore size distribution for Cr<sub>2</sub>O<sub>3</sub> templated my KIT-6. (a) The full range of pore width and (b) the PSD below 150 Å with the black arrows indicating the points of inflection.

### *Magnetic behaviour of PSC*

The magnetic behaviour of the PSC material was investigated in a magnetometer by Professor Andrew Harrison (University of Edinburgh). Chromium oxide is a well known paramagnetic material. When the chromium oxide is in the fully dense form as bulk material, the material will antialign antiferromagnetically with and without a field. The reduction of the temperature reveals that both with an applied magnetic field and without, there is a similar curve; this can be seen in Figure 3-16 (a). The applied field was 100 Oe.

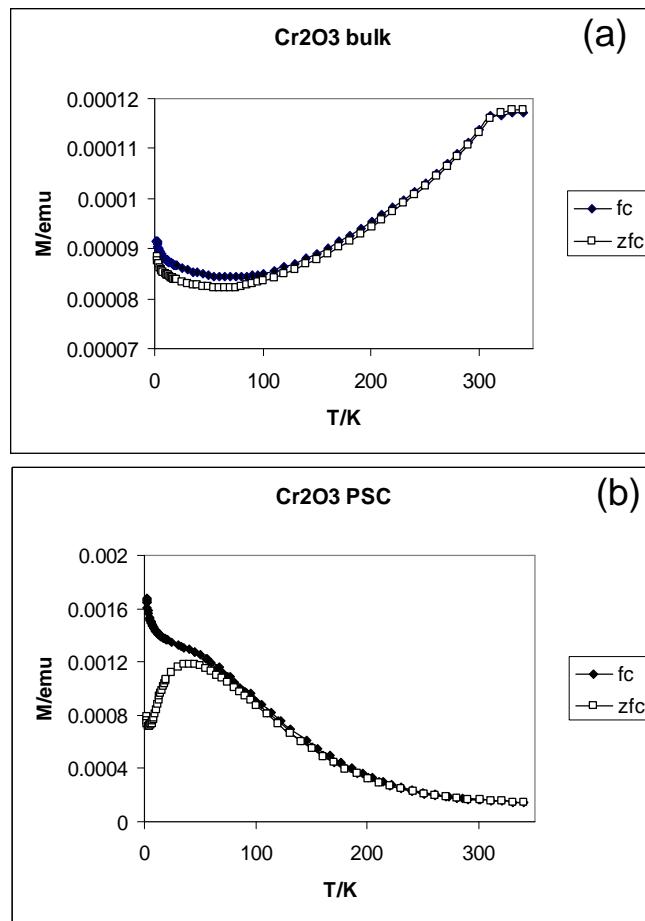


Figure 3-16. Magnetic behaviour in the presence of a magnetic field (fc) and without a magnetic field (zfc) for (a) bulk  $\text{Cr}_2\text{O}_3$  and (b) mesoporous  $\text{Cr}_2\text{O}_3$ .

As seen in Figure 3-16 (b), the different magnetic behaviour can clearly be seen, even when no external field is applied. Unlike the bulk material, which exhibits antiferromagnetic behaviour under 308 K, the PSC behaves like nanoparticulate material. With cooling outside of a magnet field (zfc) before increasing the heat and then cooling with a magnetic field (fc), the magnetic behaviour is similar above 100 K. It is only under 100 K that the magnetic behaviour changes between with/without applied external field. In the graph, the divergence can clearly be seen. Additionally, there is a cusp at 40 K, which can be deduced as coming from a blocking of the magnetism in the nanorod network of the PSC when comparing it to 15 nm nanoparticles of chromium oxide.<sup>13</sup> Obviously the nanorod thickness, approximately 8 nm for KIT-6 templated

material, is a lot closer to 15 nm than the overall size of the PSC, ranging from 100-200 nm. Also like the nanoparticles, the PSC exhibits a weakly ferromagnetic response at low temperature. This weak ferromagnetism has previously been reported to have resulted from an uncompensated excess of surface spins that have aligned, as particles get smaller, the importance and effect of these increase.<sup>14</sup>

#### *Catalytic behaviour of PSC*

The chromium oxide PSC has been investigated as a possible catalyst in the oxidation of cyclohexene by Professor Jim Anderson (University of Aberdeen). Depending on the level of oxidation of cyclohexene, the products can be either the epoxide or the ketone resulting from selective oxidation and non-selective oxidation respectively. The oxidation of the cyclohexene into the epoxide followed by hydrolysis into the diol can be seen in Figure 3-17.

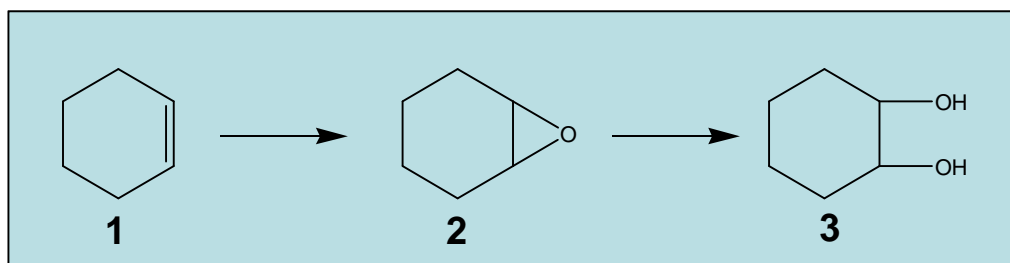


Figure 3-17. Reaction of the oxidation of cyclohexene (1) with partial oxidation leading to the epoxide, 7-oxabicycloheptane, (2) and complete oxidation leading to the diol, Cyclohexan-1,2-diol, (3).

For the catalytic tests, 0.05g of  $\text{Cr}_2\text{O}_3$  PSC was added to a stainless steel autoclave containing 0.74 mmol cyclohexene, 2.08 mmol dimethylpropanol and 25 ml of toluene as solvent. The reactor was purged with pure oxygen and pressurized to 10 bar. The contents were stirred at 85 °C for 16 h before the solution was analysed using gas chromatography-mass spectrometer.

The selective catalytic oxidation of cyclohexene to the epoxide (oxabicycloheptane) showed 98.7% conversion of the sacrificial oxidant, 2,2-dimethylpropanal (pivaldehyde) to 2,2-dimethyl propanoic acid (pivalic acid); Figure 3-18, in addition to the 100 % conversion of the cyclohexene. The sacrificial oxidant removes the excess oxygen and avoids the complete oxidation of the cyclohexene from occurring. The reaction was found to be 34 % selective to the epoxide with a minor amount of cyclohex-1-one and the remaining product being the hydrolysis product of the epoxide leading to the diol. Traces of benzaldehyde were detected indicative of oxidation of the solvent.

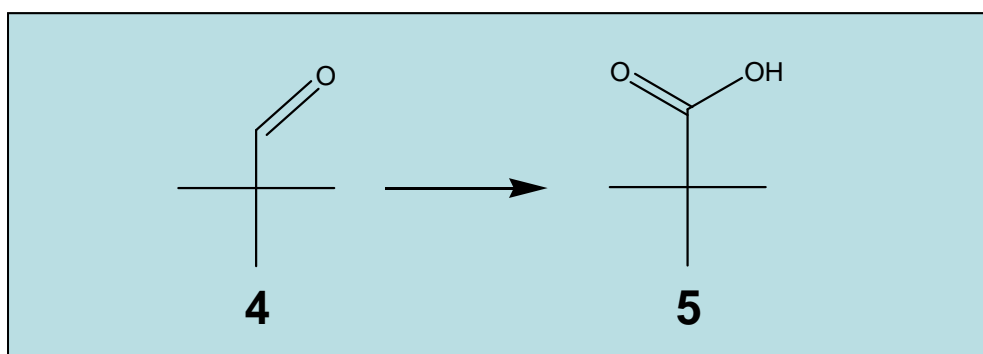


Figure 3-18. Oxidation of 2,2-dimethylpropanal (4), pivaldehyde, to 2,2-dimethyl propanoic acid (5), pivalic acid.

The PSC appears to be very powerful in this oxidation reaction. The product of pivalic acid is synthesised by the addition of oxygen into the aldehyde C-H bond. The PSC is obviously able to activate the molecular oxygen for this insertion. The minor amounts of cyclohexanone and the large amounts of the epoxide and the diol suggests that the PSC is selective in the oxidation step and allows single oxygen atom transfer from the *in situ* formed peracid. Usually this sort of reaction is largely restricted to single site metal centered complex catalysts.<sup>15</sup>

In summary, chromium oxide PSC has been successfully synthesised in mesoporous templates SBA-15 and KIT-6. The single crystallinity of the material was investigated using HRTEM and

SAED. The temperature for crystallisation within the pores from the decomposition of the chromium nitrate was reduced when compared to the bulk. The chromium oxide templated by KIT-6 synthesised by the dual solvent method showed some relation between the mesoporous orientation and crystal orientation. The isotherm for chromium oxide had two inflections at 4 and 9 nm and also revealed that the specific surface area per volume was  $\frac{1}{4}$  of that from KIT-6. The magnetism of a PSC is different to that from bulk possibly with having a weakly ferromagnetic response, possibly caused by uncompensated excess of surface spins. A catalytic test for the PSC has also shown promising results.

## References

- [1] K.K. Zhu, B. Yue, W.Z. Zhou and H.Y. He, *Chem. Commun.*, 2003, 98
- [2] K. Jiao, B. Zhang, B. Yue, Y. Ren, X.Y. Liu, S.R. Yan, C. Dickinson, W.Z. Zhou and H.Y. He, *Chem. Commun.*, 2005, 5618
- [3] B.Z. Tian, X.Y. Liu, H.F. Yang, S.H. Xie, C.Z. Yu, B. Tu and D.Y. Zhao, *Adv. Mater.*, 2003, **15**, 1370
- [4] B.Z. Tian, X.Y. Liu, C.Z. Yu, F. Gao, Q. Luo, S.H. Xie and D.Y. Zhao, *Chem. Commun.*, 2002, 1186
- [5] Y.M. Wang, Z.Y. Wu and J.H. Zhu, *J. Solid State Chem.*, 2004, **177**, 3815
- [6] P.D. Battle, T.C. Gibb, S. Nixon and W.T.A. Harrison, *J. Solid State Chem.*, 1988, **75**, 21
- [7] R. Ryoo, S.H. Joo, M. Kruk and M. Jaroniec, *Adv. Mater.*, 2001, **13**, 677
- [8] R.B. King, *Encyclopedia of Inorganic Chemistry*, 1994, **2**, 666
- [9] T.A. Hewston and B.L. Chamberland, *J. Magn. Magn. Mater.*, 1984, **43**, 89
- [10] S. Labus, A. Malecki and R. Gajerski, *J. Therm. Anal. Calorim.*, 2003, **74**, 13
- [11] W.Z. Zhou, J.M. Thomas, D.S. Shephard, B.F.G. Johnson, D. Ozkaya, T. Maschmeyer, R.G. Bell and Q. Ge, *Science*, 1998, **280**, 705
- [12] A.E. Garcia-Bennett, K. Lund and O. Terasaki, *Angew. Chem. Int. Ed.*, 2006, **45**, 2434
- [13] S.A. Makhlof, *J. Magn. Magn. Mater.*, 2004, **272**, 1530
- [14] Y.Q. Wang, C.M. Yang, W. Schmidt, B. Spliethoff, E. Bill and F. Schuth, *Adv. Mater.*, 2005, **17**, 53
- [15] S. Bhattacharjee and J. A. Anderson, *J. Molec. Catal, A*, 2006, **249**, 103.

## 4. Porous Single Crystal of Cobalt Oxide

With the success of chromium oxide forming PSCs, cobalt oxide was investigated. The nitrate method was used, rather than the aminosilylated method, to allow the crystal growth of cobalt oxide inside the mesopores of the silica template. Cobalt oxide, formed in SBA-15 and KIT-6 have been characterised and a possible formation mechanism is suggested.

### 4.1 Synthetic methods for PSCs

#### *Cobalt nitrate in ethanol method*<sup>1</sup>

0.46 g of cobalt nitrate hexahydrate was dissolved in 8 g of ethanol, whilst stirring. Once dissolved, 0.15 g of the mesoporous silica was added to the solution and stirred for a further 2 h. The solution was then transferred into a wide-bottomed petri dish and the ethanol was allowed to evaporate at room temperature until dry.

It is unclear so far whether the cobalt nitrate is entering the pores in the solvent evaporation step or the melt step (during the heating stage), that was described in the previous chapter. However, regardless of this, it can be suggested that it will be the driving force of capillary condensation that will cause the cobalt nitrate to enter the pore system of the mesoporous template.

#### *Crystallisation of PSC*<sup>2</sup>

The mesoporous silica containing the cobalt nitrate precursor was heated in a crucible inside a muffle furnace. The material was kept at 550 °C for 5 h, after increasing the temperature at a rate of 2 °C per minute. The furnace was returned to room temperature and the crucible was removed once cool.

A detailed temperature and dwell time XRD study was carried out for both cobalt nitrate with and without the porous template. The temperature study varied different final temperatures, 125-200 °C and 150-225 °C with and without silica respectively, whereas the time study varied the dwelling time in 0.5 h or 1 h increments. Additionally, in the time study, samples were quenched rather than cooled to allow for accurate time measurements to be taken.

The removal of the silica template was done in the same way as for the PSC of chromium oxide. The sample was stirred overnight with 10 % aqueous HF solution before neutralising with a sodium hydroxide solution and centrifuging. The cobalt oxide powder was washed and centrifuged, three times, before extracting with ethanol. The ethanol was then evaporated off leaving the dry metal oxide sample for characterisation.

## 4.2 Cobalt oxide in SBA-15

As with chromium oxide, mentioned in the previous chapter, the material negatively replicated the SBA-15 template. This could be seen by HRTEM imaging after the template was removed.

### *HRTEM characterisation*

Looking at the low magnification images of the cobalt oxide particles, it was found that less non-porous bulk material was found in the sample. The shape selectively caused by the mesopores, more easily seen in the spherical KIT-6 negative replicas, could also be seen for the SBA-15 negative replica. However, instead of the material being spherical in shape, the crystals tended to be cylindrical. Figure 4-1 is a TEM image of a cobalt oxide particle. As before, the size of these particles was much smaller than that of the silica template, which can be attributed to the density of the cobalt material increasing as the cobalt nitrate decomposed to the oxide. Although,

when chromium oxide formed a PSC, there was a number of non-porous crystals, the cobalt oxide sample was almost all mesoporous material (>90 %) with very few bulk particles.

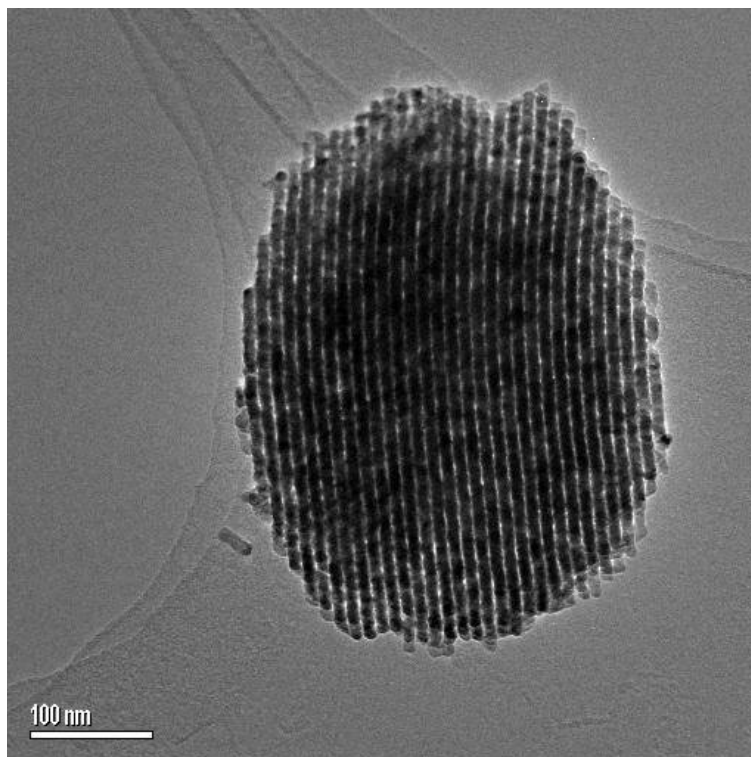


Figure 4-1. Low magnification TEM image of the cobalt oxide negative replica of SBA-15.

By tilting the sample, the nanobridges can be observed connecting the nanorods, seen in Figure 4-2 (a). This resulted from the bridging pores of the template and is believed to be essential for the communication during the crystallisation for a single crystal. The bridging allows for the hexagonal array to be maintained after the template is removed. Figure 4-2 (b) shows the hexagonal array of the nanorods of cobalt oxide after the removal of the template, viewing down the [0001] direction of the mesoporous phase.

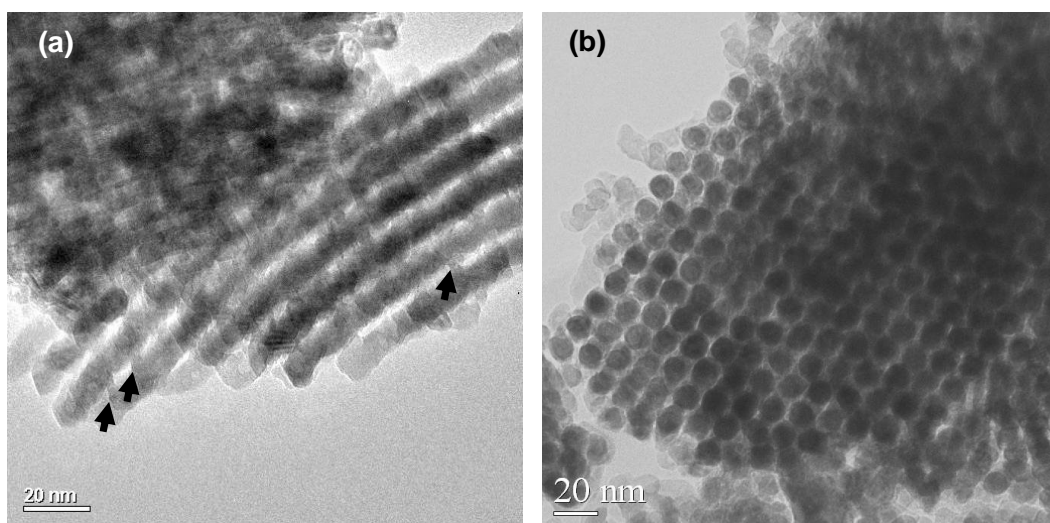


Figure 4-2. Low magnification TEM images of cobalt oxide with the negative replica of SBA-15 structure. (a) Side view of the nanorods with the black arrows indicating the nanobridges and (b) the end view of the nanorods in a hexagonal array viewed down the [0001] direction of the mesoporous phase.

The uniformity of the nanorod diameter can be seen in Figure 4-2 (b), which is measured to be as 9.6 nm. However, when measuring the nanorod diameter, which are uniform in shape with replicating the pore, in Figure 4-2 (a), it was found to be 8.9 nm. Both of these values are larger than the usual pore size for SBA-15 (8 nm). The increase in diameter could be attributed to the expansion of the cobalt oxide crystal. Additionally, the accuracy of the diameters measured is somewhat less accurate than HRTEM measurements due to it being more difficult to distinguish nanorod edges. As the pore of SBA-15 has effectively become the wall of the negative replica so the wall of the silica becomes the pore. With this, the pore size and shape is more continuous and open than the closed cylindrical pores of SBA-15.

As with the single crystal of chromium oxide, the SAED examination of the cobalt oxide material showed a 2D single crystal pattern. This was indexed to the cubic unit cell of  $\text{Co}_3\text{O}_4$  with space group  $Fd3m$  and lattice parameter  $a = 0.8085 \text{ nm}$  (JCPDS 781970)<sup>3</sup> and can be seen in

Figure 4-3. The diffraction pattern is viewed down the  $[01\bar{1}]$  direction with the angle between the two spots of (200) and (111) being  $54.7^\circ$

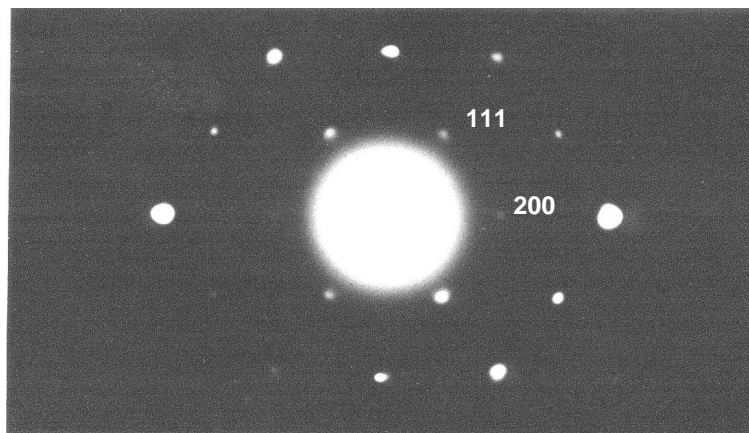


Figure 4-3. SAED pattern of the cobalt oxide porous single crystal templated by SBA-15, viewed down the  $[01\bar{1}]$  zone axis of cubic  $\text{Co}_3\text{O}_4$ .

Once a single crystal diffraction pattern is obtained, the magnification can be increased to view the atomic ordering of the cobalt oxide. Figure 4-4 shows a high magnification HRTEM image of the negative replica of SBA-15. The crystal can be indexed once again to cubic  $\text{Co}_3\text{O}_4$  viewing down the  $[0\bar{1}3]$  axis and the angle between the two identified crystal planes can be calculated to confirm the correct indexes. The image also shows the nanobridge between the nanorods, indicated by the black arrow, which confirms connection between the nanorods.

Figure 4-4 reveals that the nanorods are not perfectly cylindrical, which makes sense as that would make the inside of SBA-15 perfectly smooth. The diameter of the nanorods was found to be 8.5 nm, slightly lower than the measurements taken from the low magnification images, however far more accurate.

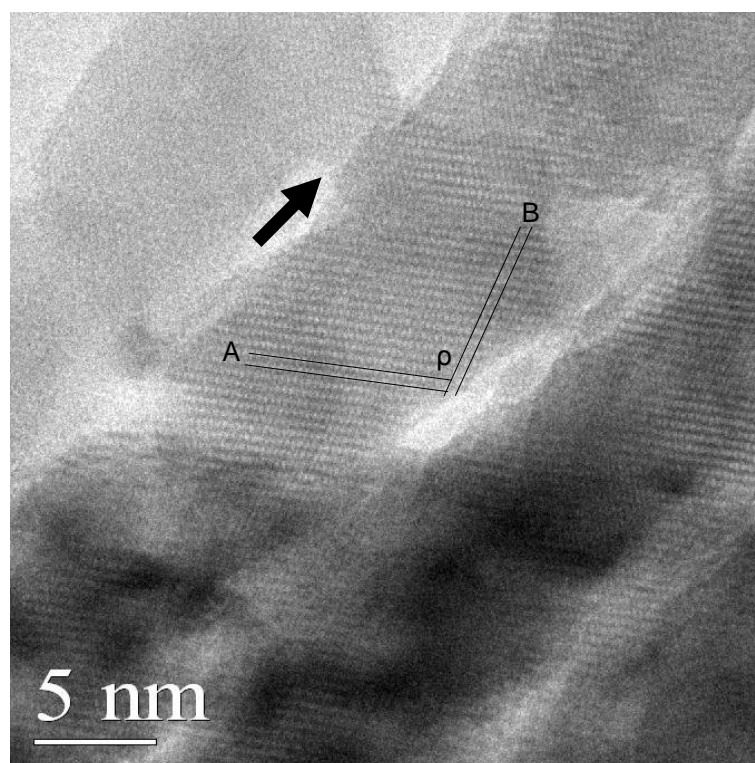


Figure 4-4. HRTEM image of the SBA-15 templated cobalt oxide PSC. The marked crystal lattice fringes are indexed to  $\text{Co}_3\text{O}_4$  fcc unit cell with space group  $Fd\bar{3}m$  and lattice parameter  $a = 8.085$  nm.  $A=(200)$  and  $B=(\bar{1}31)$  with  $\rho = 107.5^\circ$  viewed down the  $[0\bar{1}3]$  zone axis. The black arrow indicates a bridge between the nanorods with the same crystal orientation.

#### *XRD study of crystallisation*

The investigation of the decomposition temperature of cobalt nitrate in the SBA-15 was done much in the same way as in the case for chromium nitrate. Figure 4-5 shows the XRD patterns of a temperature study ranging from 125 °C to 200 °C in 25 °C increments, with 5 h dwell time at each of the target temperatures. As can be seen by the patterns, above 150 °C,  $\text{Co}_3\text{O}_4$  had been formed and at 125 °C, peaks that could not belong to  $\text{Co}_3\text{O}_4$  were seen. However, the peaks could not be easily distinguished so a time dependent study was carried out.

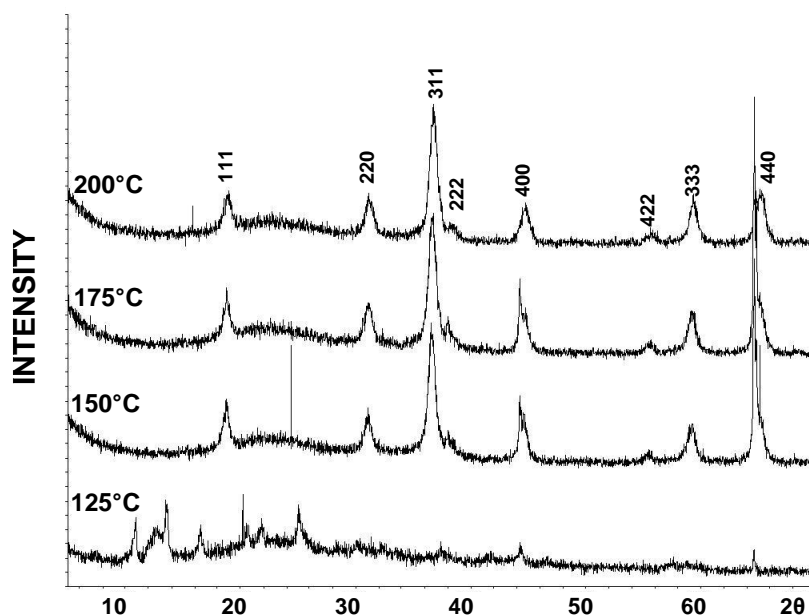


Figure 4-5. XRD patterns for a temperature study of the decomposition of cobalt nitrate in SBA-15. The top pattern is indexed to cubic  $\text{Co}_3\text{O}_4$ .

The temperature for the time dependent study was  $150\text{ }^\circ\text{C}$  and the samples were quenched with a range from 0.5-2 h in 0.5 h increments. The XRD patterns, shown in Figure 4-6, reveal that before forming the cobalt oxide, the cobalt nitrate goes through two metastable intermediates inside the mesopores. At both the 0.5 and 1 h stage, the two intermediates are both present, which then both start to disappear to form the cobalt oxide by 1.5 h and are completely gone after 2 h at  $150\text{ }^\circ\text{C}$ . The two intermediates were found to be  $\text{Co}(\text{NO}_3)_2 \cdot 2\text{H}_2\text{O}$  and  $\text{Co}(\text{OH})\text{NO}_3 \cdot \text{H}_2\text{O}$ . The former had a monoclinic unit cell with parameters of  $a = 1.429$ ,  $b = 0.6139$ ,  $c = 1.2661\text{ nm}$  and  $\beta = 112.79^\circ$  with a space group of  $I2/a$  (JCPDS 251219)<sup>4</sup>, whereas the latter was also a monoclinic unit cell with parameters  $a = 1.7757$ ,  $b = 0.3142$ ,  $c = 1.4188\text{ nm}$  and  $\beta = 113.55^\circ$  with a space group of  $P2_1/c$  (JCPDS 480091)<sup>5</sup>. The XRD peak ratio between  $\text{Co}(\text{OH})\text{NO}_3 \cdot \text{H}_2\text{O}$ / $\text{Co}(\text{NO}_3)_2 \cdot 2\text{H}_2\text{O}$  increases when the time is 1 h as opposed to the 0.5 h.

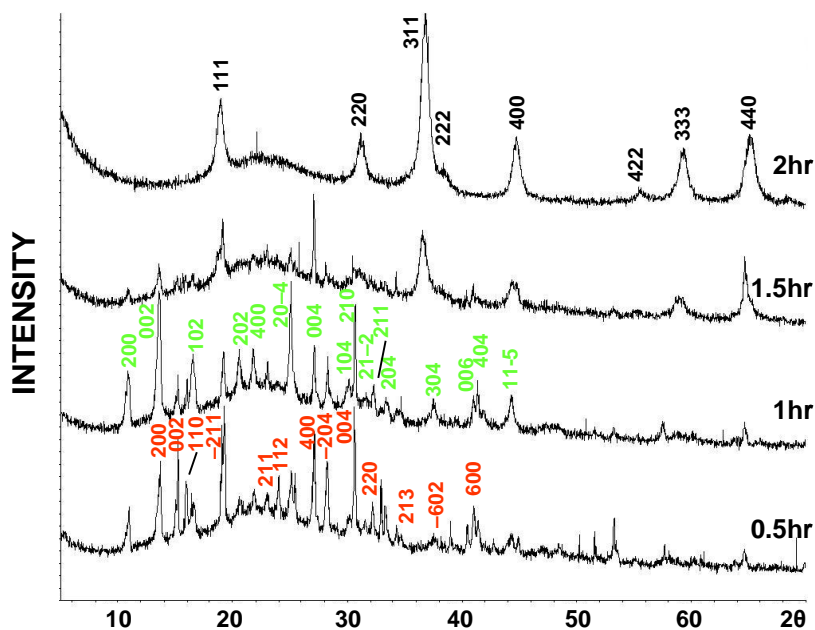


Figure 4-6. XRD patterns of the time dependent decomposition of cobalt nitrate within SBA-15 occurring at 150 °C in 0.5 h increments. The pattern with the 0.5 h treatment is indexed to monoclinic  $\text{Co}(\text{NO}_3)_2 \cdot 2\text{H}_2\text{O}$  (red) and the pattern with 1 h treatment is indexed to the monoclinic  $\text{Co}(\text{OH})\text{NO}_3 \cdot \text{H}_2\text{O}$  (green). The 2 h pattern is indexed to cubic  $\text{Co}_3\text{O}_4$  (black).

The above XRD data implies that the first step of the decomposition of the cobalt nitrate hexahydrate, is the loss of four water molecules to crystallise into the cobalt nitrate dihydrate. This crystal then undergoes a phase transition to the cobalt hydroxide nitrate monohydrate by losing one  $\text{NO}_3^-$  anion and a proton. The  $\text{Co}_3\text{O}_4$  is then formed by losing the second  $\text{NO}_3^-$  anion and the remaining water molecule. The cobalt ion remains in a 2+ oxidation state throughout the intermediates and it is only after the cobalt oxide forms that it partially oxidises to 3+.

On the other hand, when the cobalt nitrate is decomposed, with no mesoporous material present, the results are remarkably different. A time dependent study at 150 °C, the temperature that cobalt oxide crystallises in SBA-15, was carried out over the time range of 1-5 h in 1 h increments. After the analysis of the XRD patterns, Figure 4-7, it revealed two interesting results. The first was that even after 5 h at 150 °C, the material had still not formed the cobalt oxide. The

second was that not only did the intermediate phase not change between 1-5 h at 150 °C but it was a different intermediate than what was seen previously. The pattern was indexed to triclinic  $\text{Co}(\text{NO}_3)_2 \cdot 4\text{H}_2\text{O}$  with space group  $P\bar{1}$  and unit cell parameters  $a = 0.5516$  ,  $b = 0.5596$  ,  $c = 0.7228$  nm,  $\alpha = 102.38^\circ$  ,  $\beta = 97.74^\circ$  and  $\gamma = 120.16^\circ$  (JCPDS 742040).<sup>6</sup>

A temperature study was carried out, dwelling for 5 h at each target temperature, to determine when the cobalt oxide formed and it was found to be 225 °C. Below 225 °C, the cobalt nitrate stayed in the tetrahydrate form. By taking the sample out at the 1 h and 2 h stages at 225 °C, it was found that the cobalt oxide had started to become the major phase after 2 h, seen in Figure 4-8. The 1 h sample was found to have a second intermediate, in the form of the dehydrate of the cobalt nitrate. The  $\text{Co}(\text{NO}_3)_2$  was indexed to a primitive cubic unit cell with the parameter  $a = 0.741$  nm (JCPDS 190356).<sup>7</sup>

The reduction of the crystallisation temperature, when comparing with and without the presence of mesopores, correlates with the data obtained for the chromium oxide in the previous

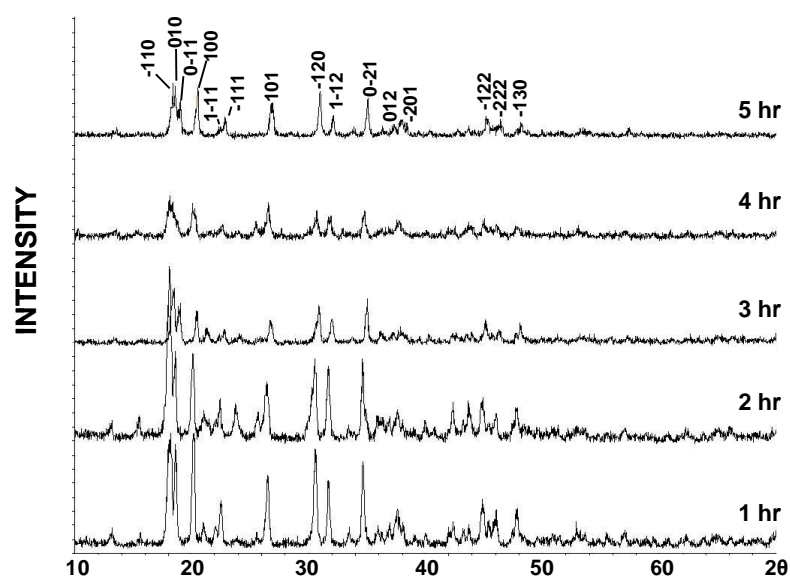


Figure 4-7. XRD patterns from samples taken out of a furnace at 150 °C at various time intervals. The diffraction peaks remain constant and can be indexed to triclinic  $\text{Co}(\text{NO}_3)_2 \cdot 4\text{H}_2\text{O}$ .

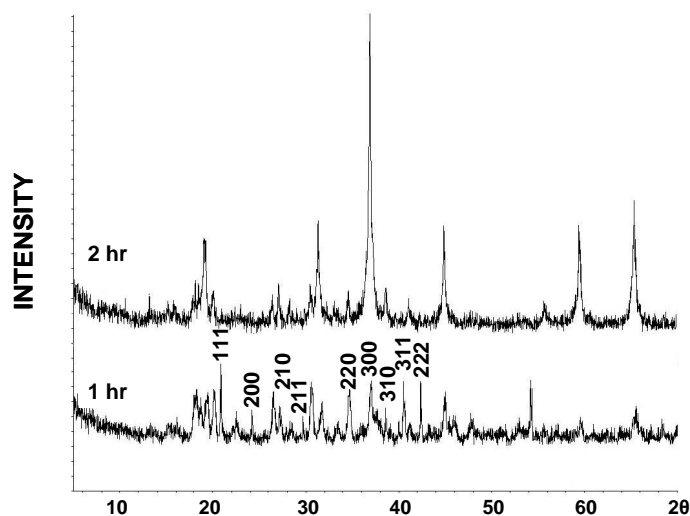


Figure 4-8. XRD patterns taken for samples after undergoing 225 °C at different times. The top pattern's major peaks can be indexed to  $\text{Co}_3\text{O}_4$  and the bottom pattern's peaks can be indexed to  $\text{Co}(\text{NO}_3)_2$  (shown) and  $\text{Co}(\text{NO}_3)_2 \cdot 4\text{H}_2\text{O}$  (not shown).

chapter. Additionally, a difference in the metastable intermediate products, present in the decomposition of the cobalt nitrate hexahydrate to the cobalt oxide, can also be seen. In fact, the cobalt hydroxide nitrate monohydrate is very uncommon, and it is due to this that the crystal structure was not solved until 1992 by Petrov *et al.*<sup>5</sup> The paper revealed that during the decomposition of the nitrate, the hydroxide nitrate only forms small fine crystals on the surface and with a very low yield. The low yield meant that the hydroxide nitrate had to be made from other sources for Petrov *et al* to obtain a large enough quantity to solve the crystal structure.

The appearance of strong peaks for not only  $\text{Co}(\text{OH})\text{NO}_3 \cdot \text{H}_2\text{O}$  but also  $\text{Co}(\text{NO}_3)_2 \cdot 2\text{H}_2\text{O}$  can be attributed to more than the exothermic and endothermic processes described in the previous chapter and Labus' paper but also the increase of the surface area of the cobalt nitrate hexahydrate.<sup>8</sup> If the  $\text{Co}(\text{OH})\text{NO}_3 \cdot \text{H}_2\text{O}$  tends to only form on the surface of the cobalt nitrate without the presence of mesopores, then it stands to reason that it is likely that with the mesoporous material increasing the surface area that  $\text{Co}(\text{OH})\text{NO}_3 \cdot \text{H}_2\text{O}$  would also increase in

yield. Additionally, the crystal width, which is restricted by the pore diameter, would be relatively small, at around 8 nm, and so crystallisation of these materials would be relatively easy.

### 4.3 Cobalt oxide in KIT-6

After cobalt oxide was formed in the KIT-6, the template was subsequently removed. Although there are several differences between the chromium oxide and the cobalt oxide templated by KIT-6, which will be discussed later in the chapter, there are also similarities. The shape of the cobalt oxide particles are spherical, seen in Figure 4-9 (a), allowing for it to be concluded that this effect is most definitely from the parental mesoporous channels conforming the crystal growth direction from within the 3D mesoporous system. The size of the cobalt oxide particles is larger than chromium oxide, in the range of 200-400 nm, although they are obviously still smaller than the micrometer scale of the KIT-6. Predictably, the cobalt nitrate decomposed into cobalt oxide without the presence of mesoporous silica does not have any particular fixed size or shape (Figure 4-9 (b)).

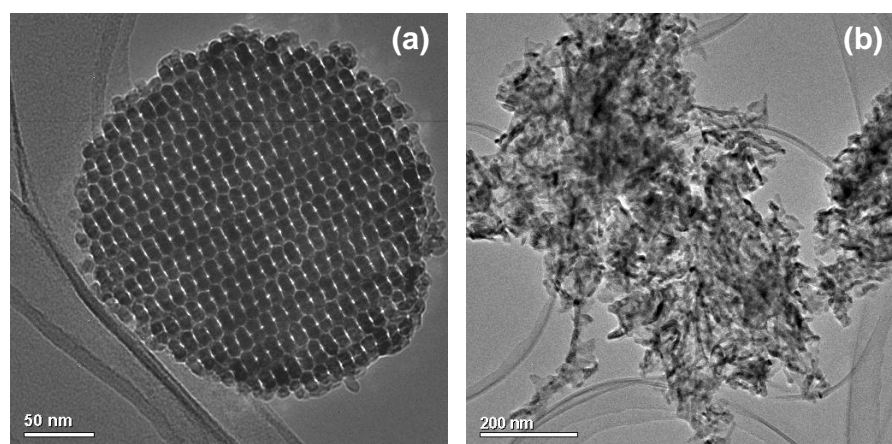


Figure 4-9. (a) Low magnification TEM image of a cobalt oxide spherical particle, templated by KIT-6, as an example of how the mesopores of the parental material effects the crystal growth. The mesopores are viewed down

the [110] direction. (b) TEM image of cobalt oxide crystals, formed by the decomposition of cobalt nitrate without the presence of mesoporous silica, showing no shape or size preference.

By tilting the particle to view down a different mesopore direction, it can be seen that cobalt oxide more truly replicates the mesopore channels of KIT-6 than chromium oxide. Like the carbon replicas<sup>9</sup>, each cobalt oxide crystal uses both of the pore systems, whereas chromium oxide only uses one. In Figure 4-10, the particle is viewed down the [111] direction of the mesopores and as a result, the bicontinuous framework of the mesopores can be observed.

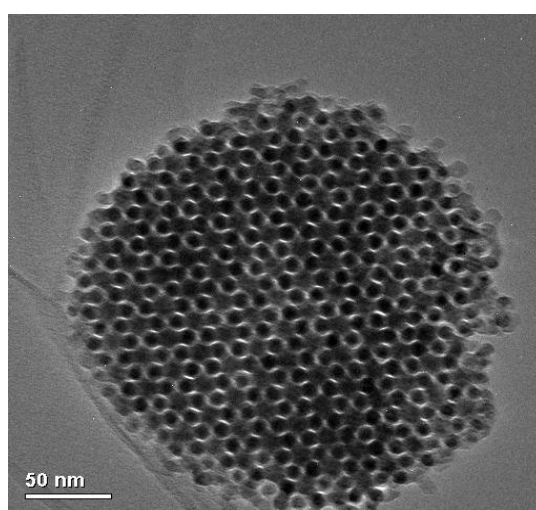


Figure 4-10. TEM image of mesoporous cobalt oxide viewed down the [111] of the mesopore structure. The image reveals that both mesoporous channels of KIT-6 have been replicated.

By checking the diffraction pattern of these mesoporous cobalt crystals, it was revealed that even though both channels were involved, they formed a single crystal. Figure 4-11 shows an SAED pattern for one of these particles. This confirms that the cobalt oxide particles are in the form of  $\text{Co}_3\text{O}_4$ , indexed to the cubic form viewing down the  $[1\bar{1}0]$  axis, and that the particles are single crystal. This also reveals that the mesoporous channels must have some sort of connection similar to the micropores in SBA-15. If there was no connection, then no communication would occur between the particles and therefore a single crystal could not be formed. As the pore systems are intertwined with each other, it is very difficult to view the nanobridges between the

nanorods. Additionally, the fact that both channels, forming the spherical particle, have the same diameter as well as having the same central position in every particle further rules out the crystal growth occurring independently in each channel.

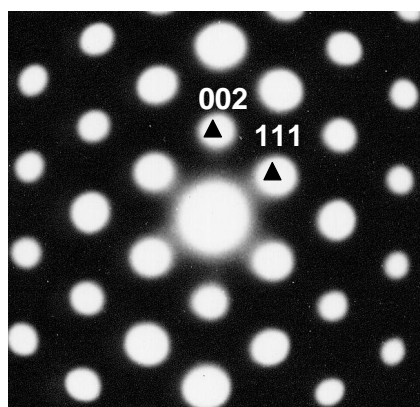


Figure 4-11. SAED pattern showing the PSC cobalt oxide particles to be single crystals. The pattern is indexed to cubic  $\text{Co}_3\text{O}_4$  viewed down the  $[1\bar{1}0]$  crystal zone axis.

The single crystallinity of the material can also be confirmed by high magnification HRTEM imaging. Figure 4-12 shows the PSC  $\text{Co}_3\text{O}_4$  viewed down the  $[23\bar{3}]$  zone axis. The two crystal planes can be indexed to  $(022)$  and  $(3\bar{1}1)$  which are confirmed by the angle between them as  $90^\circ$ . The circular end of the nanorods, created in the pore systems, can clearly be seen in the image. Once again, it is worth noting that with both pore systems being filled with the crystal an unclear mesoporous structure at high magnification results as there is always the other nanorod intertwined underneath, unlike the chromium oxide images from the previous chapter.

Additionally, there seems to be no relation between the mesoporous structure and the crystal structure, as was seen with the chromium oxide PSC formed by the dual solvent method. Although, it can not be understood why a dual solvent method would have this effect whilst the

ethanol method does not, it is understandable that the cobalt nitrate in ethanol would not lead to this phenomenon as chromium nitrate in ethanol did not exhibit it.

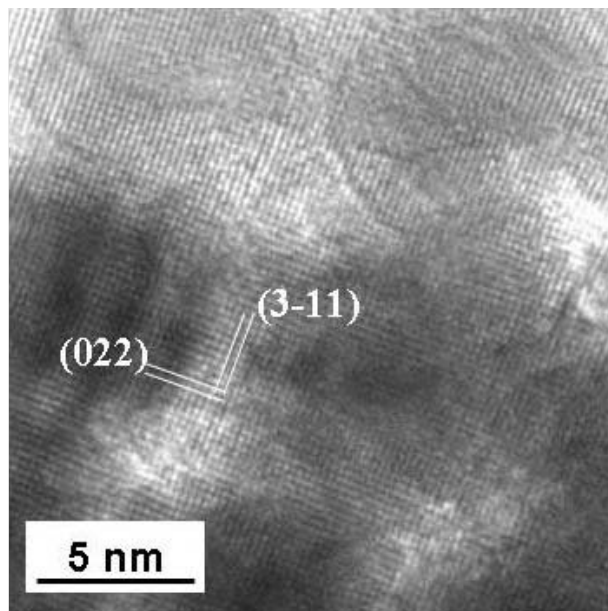


Figure 4-12. HRTEM high magnification image of cobalt oxide PSC viewed down the  $[2\bar{3}\bar{3}]$  crystal zone axis. The angle between the two planes of (022) and  $(3\bar{1}1)$  is  $90^\circ$ .

#### *Isotherm Data for PSC*

From the isotherm data of the adsorption of nitrogen onto the cobalt oxide PSC, which was templated by KIT-6, similarities and differences between this and the chromium oxide PSC can be observed. The first similarity is the loss of microporosity, which again is attributed to be from the bridging pores of the parental material, which is obviously absent in the crystals. However, whereas the chromium oxide did not have these channels since it only filled one pore system, the cobalt oxide has nanobridges in replacement of the micropores connecting the nanorods grown in the two systems.

Looking at the adsorption branch of the isotherm, Figure 4-13 (a), a slight shape in the curve at  $P/P_0 = 0.5$  and also at 0.8 can be seen, although the branch is not very steep. This leads to the

two respective pore size distribution values of ~4 and ~9 nm, shown in Figure 4-13 (b). This is similar to the two slight inflections in the pore size distribution graph of chromium oxide, Figure 3-15 (b). Since the adsorption branch was not very steep, the pore size distribution graph is very broad.

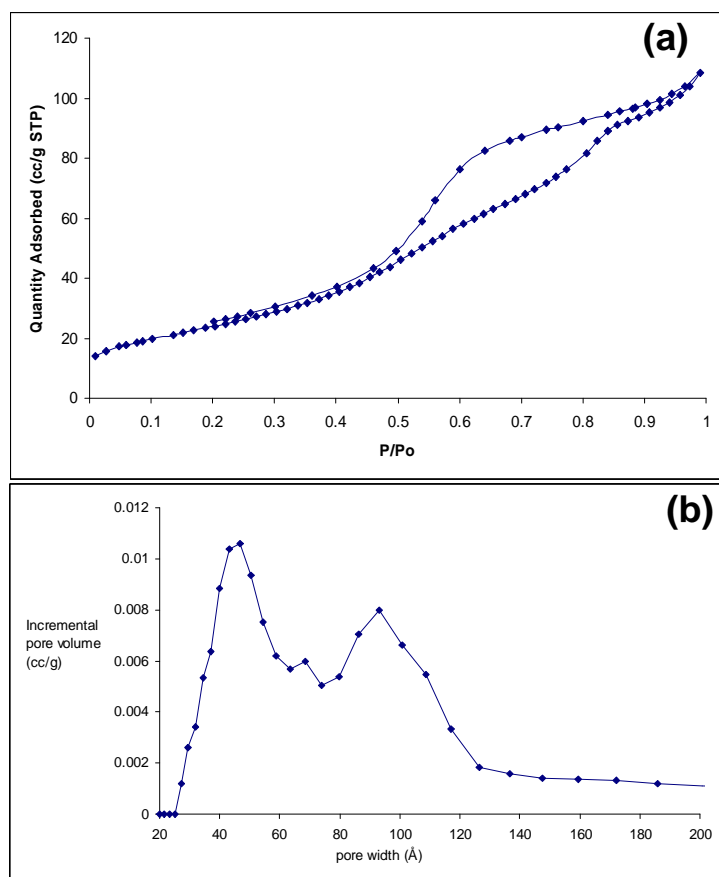


Figure 4-13. Nitrogen adsorption (a) isotherm showing the adsorption (bottom) and desorption (top) curves with the corresponding (b) pore size distribution graph.

The specific surface area of the cobalt oxide was measured at  $92 \text{ m}^2/\text{g}$  and a pore volume of  $0.167 \text{ cm}^3/\text{g}$ . Assuming the density of the crystal part of PSC cobalt oxide is the same as bulk cobalt oxide at the value of  $6.07 \text{ g cm}^{-3}$ , the specific surface area to volume was calculated as

$$\frac{1 \text{ g}}{\left(0.167 + \frac{1}{6.07}\right) \text{ cm}^3} \times 92 \text{ m}^2 / \text{g} = 277 \text{ m}^2 / \text{cm}^3 \quad (4.3)$$

This is about 60 % of the specific surface area per volume of KIT-6,  $462.9 \text{ m}^2 \text{ cm}^{-3}$ , (3.4), which although is a reduction, it was not reduced as much as chromium oxide PSC,  $114.2 \text{ m}^2 \text{ cm}^{-3}$  (3.3). Whilst the crystal of cobalt oxide is denser, by about 16 %, than the chromium oxide crystal, it has a 140 % increase in surface area, over double the surface area. This can be attributed to the presence of nanobridges, in the cobalt oxide, allowing for the second channel to be used without the loss of area.

#### *Formation mechanism*

With the fact that cobalt and chromium form a PSC and have similar data for the growth inside the template, a possible formation mechanism can be suggested. There are two possible main formation mechanisms that are most likely. The first method is the single seed, where the PSC grows from a small seed within the parental material. The second method is that the material initially forms nanoparticles and then the nanoparticles join together and change orientation to match the other particles. Both mechanisms, however, encounter some problems.

Although initially, the single seed approach seems the least likely as the walls of the silica are amorphous, and therefore no region of the template would have favoured conditions for the beginning of a seed formation above any other, there are problems with the nanoparticle approach. Firstly, if the nanoparticles were formed first, the heating time is simply too short (5 hours) for the nanoparticles to form the single crystal at such a low temperature ( $550 \text{ }^\circ\text{C}$ ). Additionally, as the temperature is so low, once the metal oxide is formed, it is harder for the crystal domains to align when the temperature is so far from the decomposition/melting point of the oxides. For  $\text{Co}_3\text{O}_4$ , it decomposes at  $900 \text{ }^\circ\text{C}$ , and for  $\text{Cr}_2\text{O}_3$ , it melts at  $2330 \text{ }^\circ\text{C}$ . Even though it can be seen that the mesopores can reduce the temperature required to decompose the nitrate, it is not a significant enough decrease for the chromium oxide to melt, and if it decreased the  $\text{Co}_3\text{O}_4$  decomposition temperature, then a different product would have been the result,  $\text{CoO}$ .

With this fundamental information, the multiseed approach was suggested. This approach means that multiple seeds are formed in different areas of the mesoporous material, and follows the single seed method of formation. This not only solves the problems raised by the nanoparticle approach but also the non site specific single seed method. It has been shown that the particle size of the PSC is much smaller than the mesoporous silica template, and that multiple PSCs can be formed in each template particle (Figure 3-11). However, a problem does arise of why the material forms a single crystal rather than a polycrystalline material since the seed formation is entirely random.

Seed formation is thermodynamically unfavourable, and as such the majority of seeds will revert back to their amorphous state. It is only when the seed reaches a critical size, that seed growth become thermodynamically favourable and the crystal can grow. When the crystal starts to grow, material will migrate towards the growing crystal and new seed formation, since it is thermodynamically unfavourable, will be sacrificed for the growth of the seed that has reached critical size.

It is also known that large crystals will take priority over smaller crystals due to Ostwald ripening.<sup>10</sup> Ostwald ripening is that a larger crystal will cause a smaller crystal to be used in increasing its size. This is due to the centre of crystals being very thermodynamically stable whereas the surface of the crystal is more thermodynamically unstable. Although the surface of a larger particle is obviously bigger and therefore more thermodynamically unstable, they also have a larger core, causing the average thermodynamic stability to greatly increase to a larger extent than a small particle with a small core. With the above reasoning, it is understandable how the single crystal forms rather than polycrystalline material. A very slow crystal growth would also enhance the formation of PSCs.

### Conjoined PSCs

Since the walls are amorphous, and the seed formation is entirely random, it stands to reason that two seeds could form at roughly the same time and have a similar growth rate. By the time these crystals meet, if they were both of a significant size, and therefore similar thermodynamic stabilities, they will join together rather than break the other down. Whilst studying the cobalt oxide PSC, it was found that conjoined particles were present, and these were attributed to two PSCs growing in the same template in close proximity. Figure 4-14 (a) shows a TEM image of a pair of conjoined particles. It can clearly be seen that the both particles have the same mesoporous orientation. Additionally, the diffraction patterns (insets) reveal that although they do not have the same crystal orientation, they are single crystals in their own right. The crystal orientation does not appear to have any relation to each other, with the top and bottom pattern being viewed down the  $[\bar{1}12]$  and  $[\bar{2}33]$  zone axes respectively.

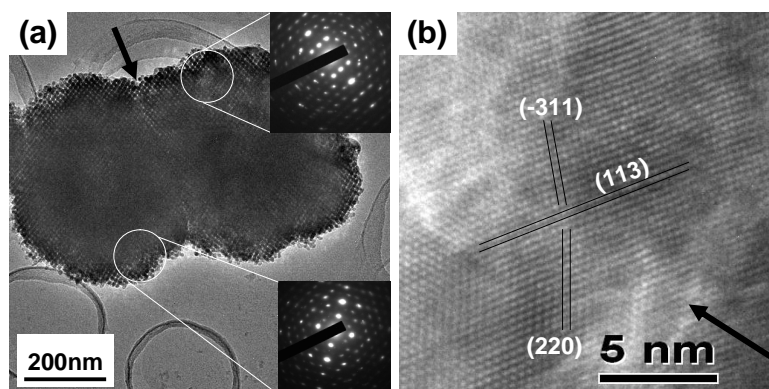


Figure 4-14. TEM images of two conjoined particles of PSC  $\text{Co}_3\text{O}_4$ . (a) Low magnification image with the common mesopore structure but different crystal orientations, indicated by the SAED patterns (insets), for the right and left particles. (b) High magnification image of the integration point of a second set of conjoined particles revealing the common (113) plane. For both images the black arrow indicates the integration point.

With the previous knowledge of the cobalt oxide forming spherical nanoparticles in KIT-6, it can be estimated where the point of integration between the particles is located. Looking at the

HRTEM image of another set of conjoined particles, Figure 4-14 (b), the line of integration can be observed due to the change in crystal orientation, indicated by the black lines. The integration point is indicated by a black arrow and the crystal orientations share a common plane of (113). Although the common plane is shared, the crystal orientations of the two PSC particles are different, with the upper and lower particles viewed down the  $[15\bar{2}]$  and  $[1\bar{1}0]$  zone axes respectively.

By looking in more detail at the SAED patterns that are the insets for Figure 4-14 (a), it can be seen that a common plane is also present. By chance, this is also the (113) plane, and was found to be common by measuring the angle between a line perpendicular to the pattern's edge and the normal direction of the (113) plane of the SAED pattern, Figure 4-15. Although the angles do not exactly match, it was found that they were within 1-2° of each other, with  $\rho$  and  $\theta$  being  $\sim 16^\circ$  and  $\sim 15^\circ$  respectively.

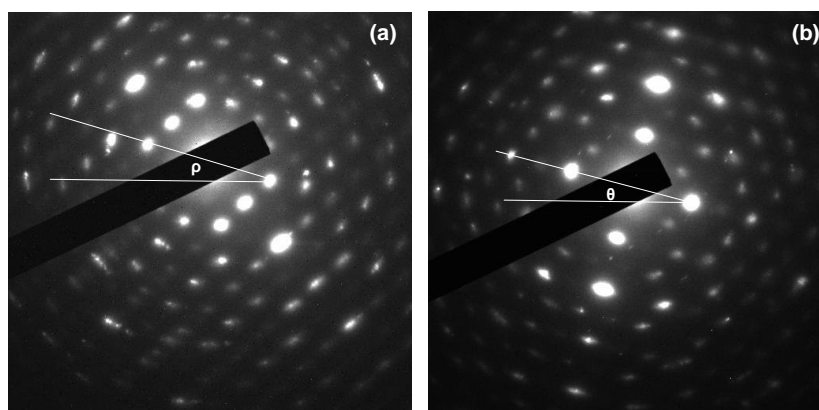


Figure 4-15. Diffraction pattern insets from Figure 4-14 (a), from the (a) top and (b) bottom right respectively. The angle for  $\rho$  and  $\theta$  are found to be very similar indicating the common plane.

By creating the theoretical unit cell viewed down the  $[\bar{1}12]$  axis and the corresponding diffraction pattern, the (113) plane can be viewed. The pattern was tilted to the angle of the

experimental pattern seen in Figure 4-15 (a). The computer simulated diffraction pattern, Figure 4-16 (a), shows that the (113) spot is relatively strong; the [113] axis is marked by an arrow. In the theoretical unit cell of cubic  $\text{Co}_3\text{O}_4$ , Figure 4-16 (b), the (113) plane is also marked with a line, which is perpendicular to the [113] axis line from the diffraction pattern. From the (113) plane, it can be seen that there is not a high density of cobalt atoms (green) or oxygen atoms (orange), which leads to the conclusion that the fact that the (113) plane is the common plane for both pairs of conjoined particles, seen in Figure 4-14, is purely coincidental.

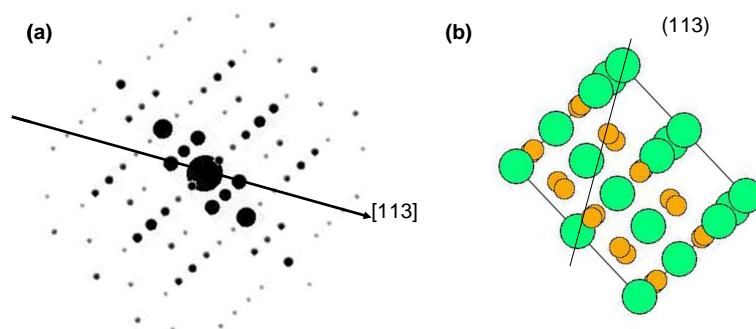


Figure 4-16. Theoretical (a) diffraction pattern showing the [113] axis and (b) unit cell with the (113) plane, of cobalt oxide in  $Fd\bar{3}m$  space group viewed down the  $[\bar{1}12]$  zone axis.

Although conjoined PSCs could be seen in the cobalt oxide sample, it could not be seen in the chromium oxide sample. A variety of reasons could be used to explain not seeing this happening in chromium oxide. If the PSCs of chromium oxide are attracted into clusters by small particle interactions, then it would be very difficult to distinguish between the conjoined particles and clustered particles. Additionally, since the chromium oxide is using only one pore system then it would be more difficult for integration points to occur.

#### 4.4 Nanobridges in KIT-6 templated PSCs

As mentioned above, only one pore system of chromium oxide is being formed in the KIT-6 in contrast to the two pore systems in cobalt oxide. Figure 4-17 shows PSCs of chromium oxide and cobalt oxide templated by KIT-6 viewing down the same mesoporous direction. A possible explanation for this can be suggested by looking at the formation of the nanobridges. To understand the formation of the nanobridges, the pore structure for the silica must first be observed.

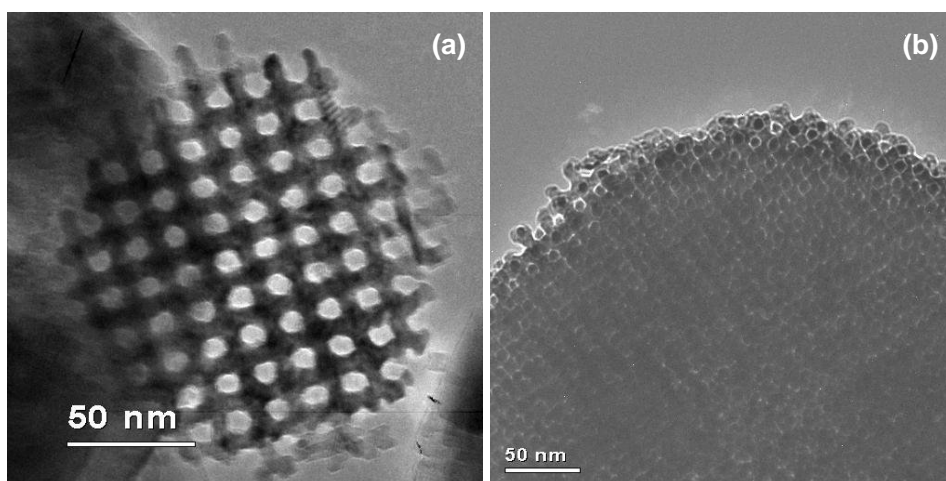


Figure 4-17. TEM images of PSCs (a) chromium oxide and (b) cobalt oxide, templated by KIT-6. Both particles are viewed down the [100] direction of the mesoporous structure.

When using triblock copolymers, micropores between the mesopores can form.<sup>11</sup> This is due to the tails of the surfactant micelle being embedded into the silicon walls. When the surfactant is decomposed by calcination, the tails of the surfactant are also destroyed leaving the micropores. By looking down the end on view of a pair of mesopores, Figure 4-18, it can clearly be seen that it has the large mesopores with the small micropores coming close to connection.

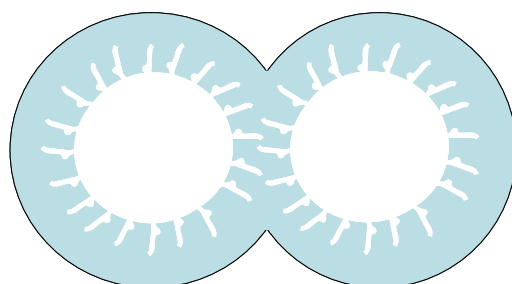


Figure 4-18. Diagram of the end on view of two pore entrances of neighbouring channels with micropores created by the surfactant.

There are two possible methods on how the nanobridge is formed, however with the information reported, only one seems likely. The first possible method is that the micropores from each pore will connect with each other, either before or after calcination. This could be a result of micropores that are in close proximity will either stop the silica from forming a wall in between them or by weakening the silica wall in that area causing the silica to collapse and leaving a connected system. The crystal can then grow through this pore forming the nanobridge. The second possibility is that the micropores stay in close proximity but are not connected. It is only when the crystal grows in the micropore, that the micropore expands breaking the thin silica wall between the neighbouring micropore allowing for the crystal to carry on growing and creating the bridge.

It is not clear whether the micropores are connected in both systems of SBA-15 and KIT-6; however isotherm data does suggest the micropore presence. Since the micropores are present in both, this can not be the only factor that results whether a bridge has formed for several reasons, the first of which can be seen by looking at SBA-15. SBA-15 is made up of relatively straight pores, this means that the wall thickness remains constant between two pore systems, see Figure 4-19 (a). If every micropore resulted in a nanobridge then we would not see anything like that which was seen in Figure 4-4, but a constant crystal all the way down the length of the nanorod.

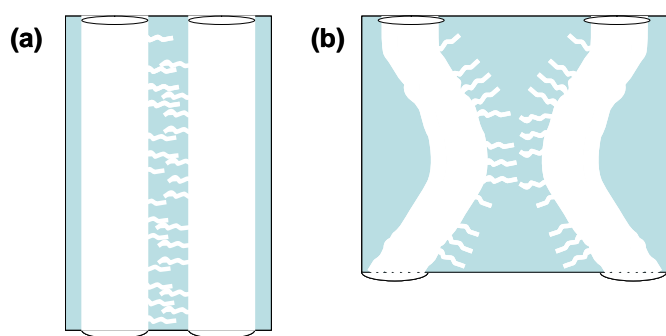


Figure 4-19. Diagram showing two channel systems and their micropores with (a) parallel and (b) curved channels.

Since this is not the case, as most nanobridges are around 2-3 nm in diameter, which is not only larger than the micropores but are less frequent, then something else must be occurring here.

Amorphous material tends to be loosely packed, as opposed to crystalline material. When a crystal grows and meets amorphous material, it can push the material away. This means that when a crystal grows in mesoporous silica, the amorphous walls are not rigid and can be compressed. The crystal will enter into and grow in one micropore causing the neighbouring micropores to collapse as the walls are compressed, or the crystal will grow in the neighbouring micropores too and the walls collapse between them and cause other unfilled micropores to collapse.

Considering the chromium oxide, in KIT-6, not being able to fill in the micropores, whereas the cobalt oxide can, it could be the amount of compression each crystal puts on the wall. Whilst this does not matter for SBA-15, it does have an effect on KIT-6. By looking at the diagram of SBA-15, Figure 4-19 (a), it can be seen that the pressure from the crystal on the SBA-15 walls will remain constant throughout the pores. However, when considering KIT-6, with the wall thickness changing as the pore systems move close to each other and then apart, the pressure will be different, Figure 4-19 (b). As the wall thickness decreases, more pressure will be on the narrow wall than the wider wall. Additionally, when the wall is thick then the channel is curved away from the wall whereas when the wall is thin, the channel is curved into the wall, which

could decrease and increase the pressure on the wall respectively. This could increase the possibility of the collapse if the pressure is significant. If this is what happens then, chromium oxide crystal must put on more pressure than cobalt oxide crystal due to the pore collapsing in KIT-6 for one and not the other. As chromium oxide is less dense than cobalt oxide, 5.21 and 6.07 g cm<sup>-3</sup> respectively, but has a similar rigidity due to being a crystal, there is a greater expansion of the crystal per volume.

Alternatively, the shape of the pores might not have a pressure effect. Looking at the micropores that connect the pores, it is more common in channels that are parallel with each other than curved channels that move close to each other and then apart. The higher the temperature will lead to a higher mobility of the amorphous silica and therefore the stability will decrease. Since it is known that the crystallisation of the cobalt oxide in the mesopores occurs at a lower temperature than that of chromium oxide, by 200 °C, then it can be assumed that the mesoporous silica will be less stable for chromium oxide crystallisation temperature. The percentage of pores collapsing could be the same for both KIT-6 and SBA-15, the only difference being the quantity of micropores that remain. For example, two channels running parallel to each other will have much more micropore connections, say 100 connections, than two channels that curve towards and then away from each other, say 30 connections. If chromium oxide crystallisation collapses 70 percent of the micropores then in curved channels the connections will be reduced to 9 but the parallel channels will still have 30 available. Additionally neighbouring micropore collapse, due to bridge formation, will cut this number even further. For cobalt oxide, the percentage collapse could be smaller, 20 %, and therefore would have 80 and 24 micropores remaining for parallel and curved channels respectively.

The third possibility for why one channel is filled as opposed to two channels being filled is a matter of chirality. If the chromium oxide crystal formation prefers the right hand channel as opposed to the left hand channel then only one channel would be filled. Unfortunately, this is

very hard to test what channel is filled by the chromium oxide if this is the case, which is discussed with the chirality of platinum replicas of similar systems.<sup>12,13</sup> However, the fact that chromium oxide forms smaller PSC particles than cobalt oxide suggest that this is not the case, as the material from the non preferred channel could migrate over to the preferred channel and therefore should be of a bigger size than the cobalt oxide rather than a smaller size. The fact that chromium oxide PSCs are smaller than cobalt oxide PSCs is indicative that the cobalt oxide appears to have a greater mobility, as not only is it bigger in one channel but is also bigger in the two channels. This means that the cobalt oxide PSC is not just twice as big as chromium oxide PSC, on average, but four times.

In summary, cobalt oxide has been shown to form porous single crystals when templated by mesoporous silicas SBA-15 and KIT-6. The single crystallinity of mesoporous cobalt oxide was confirmed by SAED and the atomic ordering was studied using HRTEM. XRD data from the studies of cobalt nitrate in mesoporous silica revealed that the decomposition temperature was significantly lowered. Additionally, the mesoporous confinement effect also revealed different decomposition intermediates than that of the decomposition of bulk cobalt nitrate without the presence of mesopore. A possible formation mechanism for cobalt oxide and chromium oxide was suggested and the conjoined PSC particles of cobalt oxide templated by KIT-6 was investigated revealing integration points of a common crystal plane between the particles. Finally, a comparison between KIT-6 templated PSCs of cobalt oxide, created in two channels, and chromium oxide, created in one channel, was made and possible reasons for this was discussed, including the importance of the micropores.

In the next chapter, the importance of the micropores is discussed further by looking at a few mesoporous silicas with different pore structures, which results in polycrystalline porous material. The chapter will also look at other metal nitrates using known templates and how their

different properties makes it difficult to form mesoporous material, either single crystal or polycrystalline.

## References

- [1] B.Z. Tian, X.Y. Liu, H.F. Yang, S.H. Xie, C.Z. Yu, B. Tu and D.Y. Zhao, *Adv. Mater.*, 2003, **15**, 1370
- [2] K.K. Zhu, B. Yue, W.Z. Zhou and H.Y. He, *Chem. Commun.*, 2003, 98
- [3] G. Will, N. Masciocchi, W. Parrish and M. Hart, *J. Appl. Crystallogr.*, 1987, **20**, 394
- [4] *Natl. Bur. Stand. (US) Monogr.*, 1974, **25**, 22
- [5] K. Petrov, N. Zotov, O. Garcia-Martinez and R. Rojas, *J. Solid State Chem.*, 1992, **101**, 145
- [6] B. Ribar et al, *Zb. Rad. Prir.-Mat. Fak. Ser. Biol.*, 1975, **5**, 65
- [7] D. Weigel, B. Imelik and M. Prettre, *Bull. Soc. Chim. Fr.*, 1964, 2600
- [8] S. Labus, A. Malecki and R. Gajerski, *J. Therm. Anal. Calorim.*, 2003, **74**, 13
- [9] F. Kleitz, S.H. Choi and R. Ryoo, *Chem. Commun.*, 2003, 2136
- [10] J.H. Yao, K.R. Elder, H. Guo and M. Grant, *Phys. Rev. B*, 1993, **47**, 14110
- [11] M. Kruk, M. Jaroniec, C.H. Ko and R. Ryoo, *Chem. Mater.*, 2000, **12**, 1961
- [12] H.J. Shin, R. Ryoo, Z. Liu and O. Terasaki, *J. Am. Chem. Soc.*, 2001, **123**, 1246
- [13] V. Alfredsson, M.W. Anderson, T. Ohsuna, O. Terasaki, M. Jacob and M. Bojrup, *Chem. Mater.*, 1997, **9**, 2066

## *5. Various Metal Oxides Using Different Silica Templates*

The previous chapters have shown two metal oxides using two different silica templates that form porous single crystals. This chapter looks at different metal oxides and different templates. While no PSCs of metal oxides were formed, possible reasons are suggested.

### 5.1 Synthetic methods of metal oxides

#### *Metal nitrate in ethanol method<sup>1</sup>*

This method was used for the metal nitrates of cobalt, iron and silver, in the templates SBA-16, FDU-12, and SBA-15, respectively.

0.3-0.6 g of the metal nitrate was dissolved in 8 g of ethanol, to which 0.15 g of mesoporous silica was added whilst stirring. After 2 h, the ethanol was allowed to evaporate off at room temperature in a wide-bottomed petri dish. Once dry, the powder was transferred to a crucible for the decomposition step in the furnace.

For SBA-15 fibres, due to being much lighter than the standard SBA-15, less template was used by weight of cobalt nitrate. For this, 0.47 g of cobalt nitrate was dissolved in 8 g of ethanol and 0.6 g of SBA-15 fibres was added to the stirring solution. The ethanol was evaporated as before and the resulting powder was transferred to a crucible.

#### *Crystallisation of metal oxide<sup>2</sup>*

The crucible containing the metal nitrate/mesoporous silica powder was placed into a furnace and heated to 550 °C for 5 h. The heating rate was 1-2 °C per minute and cooling back down to room temperature was gradual. The powder was then removed from the crucibles and XRD experiments were carried out.

The silica template was removed by either the HF or NaOH method depending on the metal. For cobalt oxide, the sample was stirred with 10 % HF solution for 8 h and the resulting metal oxide powder was separated out from the solution, which had been neutralised by sodium hydroxide, by centrifugation. The powder was washed and centrifuged three more times and then dispersed in ethanol for extraction from the tube. The ethanol was then evaporated off, leaving the cobalt oxide material behind. The template was removed for iron oxide and silver by stirring with 2 M NaOH at 70-90 °C for 8 h. The separation and washing of the sample, using the centrifuge, was carried out as mentioned above.

## 5.2 Porous metal oxides

By using cobalt oxide to negatively replicate a different silica template, other than that of SBA-15 and KIT-6, it would be expected to form a single crystal. Although the following materials do form a porous structure, the crystal structure is not single crystal.

### *Cobalt oxide in SBA-15 fibres*

SBA-15 fibres were prepared by Dr. Robert Hodgkins at Stockholm University, Sweden. The SBA-15 fibres differ to SBA-15, by being almost millimetre in size. This is due to the addition of Expancel spheres before the TEOS. The unexpanded spheres form a homogenous solution due to the density being similar to water. It is not until the maturation step that the spheres expand, disallowing the SBA-15 particles to spread out and therefore causing fusion of the particles as they mature, leading to the fibres. Cobalt nitrate was used to negatively replicate the mesopores in the hope that a larger porous single crystal could be created. When the cobalt nitrate was decomposed inside the pores, the cobalt oxide could be seen inside. The cobalt oxide appeared to fill a large area of the pore structure, Figure 5-1 (a), although some unfilled pores could still be

observed. This is obviously still due to the crystalline material contracting within the pores when the cobalt oxide is formed, as mentioned in the previous chapter.

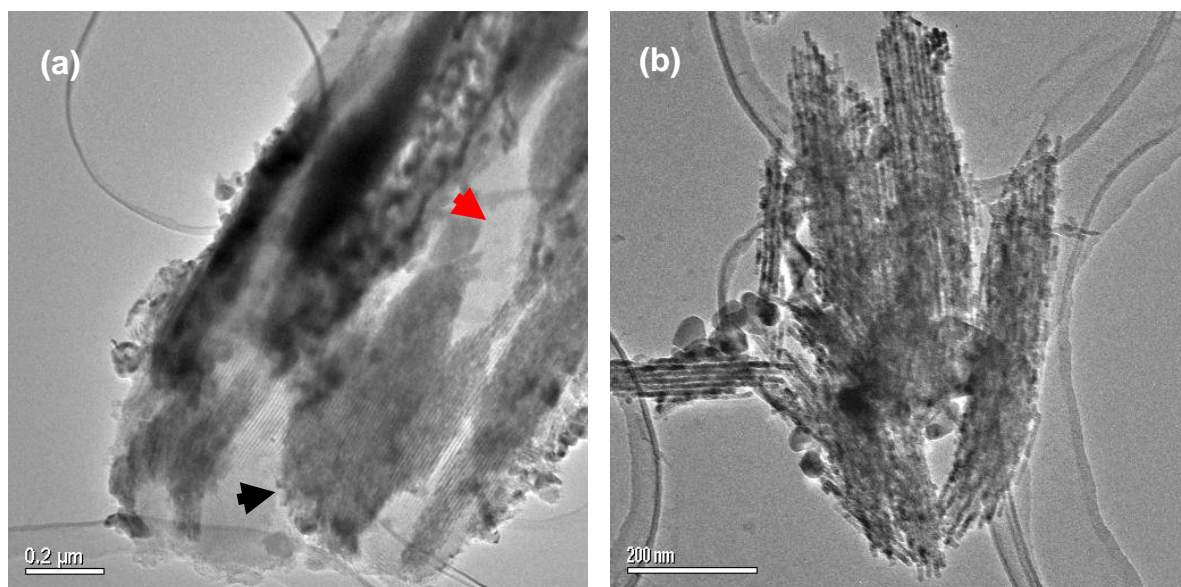


Figure 5-1. TEM image of (a) SBA-15 fibres after cobalt oxide has been formed inside. The black arrow indicates the dark region where the cobalt oxide crystal growth has concentrated inside the pores. The red arrow indicates the lighter region of the mesopores that has little or no cobalt oxide present. (b) TEM image of cobalt oxide fibres, after the SBA-15 template has been removed

Even from within the pores, the size of these crystals can be seen as somewhat larger than the crystals made in normal sized SBA-15. When the template is removed, the majority of the particles appear to be longer and thinner, Figure 5-1 (b). The length of the nanowires tend to be in the region of 400-700 nm, however some conjoined crystals can be seen forming a much longer length (1 micrometer), Figure 5-2. From Figure 5-2, it can clearly be seen that the cobalt oxide fibres do not simply overlap as you can see the continuous nanorod.

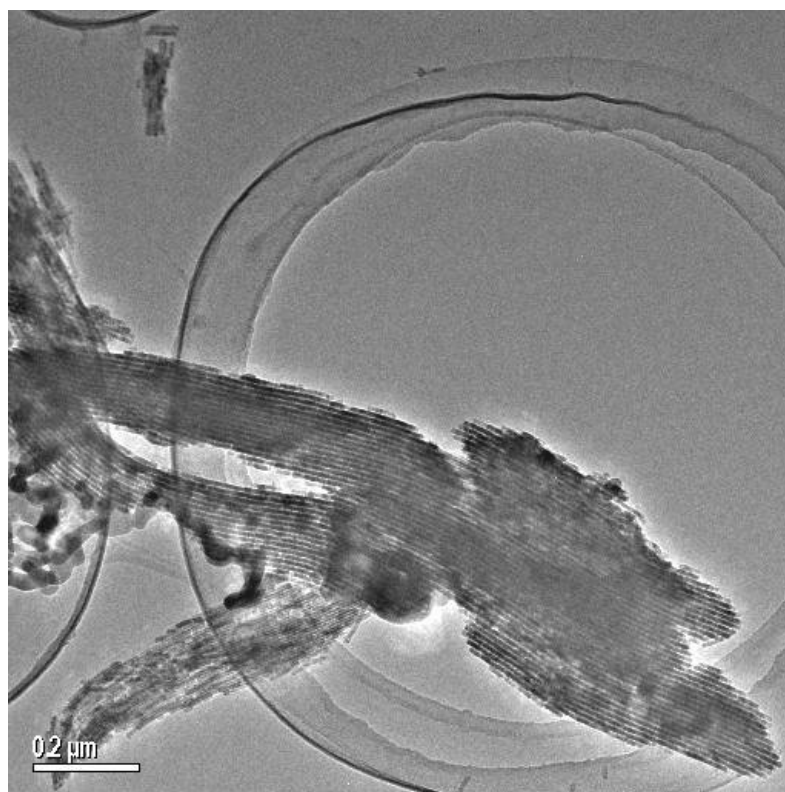


Figure 5-2. Low magnification TEM image of long cobalt oxide fibres, templated by SBA-15 fibres. Some of the nanorods are continuous over one micrometer in length suggesting these are conjoined particles rather than overlap.

The SAED pattern indicated that the cobalt oxide crystals had more than one crystal domain. This was expected, due to the nature of the conjoined particles. Although, even the particles that were separate, like that seen in Figure 5-1 (b), had 2-3 different crystal domains. With high magnification HRTEM, the crystal orientations of the particles were investigated. In the previous chapter, conjoined PSCs shared a common plane, which is thought to be essential for the particles to stay joined, Figure 4-14. However, when the HRTEM images of the nanorods of cobalt oxide fibres with different crystal domains were examined and the crystal orientations were calculated, it was found that no common plane was found.

Figure 5-3 shows an HRTEM image of the nanorods with two crystal domains. The crystal lattice was indexed to the fcc unit cell of  $\text{Co}_3\text{O}_4$  with space group  $Fd\bar{3}m$  and lattice parameter

$a = 0.8085 \text{ nm}$  (JCPDS 781970).<sup>3</sup> The top crystal domain was found to be viewed down the  $[1\bar{1}2]$  zone axis whilst the bottom crystal domain was found to be on the  $[\bar{3}14]$  projection. There does not appear to be a common plane between the two crystal orientations, despite being able to keep the mesoporous structure.

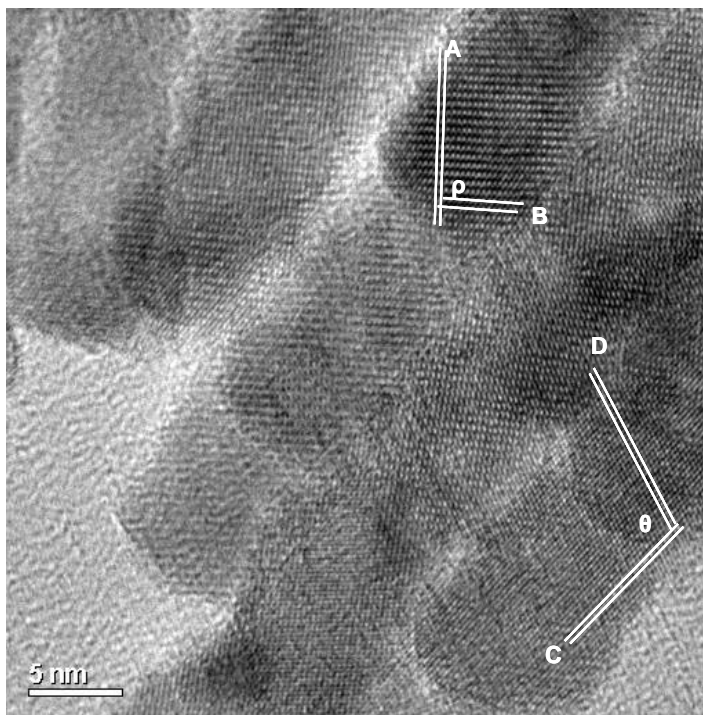


Figure 5-3. High magnification HRTEM image of the conjoined nanorod crystals.  $A=(\bar{1}11)$  and  $B=(220)$  where the angle between them is  $\rho = 90^\circ$  indicating the  $[1\bar{1}2]$  zone axis.  $C=(130)$  and  $D=(\bar{2}\bar{2}2)$  with the interplane angle being  $\theta = 110^\circ$ , indicating the  $[\bar{3}14]$  zone axis. There appears to be no relation between these two crystal orientations.

The cobalt oxide fibres show good connectivity with each other, despite the different crystals not having a common crystal plane. This correlates with polycrystalline material that still replicate the mesoporous structure, even without full crystal connection between the particles.<sup>4</sup>

There are a couple of possible reasons why the material forms several crystal domains rather than a single crystal, the first is the connectivity.

If the SBA-15 particles, due to the expanded Expancel spheres, are fusing together during the maturation step, the density of the silica could be increasing. This density increase could cause the collapse of the micropores, decreasing the chances of the nanobridges needed to form a single crystal. Additionally, if the regions of the SBA-15 are more segregated, due to the loss of a large quantity of micropores, then more crystal domains could grow unhindered by another crystal growing nearby. This can be ruled out almost immediately since the mesopore structure is retained by using nanobridges.

The second reason could be a higher amount of seed formation, which could be linked to the above information about the reduction of mesopores. If higher quantities of seeds are forming, then the amount of seeds reaching critical size would also increase. Other than the possibility of the reduction of micropores causing this, the amount of seed formation could also be due to the increase in the amount of cobalt nitrate per gram of template. Due to the SBA-15 fibres being so much lighter in weight than traditional SBA-15, less template was used per gram of cobalt nitrate. The ratio of grams of cobalt nitrate: SBA-15 increases from a 3:1 to 7.5:1 for cobalt nitrate: SBA-15 fibres. This seems the most likely explanation of the increase in seed formation. Also, it is worth considering that whether the low ratio in the previous experiments is the reason why a single crystal is formed and not a multicrystal. This suggests that when the crystal growth occurs with abundant material, it is not causing large scale migration of the precursor. It also appears that for the single crystal to form, not only the quantity of the precursor material can not be too high, or multicrystalline material may form, but the quantity of the precursor material can not be too low, as then there is not enough material to form the mesoporous replica, Figure 3-5.

With this information of the quantity of the precursor being important, as well as the importance of connectivity, it is worth looking at another template, SBA-16.

### Cobalt oxide in SBA-16

SBA-16 is a cubic mesoporous system. Although KIT-6, which was used in earlier experiments is also body-centered cubic and in a similar space group,  $Ia3d$ , SBA-16, which is  $Im\bar{3}m$ , is very different.<sup>5</sup> SBA-16 has a cage structure, with spherical pores connected by windows. In a way, this makes SBA-16 more of a true open 3D mesoporous network when compared to KIT-6, whose intertwined channels resemble SBA-15 more than other cubic systems, such as SBA-16 and FDU-12.

Once again, cobalt oxide was used to form the single crystal due to its past performance. Since the SBA-16 had the density similar to SBA-15 and KIT-6, a similar ratio of cobalt nitrate to SBA-16 was used. With the SBA-16 being a 3D mesoporous structure, it was expected to have spherical particles similar to that seen for KIT-6 replicated particles. Figure 5-4 (a) shows a low magnification TEM image of the ~200 nm spherical particles present, however they were not as common as they were for when using KIT-6, and instead there was larger particles of 300-400 nm with less of a curved edge, Figure 5-4 (b). Both of these type of particles gave a polycrystalline pattern and also had structural defects.

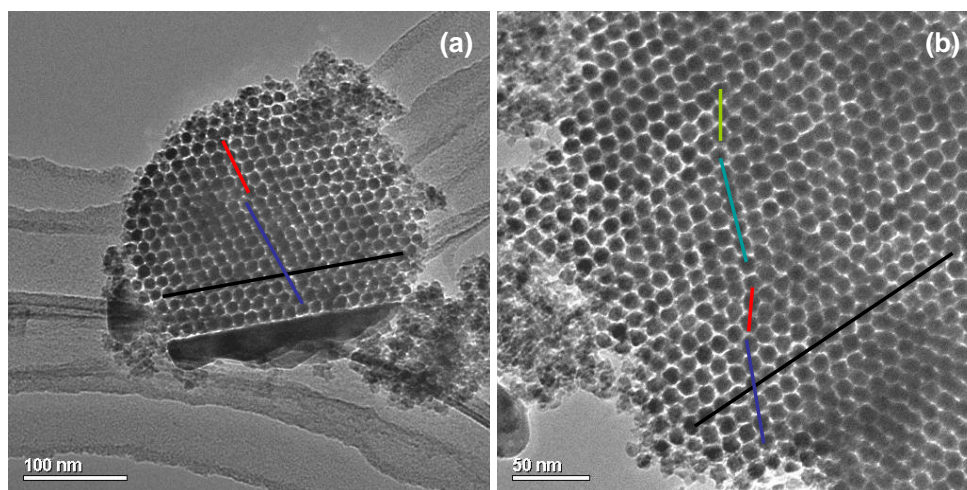


Figure 5-4. Low magnification TEM images of mesoporous cobalt oxide crystals templated by SBA-16. The black line indicates that there are no defects in one direction, whilst the varying coloured lines show different stacking faults.

The structure defects seen in the mesoporous crystals may be occurring after the template is removed. While face-centered cubic material commonly exhibit layered defects<sup>6</sup>, it is very rare in the case for body-centered cubic. If this defect was coming from the replication of the mesoporous structure, then it would be expected to be seen in images of the parental material. However, by looking at the [100] and [110] axis, Figure 5-5, of the parental SBA-16 does not reveal any such defect. Although the defects are not appearing in these zone axes, they could be exhibited in a different zone axis. This indicates that the faults could be occurring in the template in a different zone axis, which is more likely than forming after the template is removed.

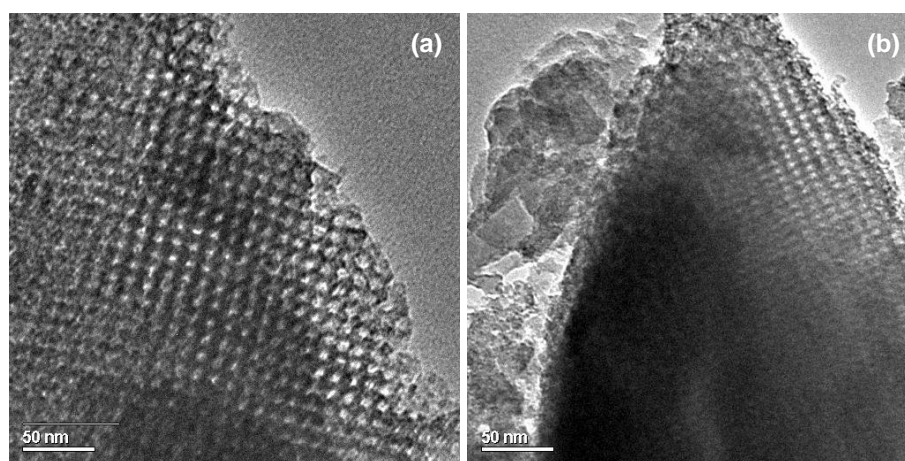


Figure 5-5. TEM images of mesoporous SBA-16 viewing down the (a) [100] and (b) [110] axes.

Due to the thickness of the crystals, high magnification imaging of these regions to see whether the defect was caused by change of crystal domain was unsuccessful. The crystals edge, where it is thinnest, tended to have small crystallites, making the atomic imaging difficult to show the different crystal domains. The fact that the cage structure, which has a highly open structure with regular connecting pores, does not form the single crystal nor a perfect replica of the parental material seems strange when compared to two-dimensional structures with random connecting pores that has perfect single crystallinity and mesoporous replication. Additionally, the spherical particles created by polycrystalline material show that it is not so much a factor of

the crystal growing from a single seed but is from the shape selectivity of the parental mesoporous material.

Considering that the particles do seem to have a defectless row of mesopores in one direction, the black lines in Figure 5-4, whilst the other directions have the defects, coloured lines, there appears to be a preferential growth direction within the mesopores. Since SBA-16 is made up of spherical cages connected by windows in a cubic arrangement, it could be assumed that crystal growth inside a perfect template should not have a preferred direction. This implies that there must be unseen defects in the parental material, possibly in the connecting windows rather than layered defects. However, this does not seem likely as the chance of the clear windows in the cubic system occurring in only one direction, as the black lines suggest in Figure 5-4, whilst the occurrence of the other windows being blocked would be very small.

A similar problem from the mesoporous cage structure, this time in the form of FDU-12, can be seen in the next section. Whilst cobalt oxide in SBA-16 just showed defects, iron oxide in FDU-12 resulted in the produced metal oxide being non-porous.

### 5.3 Non-porous metal oxides

#### *Iron Oxide in FDU-12*

Recently, nanostructured iron oxides, such as nanorods (SBA-15), thin films (SBA-16) and 3D mesoporous crystals (KIT-6), have been synthesised.<sup>7-9</sup> The mesoporous material, templated by KIT-6, was found to be near single crystal and also had an equivalent unit cell to rhombohedral iron oxide.<sup>9</sup> Iron nitrate was added to SBA-15 to see what temperature crystallisation occurred at. By running XRDs at 50 °C intervals, it was found that rhombohedral Fe<sub>2</sub>O<sub>3</sub>, with space group  $R\bar{3}c$  and lattice parameters  $a = 5.032$  and  $c = 13.733$  nm, was formed at

400 °C (JCPDS 890599).<sup>10</sup> Figure 5-6 is an XRD pattern for iron oxide in SBA-15 after the iron nitrate underwent decomposition at 400 °C for 5 h.

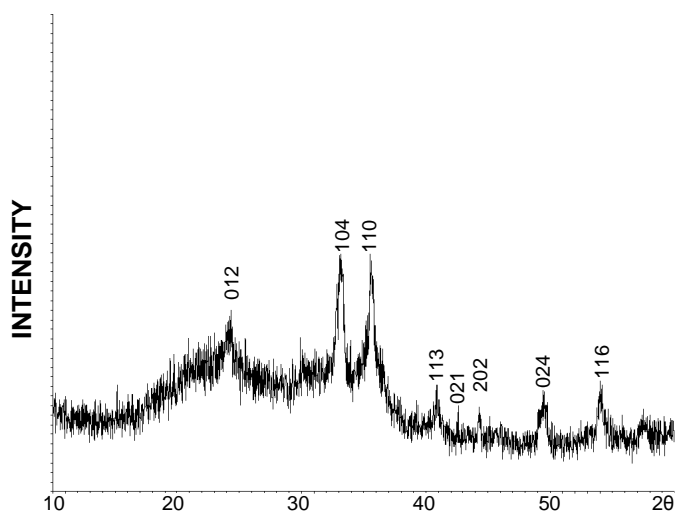


Figure 5-6. XRD pattern of iron oxide inside SBA-15 indexed to rhombohedral  $\text{Fe}_2\text{O}_3$  after the decomposition of iron nitrate at 400 °C.

Since nanorods and 3D mesoporous structures have already been synthesised, the cage structure of FDU-12 was chosen. If a PSC was created using this structure, it should display some interesting properties. The spherical cavities connected by windows cage structure is similar to SBA-16, however whilst SBA-16 has eight windows per cavity (corner sharing), FDU-12 has six (face sharing). After the template was removed after the crystallisation of  $\text{Fe}_2\text{O}_3$ , HRTEM imaging was carried out and displayed some disappointing results.

Some material appeared porous which required tilting to a principle zone axis. After tilting the sample though, it was discovered to be small particle clusters. Figure 5-7, shows a TEM image of these nanoparticle clusters. By looking at the edge of these crystals, it could be seen that these particles could have formed in the mesopores, due to their shape and size. The SAED of these clusters obviously gave a polycrystalline pattern.

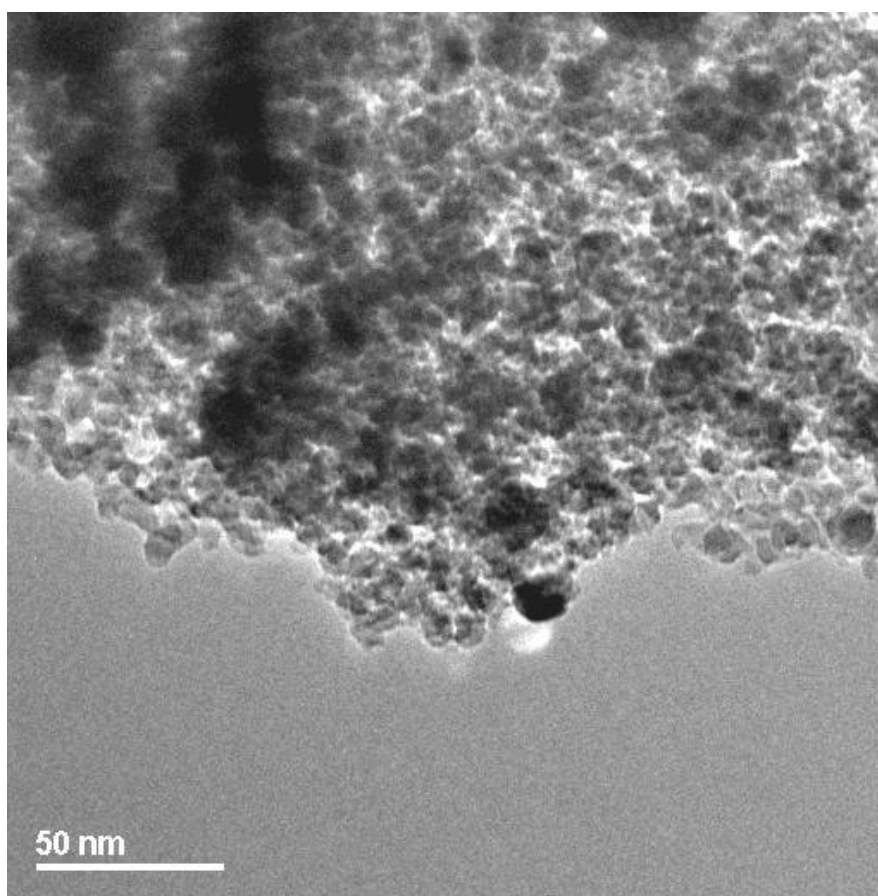


Figure 5-7. Low magnification TEM image of a cluster of nanoparticles of iron oxide.

There were some single crystal particles, although these were too big to have formed in a mesopore system. Figure 5-8 (a) shows a low magnification image of these particles with relatively uniform shape (spherical) and size (400-700 nm). The crystals also appeared to have areas of low density in the middle of the particles. The low density areas also appear to be spherical, almost like bubbles in the particles, and the particles are stable, and therefore the bubbles are not due to decomposition under the electron beam. These particles clustered together, and each of them was a single crystal. Figure 5-8 (b) is a high magnification HRTEM image of one of these single crystal particles. The particle was able to be indexed to rhombohedral iron oxide.

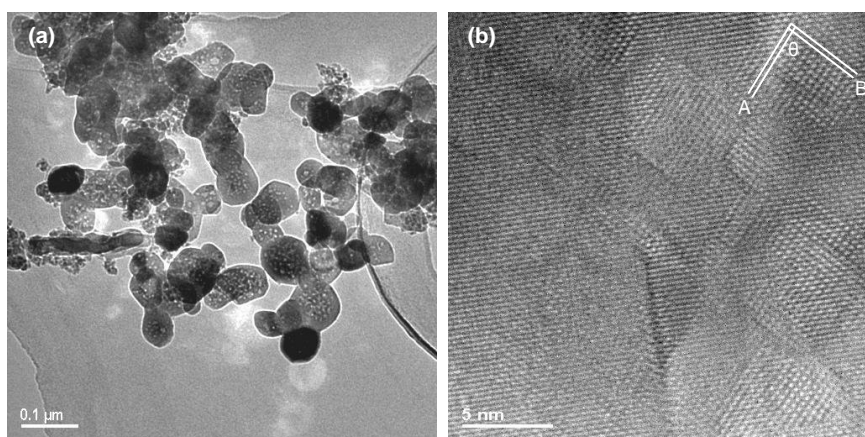


Figure 5-8. TEM images of non porous iron oxide. (a) Low magnification image showing the size and shape distribution of the particles. (b) High magnification HRTEM image of a single crystal particle indexed to rhombohedral  $\text{Fe}_2\text{O}_3$  with space group  $R\bar{3}c$  and lattice parameters  $a=5.032$  and  $c=13.733$  Å.  $A=(10\bar{1}\bar{2})$  and  $B=01\bar{1}\bar{2}$ ) with interplane angle  $\theta=86^\circ$  viewing down the  $[\bar{2}\bar{2}1]$  zone axis.

The large particles were probably formed in the bulk iron nitrate outside of the mesopores. The areas of low density could have resulted from the evolving of the gases in the decomposition step being trapped inside the crystal. Although this may not be the case, since there does not appear to be any defects in the crystal structure in these regions. High magnification images showed the single crystal was uniform throughout the whole particle.

Why cage structures have a problem remaining perfectly connected could be down to the open bridging pores. With rod-like channel structures, similar to SBA-15 and KIT-6, the connecting pores are micropores, whereas for the cage structures it is mesopores. When the sample forms a seed inside the rod-like mesopores and the precursor material migrates towards this, it will use the main channel for the migration and crystallisation. The crystallisation over the micropore, and forming the bridge will be relatively fast and will then lead to the neighbouring channel to start crystallisation. Additionally, since the micropores are random then the rate of crystallisation will mainly come from the rate of crystallisation within the rod-like channels. For the case of cage structures, the bridging mesopores are more regular and much larger than the

micropores. This means that the rate of crystallisation will not be just controlled by the larger cavities but also the bridging mesopores. If it is assumed that the smaller the pore, the greater the speed in crystallisation, then the rate of crystallisation of FDU-12 would be faster than say that of SBA-15. This would initially imply that the single crystal should form more readily in the FDU-12, however not when you take in the factor of the speed of migration of the precursor material.

When the migration of the precursor begins on seed formation, the speed will be dependent on the size and shape of the channel. For SBA-15, the speed of migration should be steady due to the relatively cylindrical pores. However, when the migration occurs in FDU-12, the speed of migration will be much faster for the bridging pores as opposed to the cavities. Although, the speed of migration could still be relatively fast, migration will slow down when filling a cavity and speed up when filling a bridging pore causing more or less a stop-start effect. The rate of migration may be faster than that from SBA-15, but the rate of crystallisation will probably be faster than the rate of migration, disallowing the full pore to be filled before the crystallisation occurs. For SBA-15, the rate of crystallisation will most likely be slower than the rate of migration, allowing enough time for the precursor material to fill the pore.

Whilst the constant flow of migration in the uniform channel could stop additional seed formation, the erratic flow of migration for the cage structure may not. Therefore, although the 3D-mesoporous structure is more open for cage structures, which should allow for a less hindered growth for the single crystal, than the rod-like channels, the windows are slowing the crystal growth down, due to letting a smaller amount of material to migrate constantly. If the migration of the material hinders the growth, then that would explain the small particle clusters found after the template is removed.

#### *Silver in SBA-15*

As mentioned before, the fact that PSCs have bulk size whilst retaining nanoproperties, should

make it useful in a whole host of properties. The project has been mainly looking at metal oxides, although since silver nitrate decomposes to silver metal, a pure metal PSC was tried. It has already been reported that it is possible to make a porous crystal by electrochemical methods and also by hydrogen reduction of ionic metal.<sup>11,12</sup> Both systems need rather exact conditions and is not as straight forward as heating in a furnace, which is far simpler.

In section 5.1, the synthesis of metal oxides in silica was described. The preparation of the silver was almost identical, with 0.33 g of silver nitrate being mixed in 8 g of ethanol together with 0.15 g of SBA-15. After stirring for 2 h, the ethanol was allowed to evaporate off at room temperature in a wide-bottomed petri dish. Once dry, the powder was decomposed in air in the furnace, increasing the heat from room temperature to 550 °C at a ramp rate of 1 °C/min.

After the silver nitrate was decomposed, XRD data was collected for the silver in SBA-15 and it was found to fit with the cubic silver unit cell with space group  $Fm\bar{3}m$  and lattice parameter  $a = 4.077 \text{ \AA}$  (JCPDS 870720).<sup>13</sup> The XRD, Figure 5-9, showed that the silver was in a pure phase, which would be expected as any silver oxide would automatically decompose due to the temperature in the furnace. The template was then removed for HRTEM characterisation.

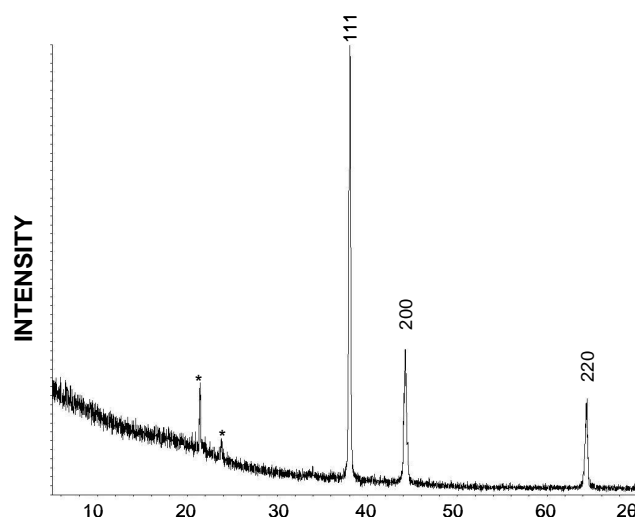


Figure 5-9. XRD pattern of silver in SBA-15 indexed to the face-centered cubic phase. The two peaks at 21° and 24°, marked with asterisks, are from the petroleum jelly used in adhering the sample to the XRD disk.

HRTEM revealed large silver particles that had obviously formed outside the mesopores of SBA-15. All of the particles were spherical in shape, although there was a wide range of sizes, ranging from 30-300 nm with some micrometer sized particles. Figure 5-10 shows some of these silver nanoparticles with a range of sizes. No other particles that resembled mesoporous material or nanorods were seen, indicating that the mesopores were not used in the decomposition.

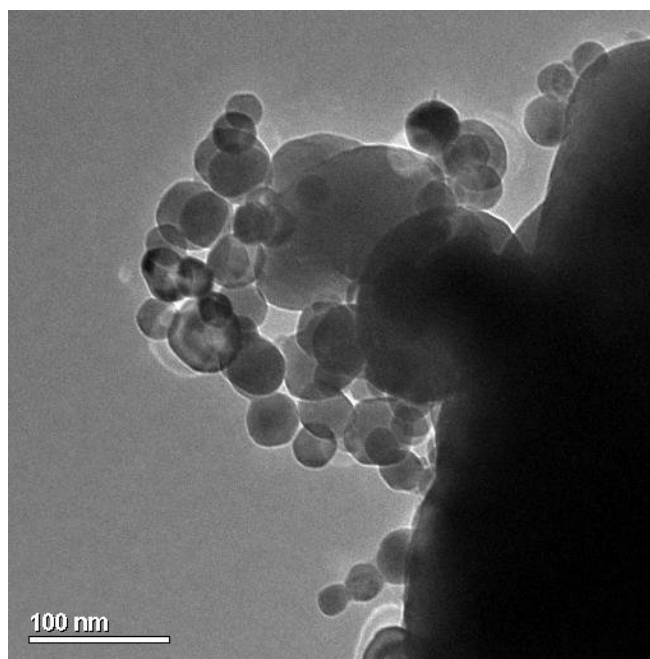


Figure 5-10. TEM image of spherical silver particles formed outside the mesoporous template, SBA-15.

This experiment does reveal some important information on when choosing a suitable precursor. It has been mentioned that the capillary condensation can occur either in the solution step or the melt step. The silver nitrate has a melting point of  $\sim 200$  °C and a decomposition point of  $\sim 400$  °C, so a melt step should occur before the decomposition.<sup>14</sup> For the solution step, the solubility of silver nitrate is poor and therefore not all of it will be dissolved in the ethanol. This would result in only a minimum amount of material entering in this step. When the silver nitrate then melts, most of the particles will be on the outside of the SBA-15. Capillary action will most likely be hindered, not so much by the quantity of material outside but, by the poor dispersity.

Since cobalt nitrate is very soluble, even when the ethanol evaporates off and the material is deposited on the outer surface of the mesopores, it has a wide dispersity and therefore capillary condensation can occur. In the case of silver nitrate, the large particles will melt and form globules of liquid. For the capillary action to occur, it needs to break the surface tension of the globules, which requires more heat.

Since it is known, from previous results in chapters 3 and 4, that the mesopores of the template can reduce the decomposition temperatures, it stands to reason that this may also be the case for the silver nitrate. Therefore the temperature difference between the melt and the decomposition temperature will be reduced. If the temperature for the melt to begin capillary condensation is higher than the decomposition temperature within the mesopores, then the material will start breaking down as soon as it enters the template. This could result in the blocking of the pore entrances. Additionally, since the nitrate will break down first to the oxide, which will decompose to the metal violently, as a result of the high temperature. This is due to the decomposition of the  $\text{AgNO}_3$  being  $\sim 400^\circ\text{C}$ , whilst the decomposition of the  $\text{Ag}_2\text{O}$  is only  $100^\circ\text{C}$ .<sup>14</sup> Even if the silver changes oxidation state from 1+ to 2+ when decomposed from the nitrate, and therefore forms  $\text{AgO}$ , the decomposition temperature is still only  $200^\circ\text{C}$ . The violent reaction of the silver oxide to silver would cause the evolution of gas and could propel the material out of the mesopore and into the bulk material. The silver particles could then act as seeds for the material to grow as bulk silver outside the mesopores.

Despite the relatively high melting point of the silver,<sup>14</sup> which made it a candidate as forming a pure metal porous single crystal by heating, it was hindered by the fact of the poor solubility of the nitrate precursor and the violent decomposition of the intermediate. This makes it understandable why more successful results have been obtained by electrodecomposition and hydrogen reduction.<sup>11,12</sup> It could still be possible to allow the silver nitrate into the pores by holding the temperature at the melting point. This could allow for more of the material to enter

the pores, however as mentioned before a higher temperature, rather than that of the melt, may be required to break the surface tension of the silver nitrate globules.

In summary, cobalt oxide was used in two more mesoporous templates. The resulting cobalt oxide was polycrystalline for both the SBA-15 fibres and SBA-16, however the resulting material was mesoporous. The cobalt oxide fibres were observed as larger crystals than the material produced from normal SBA-15 and possibilities on why the material was polycrystalline was discussed. The cobalt oxide, templated by SBA-16, was found to have defects and not perfectly replicate the pore structure of the parental material, despite SBA-16 having a more open structure than SBA-15 and KIT-6. Another cage structure, FDU-12, was used for the synthesis of porous iron oxide crystals. This was not successful, leading instead to clusters of nanoparticles and large non porous single crystals. The effects of the mesoporous windows in the cage structure on the migration of the precursor material were also discussed. Finally, silver nitrate was decomposed in SBA-15, however due to the poor solubility of the nitrate and the violent decomposition to the metal, only bulk material was formed.

The final research chapter looks at the HRTEM work on other nanomaterials. The HRTEM work was in collaborations with other universities, where the material was synthesised. The chapter includes nanoparticles in mesoporous material and silicon nanowires grown in a 2-dimensional porous template.

## References

- [1] B.Z. Tian, X.Y. Liu, H.F. Yang, S.H. Xie, C.Z. Yu, B. Tu and D.Y. Zhao, *Adv. Mater.*, 2003, **15**, 1370
- [2] K.K. Zhu, B. Yue, W.Z. Zhou and H.Y. He, *Chem. Commun.*, 2003, 98
- [3] G. Will, N. Masciocchi, W. Parrish and M. Hart, *J. Appl. Crystallogr.*, 1987, **20**, 394
- [4] P.D. Yang, D.Y. Zhao, D.I. Margolese, B.F. Chmelka and G.D. Stucky, *Chem. Mater.*, 1999, **11**, 2813
- [5] Y. Sakamoto, M. Kaneda, O. Terasaki, D.Y. Zhao, J.M. Kim, G.D. Stucky, H.J. Shim and R. Ryoo, *Nature*, 2000, 408, 449
- [6] W.Z. Zhou, H.M.A. Hunter, P. A. Wright, Q.F. Ge and J.M. Thomas, *J. Phys. Chem. B*, 1998, **102**, 6933
- [7] F. Jiao, B. Yue, K.K. Zhu, D.Y. Zhao and H.Y. He, *Chem. Lett.*, 2003, **32**, 770
- [8] K.Y. Shi, L.M. Peng, Q. Chen, R.H. Wang and W.Z. Zhou, *Micropor. Mesopor. Mater.*, 2005, **83**, 219
- [9] F. Jiao, A. Harrison, J.C. Jumas, A.V. Chadwick, W. Kockelmann and P.G. Bruce, *J. Am. Chem. Soc.*, 2006, **128**, 5468
- [10] V.A. Sadykov, L.A. Isupova, S.V. Tsybulya, S.V. Cherepanova, G.S. Litvak, E.B. Burgina, G.N. Kustova, V.N. Kolomiichuk, V.P. Ianov, E.A. Paukshtis, A.V. Golovin and E.G. Avvakumov, *J. Solid State Chem.*, 1996, **123**, 191
- [11] T. Gabriel, I.S. Nandhakumar and G.S. Attard, *Electrochem. Commun.*, 2002, **4**, 610
- [12] Y.J. Han, J.M. Kim and G.D. Stucky, *Chem. Mater.*, 2000, **12**, 2068
- [13] G. Becherer and R. Ifland, *Naturwissenschaften*, 1954, **41**, 471
- [14] *CRC Handbook of Chemistry and Physics 8<sup>4</sup>th Ed.*

## 6. HRTEM of Other Nanomaterials

In addition to the work on mesoporous solids, the HRTEM has been used to investigate other nanomaterials. Three different areas of research are presented in this chapter. The first two sections are closely related to the research in the previous chapter, with the first being nanoparticles in mesoporous silica and the second being nanowires templated from porous anodised aluminium oxide (AAO). The third section looks at trifunctional nanospheres.

### 6.1 Ruthenium oxide nanoparticles in mesoporous silica

The use of mesoporous silica as catalytic supports is now a widely common research field, from functional groups to metal incorporation.<sup>1,2</sup> In this section, ruthenium oxide nanoparticles in mesoporous silica were investigated by HRTEM.<sup>3</sup> The material was synthesised and used in catalytic experiments by Professor Duncan Bruce's group in Exeter University, UK.

#### *Synthesis of ruthenium containing mesoporous silica<sup>3</sup>*

A ruthenium surfactant, tris(bipyridine) ruthenium (II) complex,<sup>4</sup> was mixed with water in a 1:1 weight ratio. Once a homogeneous mixture was obtained, the silica source, tetramethoxy orthosilicate (TMOS), was added, along with acidified methanol, to the mixture. The mixture then underwent condensation at 40 °C for 48 h, allowing the methanol to be gradually evaporated. The resulting powder was calcined at 400 °C, at a ramp rate of 3 °C/min, for 5 h. Ruthenium oxide particles were now dispersed in the mesoporous silica support.

#### *TEM characterisation*

The main areas of investigation for the material were the mesoporosity and the distribution of location and size of ruthenium oxide particles. A very low electron beam spot size was required

as the material was very unstable under the electron beam. Usually, mesoporous silica, formed in the traditional manner (i.e. SBA-15), is very stable under the beam. The reason why this material may be less stable could be the nature of the maturation process.

Preliminary TEM results revealed that most of the silica was mesoporous and had a hexagonal structure. The TEM evidence of the mesoporous silica fitted well with the XRD data presented in the paper.<sup>3</sup> Figure 6-1 (a) shows the side on view of the mesoporous silica, looking down the  $[01\bar{1}0]$  direction. The interfringe distance was measured to be 36 Å, which corresponded to the d-spacing of the  $\{10\}$  atomic plane. Due to the ordered image contrast pattern, the ruthenium oxide nanoparticles within the pores, as only a small amount are present, are concealed although some can be seen, as indicated by the white arrows.

When there is an increase in ruthenium oxide particles, a rosary-like contrast pattern is observed in the TEM image, Figure 6-1 (b). This rosary pattern occurs when the nanoparticles become ordered or partially ordered in the mesopores.<sup>5</sup> This further supports that there is only a very low loading in the mesopores in Figure 6-1 (a) due to the absence of this pattern. Even though disordered metal nanoparticles can usually be seen in mesopores, it is only when the wall thickness is relatively thin.<sup>6</sup> For the mesoporous material with the ruthenium oxide nanoparticles; the wall thickness is ~15 Å, as opposed to MCM-41 which is ~6 Å.

Even when the rosary pattern was seen, which tended to be the more common of the two, it was difficult to measure the ruthenium oxide particle size when the particles were in the mesopores. The electron beam was increased in spot size to destroy the mesopores, so that the particles could be measured. Figure 6-1 (c) is a TEM image of the mesoporous material, seen in Figure 6-1 (b), after the collapse of the mesopores by the electron beam. It can be seen that the level of nanoparticles present is rather high. By measuring over 700 particles, a range of size, 15-40 Å, was obtained, with the average particle size being 26 Å, Figure 6-1 (d).

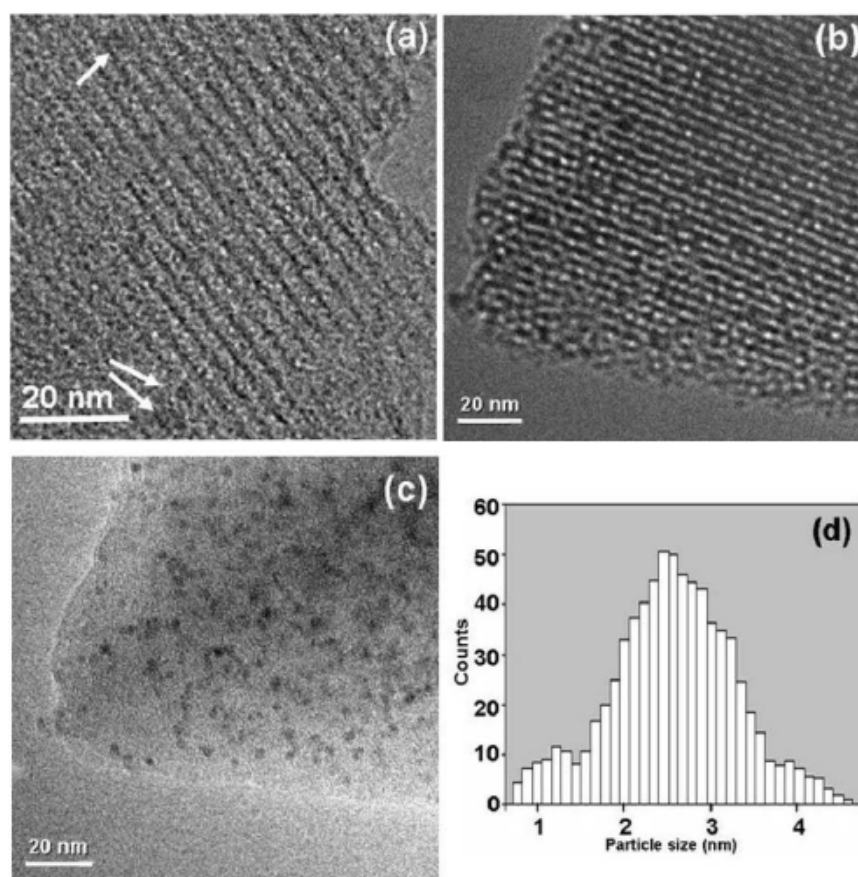


Figure 6-1. (a) TEM image of the one dimensional straight mesopores corresponding to the  $[01\bar{1}0]$  zone axis of the hexagonal phase of silica. The white arrows indicate some large ruthenium oxide nanoparticles. (b) TEM image of the more typical particles in the sample, viewing down the same direction as (a) but exhibiting a rosary-like pattern due to high loading of nanoparticles. (c) TEM image of the particle in (b) after the mesostructure was destroyed by the electron beam. (d) Size distribution graph for ruthenium oxide nanoparticles, from the measurement of >700 particles.

The size of the average nanoparticles is possibly larger than the pores, as the interfringe distance is  $36 \text{ \AA}$  and the wall thickness is  $\sim 15 \text{ \AA}$ . However, the larger particle size can be attributed to when the electron beam destroyed the template; it caused a sintering effect of the nanoparticles and therefore appeared larger than if they could have been accurately measured inside the original pores.

EDX was also carried out to determine the weight percentage of ruthenium in the sample. Figure 6-2 is an EDX spectrum showing only a small peak for ruthenium when compared to silica, indicating good dispersity within the template. The EDX was taken for 10 particles that exhibited the rosary pattern and revealed a percentage of  $7.6 \pm 1.7$  wt % of ruthenium. This is in good agreement from the data obtained from ICP-MS and the theoretical value (6.9 wt %).

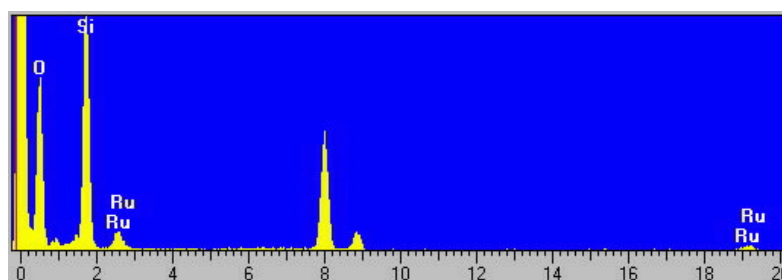


Figure 6-2. EDX spectrum of the mesoporous silica containing ruthenium oxide nanoparticles.

## 6.2 Silicon nanowires templated by AAO

Over the past decade, silicon nanowires have been a well researched area, ranging from methods of synthesis to the growth mechanism.<sup>7-9</sup> While most of the nanowires tended to be poorly crystalline and had disordered growth,<sup>7,8</sup> the use of a template can reverse these problems.<sup>10</sup> The following TEM work was carried out on material synthesised by Professor Jian Sha's group in Zhejiang University, China. There were two types of silicon nanowires produced. The first nanowires have a crystalline silicon core with defects covered in a large coating of 'sticky' amorphous silica and the second set were thinner and without the thick silica coating.

### *Synthesis of AAO template*<sup>11</sup>

An aluminium plate, 1 mm in thickness, was placed under vacuum and annealed for 2 h at 500 °C. The plate was then washed with acetone, dried and put into an oxalic acid solution at 16 °C at a constant voltage of 42 V for 3 h for anodisation. The disordered structure from the top layer was removed by using phosphoric acid- chromic acid mix before anodising for a further 10 h. The excess aluminium was then removed from the AAO using a copper chloride solution, and the alumina was further treated with phosphoric acid at 30 °C for 90 min.

### *Synthesis of silicon nanowires*

The only difference between the two different nanowires produced was the ratio of the mixture of argon, hydrogen and silane gas, all the other synthetic steps were the same. The AAO, from the section above, was sputtered with gold on one side and placed in a tube furnace. The pressure of the furnace chamber was pumped down to 20 Pa and heated to 500 °C. A mixture of the gases, argon, hydrogen and silane, in the ratio of 10:2:1 or 10:20:15, was allowed to flow into the chamber. The temperature, 500 °C, and pressure, 1400 Pa, was kept constant for the 6 h of deposition. The furnace was returned to room temperature and pressure and the AAO substrate, now with the nanowires, was placed in a desiccator for storage.

### *HRTEM characterisation*

Before the silicon nanowires were removed from the substrate, with the use of a razorblade, SEM was used to show the nanoforest of wires. Figure 6-3 has two SEM images of the nanowires, looking along the edge of the substrate and down onto the face of the substrate.

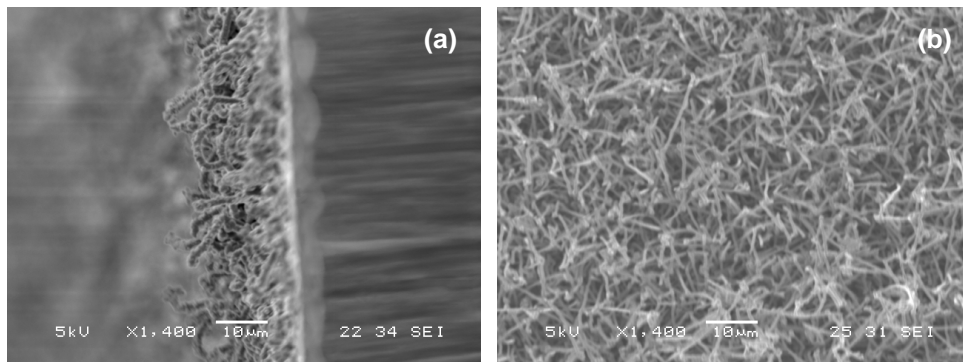


Figure 6-3. SEM image of silicon nanowires on the substrate, viewing (a) along the edge and (b) down onto the face.

Starting by looking at the nanowires made with the argon, hydrogen and silane ratio of 10:2:1, it was found that the nanowires had a crystalline core covered by a large amount of amorphous material. The crystalline core had an average diameter of 50-70 nm, although with the amorphous coating, the diameter was nearer 200 nm. By tilting the wire to obtain a symmetrical diffraction pattern, the crystalline core became visible. Dark field imaging was used to help distinguish between the crystalline wire and the amorphous coating. Figure 6-4 shows the tip of a nanowire; the white arrow indicates the crystalline centre in the bright field and dark field image, (a) and (b).

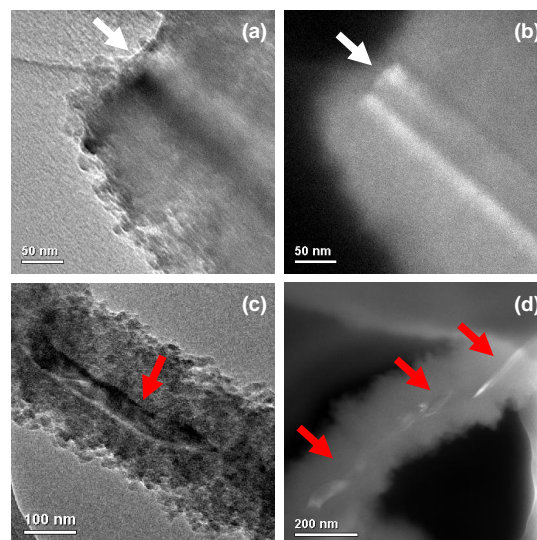


Figure 6-4. TEM image of the tip of a nanowire indicated by the white arrow in (a) bright field and (b) dark field. (c-d) TEM images of the 'broken' nanowire effect in (c) bright field and (d) dark field.

If a wire had not been tilted to a two-dimensional diffraction pattern, the image looks like the nanowire is broken. Figure 6-4 (c) and (d) shows this broken nanowire effect in bright and dark field respectively. The nanowire, however, is not broken as tilting the sample further can make the whole nanowire to appear. This ‘broken nanowire’ effect is mainly due to the low diffraction contrast of the image when the electron beam is not parallel to a principal crystal orientation of silicon.

By looking at the HRTEM of a nanowire, after a good 2D SAED pattern had been obtained, the wire was found to be silicon in the fcc phase. The cubic silicon has a space group of  $F\bar{4}3m$  with lattice parameter  $a = 5.392$  (JCPDS 800018).<sup>12</sup> All the nanowires grow in the  $[\bar{2}11]$  direction, this growth phenomenon has been well reported in literature.<sup>11, 13</sup> Figure 6-5 shows the edge of the silicon nanowire and the amorphous coating. Small crystallites were seen in the

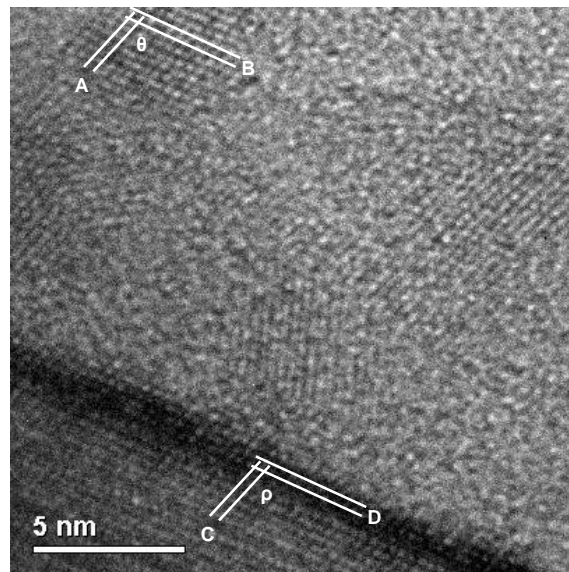


Figure 6-5. HRTEM image of the silicon nanowire with the amorphous coating. The silicon crystallites can be indexed to the same cubic silicon as the nanowire. A and C are indexed to the  $(1\bar{1}\bar{1})$  plane, B and D are indexed to the  $(111)$  plane and angles  $\theta$  and  $\rho$  are both  $109.5^\circ$ . The silicon crystallite and nanowire are both viewed down the  $[0\bar{1}1]$  zone axis.

amorphous coating, these were also indexed to cubic silicon. It is believed that when the silane gas meets a surface, it becomes amorphous silicon, small particles of silicon could form in the silica due to the temperature.

By investigating the diffraction patterns, it was found that most of these nanowires had defects, with the most common being twin defects. Twin defects are relatively common in silicon nanowires and have been reported in literature, with some research groups actually removing the defects by further treatment.<sup>8</sup> The diffraction pattern can be seen in Figure 6-6 (a), the principle growth direction of the nanowire,  $[\bar{2}11]$ , remains the same and the index numbers that are in white are the diffraction spots the twins have in common. The other indexing is in blue and purple, dependent on which domain it belongs to. Figure 6-6 (b) is a diagram separating out the diffraction spots, to show how the individual patterns for each twin domain come together to form the twin defect diffraction pattern.

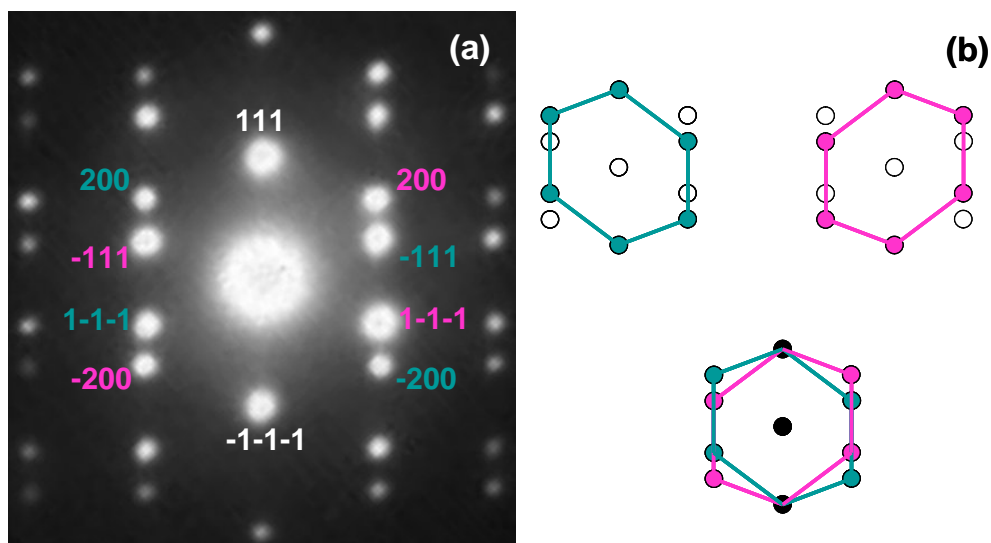


Figure 6-6. Twin defect (a) diffraction pattern with indexing of each twin and the (b) corresponding diagram of the individual patterns viewed down the  $[0\bar{1}1]$  zone axis.

The twin defects can be observed in the HRTEM image in Figure 6-7. The white line indicates the change in angle of the atomic plane and it can be seen that the growth direction of

the nanowire remains the same as  $[\bar{2}11]$ , shown by the arrow. The angle of the twin defect is  $141^\circ$ , which is twice the angle between  $(111)$  and  $(\bar{1}11)$  in a face centered cubic pattern viewed down the  $[0\bar{1}1]$  zone axis.

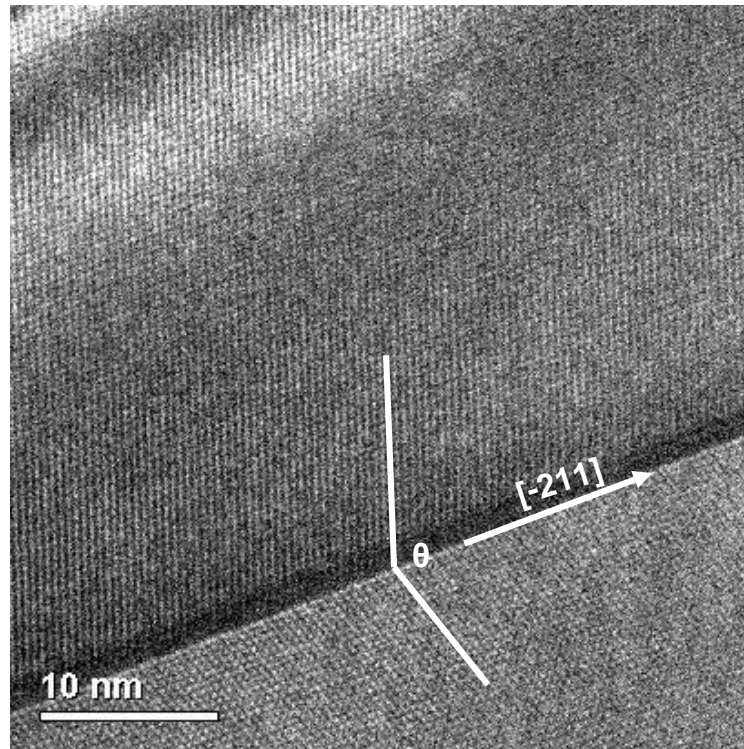


Figure 6-7. HRTEM image of a silicon nanowire exhibiting a twin defect. The white arrow reveals the  $[\bar{2}11]$  growth direction of the wire and the white line shows the change in crystal orientation, with the angle  $\theta$  as  $141^\circ$ .

Although the twin defects were the most common, some other defects were seen. Figure 6-8 shows two HRTEM images of a nanowire with rather complex defects; however the  $[\bar{2}11]$  growth direction is still retained. Figure 6-8 (a) reveals how this stacking fault has a regular periodicity across the wire, with the SAED pattern (inset) showing the equally complex diffraction pattern resulting from this superstructure. The periodicity of  $(4 \text{ or } 5):2:1:2:(4 \text{ or } 5)$  atomic layers, is almost constant through the width of the wire, with the twin defects seen on either side of the nanowire. By increasing the magnification on the white boxed area, the change in crystal

orientation can be seen (Figure 6-8 (b)). Whereas the twinning angle is  $141^\circ$ , the other defects only change the crystal orientation by a much smaller angle, which can be seen by the white line C. The d-spacings A and B confirm the nanowire to be still cubic silicon as before.

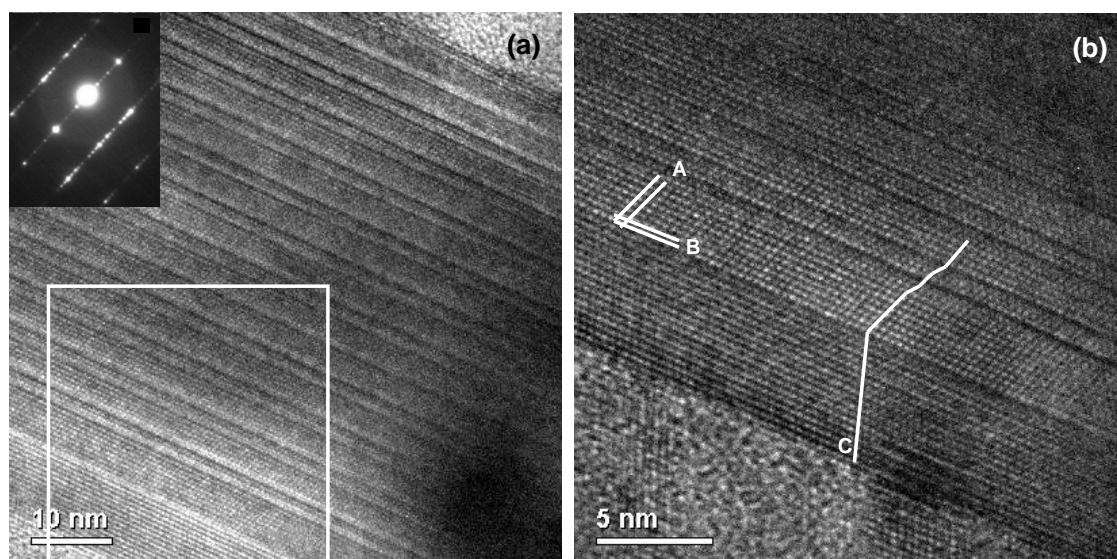


Figure 6-8. HRTEM images of a silicon nanowire with stacking faults. (a) The faults have a periodicity of  $4/5:2:1:2:4/5$  atomic layers resulting in an SAED pattern with superstructure (inset). (b) Higher magnification image of the white boxed region from (a) with the line C showing the change in crystal orientation.  $A=(\bar{1}11)$  and  $B=(111)$  of fcc silicon.

The nanowires made with the argon, hydrogen and silane ratio of 10:20:15, were less rigid than the previous nanowires. The diameter of the wires was only 30-40 nm and they only had a 10 nm amorphous coating. Figure 6-9 (a) is a TEM image of the nanowires clustered together resembling spaghetti. The interweaving nature of the nanowires made obtaining an SAED pattern difficult, however as there was so many nanowires, it was possible to obtain good orientation of the crystal by searching. Figure 6-9 (b) shows an HRTEM image of a nanowire's atomic structure; once again it is indexed to cubic silica and has a  $[\bar{2}11]$  growth direction.

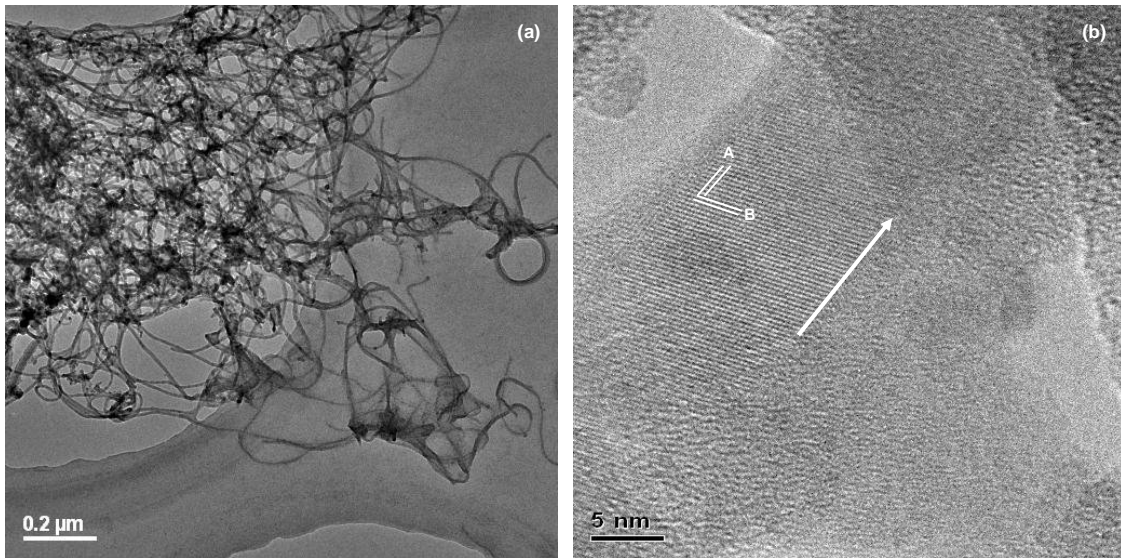


Figure 6-9. (a) TEM image of a cluster of silicon nanowires resembling spaghetti and (b) HRTEM image of a nanowire indexed to cubic silica with  $A=(111)$  and  $B=(\bar{1}11)$  viewing down the  $[0\bar{1}1]$  zone axis. The growth direction of  $[\bar{2}11]$  is indicated by the white arrow.

As mentioned in the synthesis procedure, the AAO is sputtered with gold, this catalyses the growth of the nanowire. The silicon from the silane gas dissolves in the liquid gold interface, once it becomes saturated, the silicon wire will grow. As the silicon grows, there is a gold nanoparticle on top, and silicon will continue to dissolve in the gold and grow the wire. This is referred to as the vapour-liquid-solid growth. Figure 6-10 (a) is a TEM image with gold particles, indicated by the white arrows, attached to the tip of the nanowires. The gold particles are roughly the same diameter as the nanowires. For the previously mentioned silicon nanowires, the gold was not seen. The gold for those nanowires would have had to have been twice the diameter, and therefore much easier to be removed from the tip of the nanowire. However, there was some evidence of branching from the nanowire, which is seen in Figure 6-10 (b). Whilst the growth of the wire is once again along the  $[\bar{2}11]$  axis, the red arrow, which is parallel to the plane marked

A, the growth of the branch appears to be  $[211]$ , parallel to the B plane. Additionally, the angle between the  $[\bar{2}11]$  and  $[211]$  axes is  $109.5^\circ$ , the same angle between plane A and plane B.

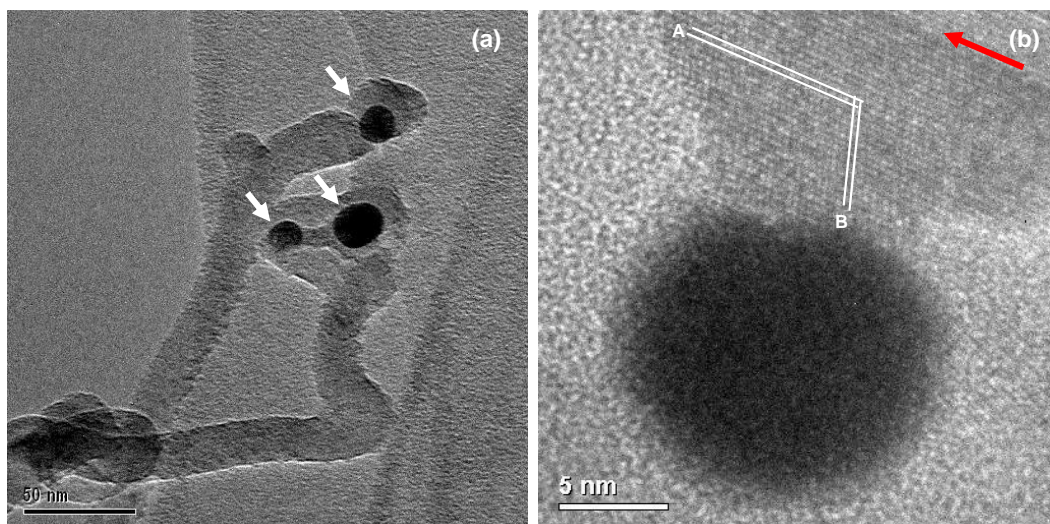


Figure 6-10. (a) TEM image showing gold nanoparticles, as indicated by the white arrows, at the tip of the nanowires. (b) HRTEM image of a gold nanoparticle creating a branch from a nanowire. The direction of growth for the nanowire is  $[\bar{2}11]$ , parallel to plane A, which is  $(111)$ , whereas the direction of growth for the branch is  $[211]$ , parallel to plane B, which is  $(1\bar{1}\bar{1})$ .

### 6.3 Tri-functional nanospheres

Although the material does not involve ordered mesoporous material, as the final product or as a template, it is worth mentioning on the huge advantage that nanomaterial can have in biological applications. This material can be used to target cancer cells due to the surface groups of the polymers, they are also trackable and magnetically manipulatable by the nanoparticles inside the spheres. This material was synthesised and tested with cancer cells by Professor Daiwen Pang's group at Wuhan University, China. The TEM technique was used to investigate the dispersity of the nanoparticles in the nanospheres and characterisation of these nanoparticles.

### *Synthesis of the Trifunctional nanospheres (TFNS)*<sup>14</sup>

The CdSe/ZnS quantum dots (QDs) were prepared by first making the CdSe quantum dots according to literature.<sup>15</sup> Hexamethyldisilathiane ((TMS)<sub>2</sub>S) and zinc acetate (Zn(ac)<sub>2</sub>) were then added dropwise to a CdSe solution at a constant temperature of 200 °C. The CdSe/ZnS QDs were dispersed in hexane until use.

Iron oxide nanoparticles were prepared, using a modified method from literature,<sup>16</sup> by reacting ferric acetylacetonate, HDA and oleic acid. This resulted in  $\gamma$ -Fe<sub>2</sub>O<sub>3</sub>, possibly due to the reaction being carried out in air. The nanoparticle size was 5-20 nm for  $\gamma$ -Fe<sub>2</sub>O<sub>3</sub>, whereas CdSe/ZnS particle size was 3-6 nm. Like before, the  $\gamma$ -Fe<sub>2</sub>O<sub>3</sub> was dispersed in hexane until use.

The nanospheres were synthesised using a modified emulsifier free polymerisation technique for styrene (St) and acrylamide (Aam) in an aqueous solution.<sup>17</sup> The St-Aam was hydrothermally treated with hydrazine, forming H<sub>2</sub>N-St-Aam, which were then swelled in a chloroform/butanol solvent (5:95 v/v). During the swelling, the CdSe/ZnS QDs and the  $\gamma$ -Fe<sub>2</sub>O<sub>3</sub> were added creating the bifunctional nanospheres. The nanospheres were then washed with butanol three times by ultrasonication and centrifuging. The final function was added by modifying the surface of the nanosphere with folic acid. Additionally, the external surface group can be easily changed to target different cancer cells.<sup>18</sup>

### *HRTEM characterisation*

TEM imaging revealed that no nanoparticles were found outside the mesopores. This implied that any nanoparticles that were not embedded were removed by the washing step. The nanospheres were of uniform size, with clean surfaces and nanoparticles were seen in the inside. Figure 6-11 is a TEM image of a nanosphere showing the uniform size of ~200 nm.

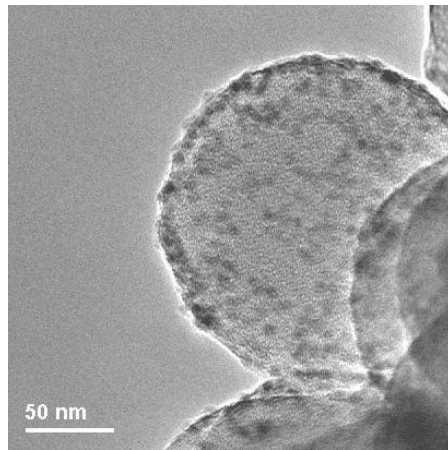


Figure 6-11. TEM image of a nanosphere containing the nanoparticles.

By running EDX on the nanospheres, the presence of the elements from the nanoparticles was revealed. By selecting a lone nanosphere, the edge of sphere was compared to the centre and was found that the atomic percentage of the nanoparticle elements was the same across the sphere. Additionally, the range of presence of nanoparticles in each sphere was very narrow, confirming good dispersity. Figure 6-12 is an image of a nanosphere and the corresponding EDX spectrum. The elements from the nanoparticles are coloured red.

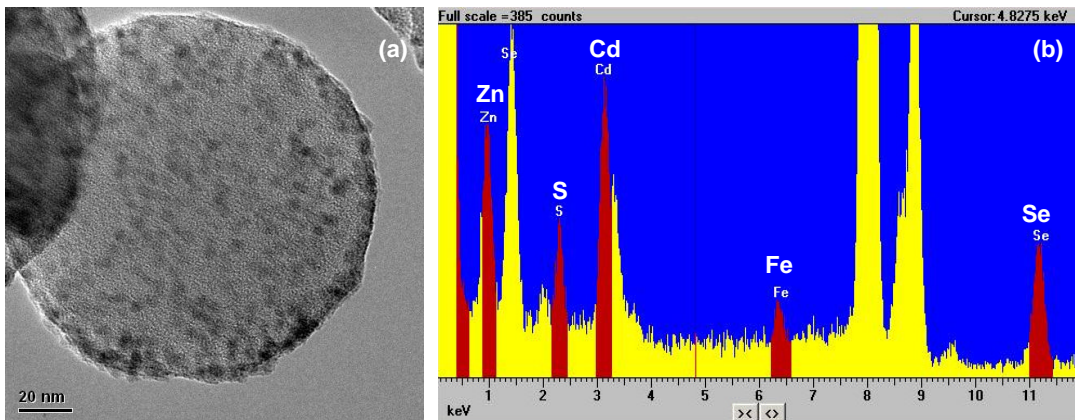


Figure 6-12. (a) TEM image of a nanosphere and the corresponding EDX spectrum. The spectrum reveals, in red, the presence of CdSe/ZnS and  $\text{Fe}_2\text{O}_3$  particles.

To further support that the nanoparticles of CdSe/ZnS, required for the photoluminescent properties so the nanospheres could be tracked, and the  $\gamma$ -Fe<sub>2</sub>O<sub>3</sub>, allowing for the nanospheres to be moved by a magnet, were characterised using HRTEM. The HRTEM was able to confirm that both nanoparticles were present in the nanosphere. Figure 6-13 (a, b) are HRTEM images of CdSe/ZnS, determined by their d-spacings, whereas (c, d) are images of the  $\gamma$ -Fe<sub>2</sub>O<sub>3</sub>.  $\gamma$ -Fe<sub>2</sub>O<sub>3</sub> was in the cubic form with space group  $P4_232$  and lattice parameter  $a = 8.35 \text{ \AA}$  (JCPDS 240081).<sup>19</sup>

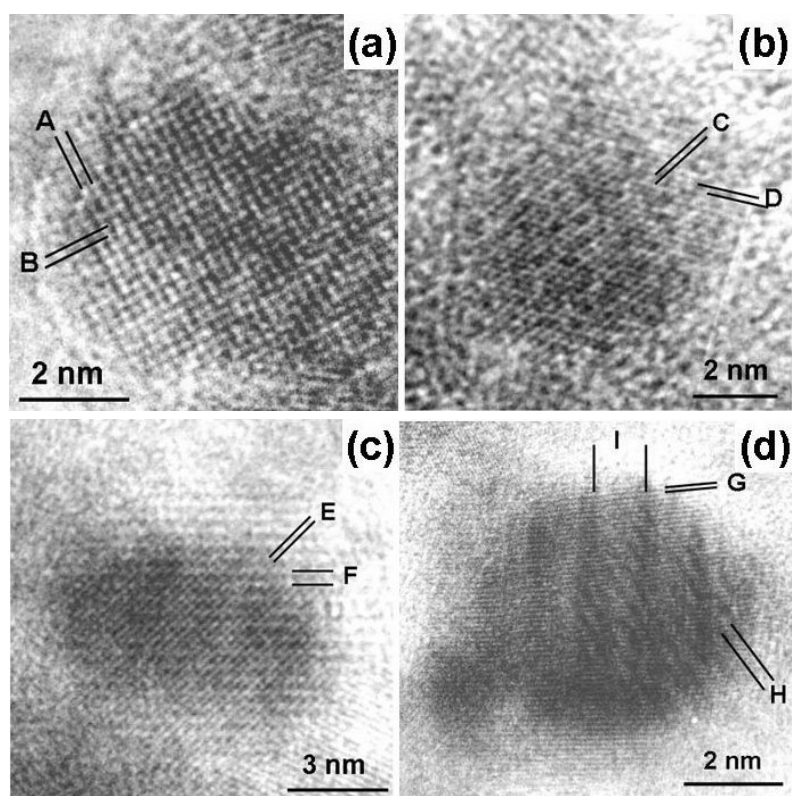


Figure 6-13. HRTEM images of CdSe/ZnS and  $\gamma$ -Fe<sub>2</sub>O<sub>3</sub> nanoparticles. (a) CdSe/ZnS QD;  $A = (0\bar{1}11)$ ,  $d = 0.33 \text{ nm}$ ;  $B = (10\bar{1}2)$ ,  $d = 0.25 \text{ nm}$ . The interplane angle is  $88^\circ$ . (b) CdSe/ZnS QD;  $C = (102)$ ,  $d = 0.25 \text{ nm}$ ;  $D = (2\bar{1}0)$ ,  $d = 0.21 \text{ nm}$ . The interplane angle is  $54^\circ$ . (c) Two particles overlapping each other. The atomic planes of E of the small crystallite can be indexed as CdSe (111) with  $d = 0.21 \text{ nm}$  and F of the large particle indexed as cubic  $\gamma$ -Fe<sub>2</sub>O<sub>3</sub> (200) with  $d = 0.41 \text{ nm}$ . (d) A nanoparticle of  $\gamma$ -Fe<sub>2</sub>O<sub>3</sub> with the fringes G indexed to (222) with  $d = 0.24 \text{ nm}$ . The superlattices present are marked by H ( $d = 0.76 \text{ nm}$ ) and I ( $d = 2.71 \text{ nm}$ ).

CdSe has a hexagonal space group  $P6_3mc$  with lattice parameters  $a = 4.299$  and  $c = 7.010$  Å (JCPDS 772307), and ZnS also has the same space group with similar lattice parameters  $a = 3.836$  and  $c = 6.277$  Å (JCPDS 751547).<sup>20,21</sup>

For Figure 6-13 (a, b), the core shell structure can not be seen for the CdSe/ZnS. The d-spacings are indexed to the CdSe crystal structure as that is the core structure, since the CdSe QDs were synthesised first. The shell of ZnS, is probably only a few atomic layers and due to the fact of lattice relaxation of the layers and that both CdSe and ZnS has the same wurtzite structure, it can be understood why the core shell can not be seen. Additionally, no separate particles of ZnS were seen in the sample, so most definitely, since both elements were present in the EDX spectrum, it is solely part of the core shell structure.

In summary, HRTEM work has been carried out in collaboration with several universities. The TEM has been used to investigate size distribution and the locational distribution of ruthenium oxide nanoparticles inside a mesoporous template. HRTEM of silicon nanowires has investigated the growth mechanism and defects of silicon nanowires using a non silica template, AAO. Finally, the HRTEM has been used to determine the presence of different types of nanoparticles in polymer nanospheres.

## References

- [1] H.H.P. Yiu, P.A. Wright and N.P. Botting, *J. Mol. Catal. B Enzym.*, 2001, **15**, 81
- [2] P.T. Tanev, M. Chibwe and T.J. Pinnavaia, *Nature*, 1994, **368**, 321
- [3] N.C. King, C. Dickinson, W.Z. Zhou and D.W. Bruce, *Dalton Trans.*, 2005, **6**, 1027
- [4] H.B. Jervis, M.E. Raimondi, R. Raja, T. Maschmeyer, J.M. Sneddon and D.W. Bruce, *Chem. Commun.*, 1999, 2031
- [5] W.Z. Zhou, J.M. Thomas, D.S. Shephard, B.F.G. Johnson, D. Ozkaya, T. Maschmeyer, R.G. Bell and Q. Ge, *Science*, 1998, **280**, 705
- [6] D.S. Shephard, T. Maschmeyer, B.F.G. Johnson, J.M. Thomas, G. Sankar, D. Ozkaya, W.Z. Zhou, R.D. Oldroyd and R.G. Bell, *Angew. Chem.*, 1997, **36**, 2242
- [7] W.S. Shi, H.Y. Peng, Y.F. Zheng, N. Wang, N.G. Shang, Z.W. pan, C.S. Lee and S.T. Lee, *Adv. Mater.*, 2000, **12**, 1343
- [8] Y.H. Tang, Y.F. Zheng, C.S. Lee and S.T. Lee, *Chem. Phys. Lett.*, 2000, **328**, 346
- [9] Y.J. Zhang, Q. Zhang, N.L. Wang, Y.J. Yan, H.H. Zhou and J. Zhu, *J. Cryst. Growth*, 2001, **226**, 185
- [10] J.J. Niu, J. Sha, X.Y. Ma, J. Xu and D. Yang, *Chem. Phys. Lett.*, 2003, **367**, 528
- [11] H. Zhang, X.Y. Ma, J. Xu, J.J. Niu, J. Sha and D.R. Yang, *J. Cryst. Growth*, 2002, **246**, 108
- [12] C.Y. Yeh, Z.W. Lu, S. Froyen and A. Zunger, *Phys. Rev. B*, 1992, **46**, 10086
- [13] A.M. Morales and C.M. Lieber, *Science*, 1998, **279**, 208
- [14] H.Y. Xie, C. Zuo, Y. Liu, Z.L. Zhang, D.W. Pang, X.L. Li, J.P. Gong, C. Dickinson and W.Z. Zhou, *Small*, 2005, **1**, 506
- [15] L.H. Qu and X.G. Peng, *J. Am. Chem. Soc.*, 2002, **124**, 2049
- [16] S. Sun and H. Zeng, *J. Am. Chem. Soc.*, 2002, **124**, 8204
- [17] X. Zhao, Y. Liu and H. Hui, *J. Med. Coll. PLA*, 1997, **12**, 62

- [18] H.Y. Xie, M. Xie, Z.L. Zhang, Y.M. Long, X. Liu, M.L. Tang, D.W. Pang, Z. Tan, C. Dickinson and W.Z. Zhou, *Manuscript completed*.
- [19] S. Haul, *Z. Phys. Chem.*, 1939, **44**, 216
- [20] F. Ulrich and W. Zachariasen, *Z. Kristallogr. Kristallgeom. Kristallphys. Kristallchem.*, 1925, **62**, 620
- [21] A.W. Stevenson and Z. Barnea, *Acta Crystallogr. Sec. B*, 1984, **40**, 530

## *7. Conclusions and Future Work*

The main work presented in this thesis has been metal oxide PSCs. The main technique used for their investigation was the HRTEM, which was also used for other interesting nanomaterials. In this chapter, conclusions from the work are presented and the future work for the project is given.

### 7.1 Conclusions

Chromium oxide and cobalt oxide PSCs have successfully been synthesised in mesoporous templates SBA-15 and KIT-6. The PSCs were found to negatively replicate the templates mesoporous structure and the single crystallinity of the material was confirmed by using HRTEM and SAED. Both chromium and cobalt nitrates decomposed in mesopores forming the oxides at a lower temperature than bulk material and used a different intermediate route due to a confinement effect in the nanoscale channels. The chromium oxide templated by KIT-6 synthesised by the dual solvent method showed some relation between the orientation of the mesopore system and crystal orientation of the oxide. The isotherm for chromium oxide had two inflections at 4 and 9 nm, which were the same values obtained for the cobalt oxide in the same template. The specific surface area per volume for the cobalt oxide, templated by KIT-6, was over twice that of chromium oxide due to the cobalt oxide replicating the 2 sets of channels of the KIT-6 as opposed to one, which was the case for chromium oxide. A multicrystal growth mechanism was proposed and evidence of conjoined particles for cobalt oxide was presented. The magnetic behaviour of chromium oxide was compared with bulk material, revealing that the PSC behaved like 15 nm nanoparticles. The catalytic activity of chromium oxide PSC was also investigated and showed some interesting results. It is therefore very possible that this new type of materials can be developed into self-supported catalysts in the near future.

Cobalt oxide using SBA-16 and SBA-15 fibres resulted in mesoporous polycrystalline material and possible reasons why no PSC was formed were discussed. Iron oxide and silver were tried with FDU-12 and SBA-15 respectively; however no porous material was formed. HRTEM work on other nanomaterials was also presented.

## 7.2 Future Work

A recent project has started to carry on this work using different metal oxides, templates and methods. The reasons why some metal oxides form PSCs whilst others form polycrystalline or non porous material are being investigated in more depth. The chromium oxide PSC, templated by KIT-6, is currently undergoing electrochemical characterisation and neutron diffraction, which preliminary results look interesting. Additional catalytic experiments will also be tried out at Aberdeen University. Neutron diffraction has also been scheduled for the cobalt oxide PSC in November 2006.

The use of non siliceous templates for metal oxides that are dissolvable in both NaOH and HF is another avenue that this work can be taken. ZnO is dissolvable in both, so the mesoporous silica cannot be used as a template. In this case, using mesoporous carbon, synthesis of PSCs of ZnO is possible. Additionally, it would be an idea to try cobalt oxide and chromium oxide in carbon templates to see if they still form single crystals and they should be a replica of the mesoporous silica used for templating the carbon, as opposed to the negative replica if the silica is used as a template for porous carbon. Cobalt nanoparticles have already been prepared with carbon as a support, so the use of this material could result in using the existing particles as seed, however this could result in polycrystalline material.

Bimetallic porous material is another area of research that the material could be tried. Choosing two metal oxides or other compounds with similar crystal parameters, much like those

of CdSe and ZnS could integrate with each other. The easiest route would possibly be forming one of the metal compounds first, removing the template and then using the porous metal material to then template the other metal compound. This may cause the material to lose the porosity but could create a bimetallic crystal with uniform rods which has advantages in itself.

These ideas show that the creation of the chromium and cobalt oxide PSCs is only the start of research in this area. Not only will different metal oxide PSCs be formed, further increasing the exponential growth of new mesoporous material, but the tests in possible applications will also grow. The beauty of research is that every question answered leads to a hundred more questions.

## Publications

- \* 'HRTEM of negative replicas of mesoporous silica', W.Z. Zhou, K. K. Zhu, B. Yue, H.Y. He and C. Dickinson, *Stud. Surf. Sci. Catal.*, 2004, **154**, 924
- \* 'The oxidation of water by cerium (IV) catalysed by nanoparticulate RuO<sub>2</sub> on mesoporous silica', N.C. King, C. Dickinson, W.Z. Zhou and D.W. Bruce, *Dalton Trans.*, 2005, **6**, 1027
- \* 'Preparation and characterization of three-dimensional mesoporous crystals of tungsten oxide', B. Yue, H.L. Tang, Z.P. Kong, K.K. Zhu, C. Dickinson, W.Z. Zhou and H.Y. He, *Chem. Phys. Lett.*, 2005, **407**, 83
- \* 'Cell-targeting multifunctional nanospheres with both fluorescence and magnetism', H.Y. Xie, C. Zuo, Y. Liu, Z.L. Zhang, D.W. Pang, X.L. Li, J.P. Gong, C. Dickinson and W.Z. Zhou, *Small*, 2005, **1**, 506 (cover picture)
- \* 'Growth of porous single crystal Cr<sub>2</sub>O<sub>3</sub> in a 3D mesopore system', K. Jiao, B. Zhang, B. Yue, Y. Ren, S.X. Liu, S.R. Yan, C. Dickinson, W.Z. Zhou and H.Y. He, *Chem. Commun.*, 2005, 5618 (inside cover picture)
- \* 'Temperature-dependant Raman scattering of silicon nanowires', Z.X. Su, J. Sha, G.W. Pan, J.X. Liu, D.R. Tang, C. Dickinson and W.Z. Zhou, *J. Phys. Chem. B*, **110**, 1229
- \* 'Formation mechanism of porous single crystal Cr<sub>2</sub>O<sub>3</sub> and Co<sub>3</sub>O<sub>4</sub> templated by mesoporous silica', C. Dickinson, W.Z. Zhou, R.P. Hodgkins, Y.F. Shi, D.Y. Zhao and H.Y. He, *Chem. Mater.*, 2006, **18**, 3088
- \* 'A reinvestigation of sillen XI-type lead tellurium oxyhalides' D.O. Charkin, O.S. Morozov, E.A. Ulyanova, P.S. Berdonsov, V.A. Dolgikh, C. Dickinson, W.Z. Zhou and P. Lightfoot, *Solid State Sci.*, 2006, **8**, 1029
- \* 'Three-dimensional single crystals and their properties', C. Dickinson, A. Harrison, J.A. Anderson and W.Z. Zhou, *Stud. Surf. Sci. Catal.*, 2006, **In press**
- \* 'Wheat germ agglutinin-modified trifunctional nanospheres for carcinoma cell recognition' H.Y. Xie, M. Xie, Z.L. Zhang, Y.M. Long, X. Liu, M.L. Tang, D.W. Pang, Z. Tan, C. Dickinson and W.Z. Zhou, 2006, *Manuscript completed*